UNIVERSITY OF CALIFORNIA,
IRVINE

Ionic Current Manipulation in Solid-State Nanopores

DISSERTATION

submitted in partial satisfaction of the requirements
for the degree of

DOCTOR OF PHILOSOPHY

in Physics

by

Rachel Anne Lucas

Dissertation Committee:
Professor Zuzanna S. Siwy, Chair
Professor Kenneth J. Shea
Professor Javier D. Sanchez-Yamagishi

2021

DEDICATION

To

my mom, my family, and my friends

who have always supported me

TABLE OF CONTENTS

LIST OF FIGURES

LIST OF TABLES

ACKNOWLEDGEMENTS

I would like to express the deepest appreciation to my committee chair and research advisor, Professor Zuzanna Siwy, who's guidance, intelligence, and continual support has made my graduate research career possible.

I would like to thank my committee members, Professor Kenneth J. Shea and Professor Javier D. Sanchez-Yamagishi for serving on both my advancement and doctoral committees.

Additionally, I would like to thank my lab mates in the Siwy group who have provided much help, knowledge, and laughter along the way.

Finally, I would like to acknowledge NSF, Lawrence Livermore National Laboratory, and the U.S. Department of Energy for their support and funding.

CURRICULUM VITAE

Rachel Lucas

EDUCATION

University of California, Irvine — May 2021
Ph.D. in Physics
Ionic Current Manipulation in Solid-State Nanopores
Advisor: Professor Zuzanna Siwy

Purdue University — May 2016
B.S. in Aerospace Engineering
B.S. in Honors Applied Physics

EXPERIENCE

Graduate Student Researcher — March 2017 – May 2021
University of California, Irvine
Professor Zuzanna Siwy

Applied Innovation Research Translation Fellow — December 2019 – December 2020
University of California, Irvine

Teaching Assistant — September 2016- June 2017
University of California, Irvine

PUBLICATIONS

R. Lucas, Z. Siwy, "Tunable Nanopore Arrays as the Basis for Ionic Circuits," *Applied Materials & Interfaces*, 12 (50), 56622-56631 (Dec. 2020)

R. Lucas, C.Y. Lin, L. Baker, Z. Siwy, "Ionic Amplifying Circuits Inspired by Electronics and Biology," *Nature Communications*, 11, 1568 (Mar. 2020)

R. Lucas, C.Y. Lin, Z. Siwy, "Electrokinetic Phenomena in Organic Solvents," *Journal of Physical Chemistry B*, 123 (28), 6123-6131 (June 2019)

Y. Qiu, R. Lucas, Z. Siwy, "Viscosity and Conductivity Tunable Diode-like Behavior for Meso- and Micropores," *Journal of Physical Chemistry Letters*, 8 (16), 3846-3852 (Aug. 2017)

ABSTRACT OF THE DISSERTATION

Ionic Current Manipulation in Solid-State Nanopores

by

Rachel Lucas

Doctor of Philosophy in Physics

University of California, Irvine, 2021

Professor Zuzanna Siwy, Chair

Ionic current transport and nanopores go hand in hand. Ionic current has been used to investigate properties of nanopores and vice versa for many years. Nanopores are simply holes which contain dimensions on the nanoscale and ionic current is produced through them by placing the pores in a solvent containing an electrolyte. Ionic transport is investigated typically using current-voltage or current-time measurements. In this thesis ionic transport is studied and manipulated through three separate projects. We begin using cylindrical polymer pores ~700 nm in diameter and 11 μm in length to investigate the effect of organic solvents on ionic transport and thus electrochemical properties of polymer/liquid interfaces. Current-voltage measurements were taken in solutions with varying solvent type and varying concentration of $LiClO_4$. These measurements probed electroosmotic flow and allowed us to deduce surface charge properties of the pores. It was found that the carboxlyated surface of PET can flip charge polarity dependent on solvent type and concentration of $LiClO_4$. This work helped overall understanding of the origin of the effective

surface charge in organic solvents and its impact on ionic transport. Another method of ionic transport manipulation which was investigated utilized an ionic bipolar junction transistor. Nanopores in silicon nitride were sandwiched together with a thin film of Nafion which also contained a gate electrode. Current-voltage measurements were taken across the device while varying voltage at the gate. It was successfully demonstrated through this system that an ionic transistor with fully ionic inputs and outputs can easily be rearranged into amplifying units providing amplifications up to 300 times. Finally, this document goes on to investigate interpore effects by using arrays of nanopores with a gate electrode placed near one of the pores within the array. Ionic transport is investigated through modeling current-voltage characteristics both with and without application of voltage at the gate electrode. In this system complex interactions were revealed which allow for different pores to exhibit different ionic transport properties though subject to the same bulk solution concentration and voltage configuration. Findings from these projects could be useful in a variety of applications including preparation of artificial biocircuits or spatially controllable drug delivery devices.

INTRODUCTION

Ionic current plays a huge role in our day-to-day lives and can be utilized in a variety of different applications. Ion channels within our bodies form the basis for muscle movement, hearing, vision, and signal propagation in axons [1], [2]. These ion channels are also known as biological nanopores that exhibit a variety of exciting transport properties, including ion selectivity, and responsiveness to external stimuli such as voltage, binding of a molecule, mechanical stress, and light. Many of the properties have been emulated through the use of solid-state nanopores, where solid-state nanopores played the role of a template to which various functionalities were added. Nanopores in general are holes on the order of one billionth of a meter. Such pores separate two chambers of a conductivity cell and present the only conduit for ions and molecules to flow. Manipulation of ionic current through nanopores lends itself to many possible functions such as separations (e.g. desalination [3]), generation of spatial chemical gradients [4], drug delivery [5], [6], single molecule sensing [7], biomimetics [8], DNA sequencing [9] and creation of electronic circuit analogs [10]–[12].

Inspired by biological systems, control of ionic current in nanopores can be exerted through a diverse range of external stimuli. Voltage, pH, bulk solution concentration, chemical modifications, pore geometry, and pressure are all examples of stimuli/parameters which influence ion current [13]–[18]. In this work the dependence of ionic current on electrolyte concentrations, solvent type, voltage application, and interpore interactions are probed. Different stimuli are used to control current in different ways. For example, application of voltage can cause increase, decrease, or reversal of direction of current based on direction and magnitude of voltage applied [12] while interpore interactions can cause increase or decrease of current based on location with respect to other pores [4].

First, a detailed look at nanopore creation and characterization is presented. The fundamentals of nanopore physics and how modeling is performed are discussed next. After this solid background, three separate projects are addressed. Throughout these projects the details of several current control mechanisms will be explored. It is shown how each of the previously mentioned stimuli affect current and unique applications of each method are discussed. The first project explores the effects of solvent type on ionic current and focuses on organic solvents. Experimental evidence shows polymer carboxylated surfaces can switch charge polarity from negative in aqueous media to positive in propylene carbonate and acetone which contains $LiClO_4$. We developed a method that allows deduction of the effective charge polarity of the pore walls from the direction of electroosmotic flow. The next project goes on to explore ionic current under effects of voltage gating in ionic transistor devices. It is demonstrated that an ionic bipolar junction transistor with fully ionic inputs and outputs can be designed to detect small ionic input currents and amplify them up to 300 times. Finally, arrays of nanopores are explored as a method of ion current control. Here, pore placement within the array, application of gate voltage, and introduction of pores with surface charge patterning all contribute as potential mechanisms for control of ionic current magnitude and location within an array of pores. These projects contribute to our knowledge of the fundamentals of nanopore physics as well as potential applications such as biomimetics and ionic circuitry.

CHAPTER 1

Nanopore Creation and Characterization Methods

Single nanopore membranes used in this work were created in two types of materials, either polymer or silicon nitride films. The polymer membranes were made of polyethylene terephthalate (PET) and were prepared by the track-etching technique. Briefly, the technique entails irradiation with single heavy ions performed at the GSI Helmholtz Centre for Heavy Ion Research, followed by wet chemical etching at UC, Irvine. The silicon nitride chips were purchased from Norcada as thin, few tens of nm thick, films standing on 200 μm thick silicon supports. Individual silicon nitride nanopores were drilled using either focused ion beam (FIB) or electron beam in the transmission electron microscope (TEM). Within this chapter we will review the fundamentals of these techniques as well as pore size characterization methods.

1.1 Latent Tracks in Polymer Films

Single nanopores in 12 μm thick polymer films were created by the track-etch technique. This procedure combines latent damage tracks with wet chemical etching in order to create nanopores. Latent nuclear damage tracks are created when ions accelerated to high kinetic energies, ~GeV, pass through a dielectric film leaving a region of damage around it. Our group uses polyethylene terephthalate films that were irradiated at the UNILAC linear accelerator in Darmstadt, Germany. In our research we use films that were irradiated with single heavy ions, however irradiation densities up to 10^{10} per cm^2 can be achieved. Xenon ions or heavier are employed in the track-etching technique to prepare pores. A schematic of the GSI beam line and set-up for single ion irradiation is shown in Figure 1.1.

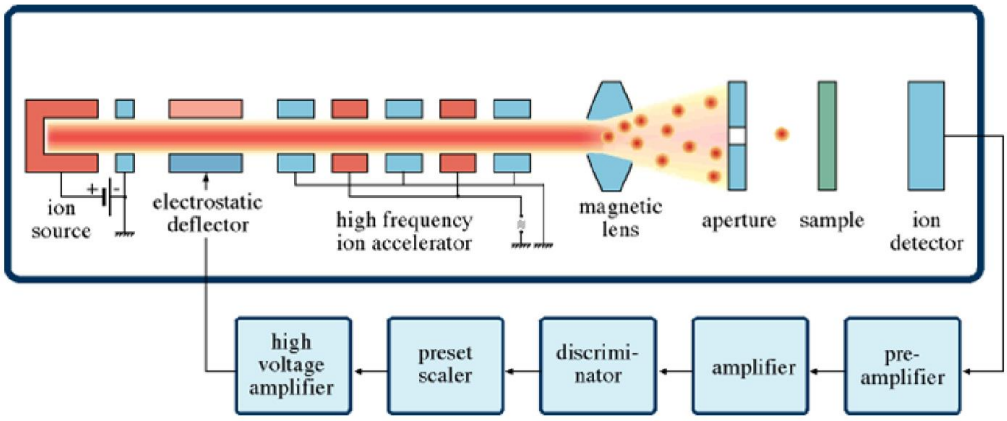

Figure 1.1: GSI beam line for single ion irradiation. The ion beam is accelerated up to the necessary energy and defocused; decreasing the rate of accelerated ions through the dielectric samples to approximately 1 ion/sec. Ion detection after the irradiated medium permits the beam to be deflected after the desired number of ions pass. Image from [19].

Single-ion irradiation is achieved through the use of a metal mask and beam defocusing. The polymer film samples are loaded into the sample holder, in front of which is a metal plate with an aperture of 100 μm which defines the area of the membranes that the ions may go through. There is a particle detector behind the sample holder which measures the number of ions that pass through the membranes. This detector is electronically connected to a system of two shutters in the beam path. First, there is a fast action shutter that closes within a few microseconds of detection of the desired number of ions. The second shutter is slower acting but is capable of withstanding the beam energy for longer periods of time. UNILAC uses heavy ions with energy of 11.4 MeV/nucleon that allows irradiating a 6-foil stack of 12 μm thick PET films. Once this process is complete the samples are removed and shipped to our lab.

1.2 Wet Chemical Etching of Polymer Nanopores

Latent damage tracks are necessary for the next step of polymer nanopore formation, chemical etching, to be performed successfully. The tracks provide a path for etching to occur

along and therefore the number of latent tracks defines the number of pores created. Before wet chemical etching begins, a step of exposure to UV radiation must be completed. This is done with a desk top UV lamp at a peak wavelength of 365 nm for 1 hour on each side of the membrane. This additional UV radiation was found to improve reproducibility of etching in some polymers [20], [21]. It is hypothesized that UV leads to further breakage of the polymer chains within the track, allowing increased reactivity during the chemical etching.

After UV irradiation, chemical etching is performed with the specific parameters of etching dependent on the pore size and geometry that we want to produce. In order to obtain cylindrical nanopores, an irradiated film is immersed in a bath of the required etchant so that the etching process occurs symmetrically (Figure 1.2). Cylindrical nanopores are obtained when the rate of etching along the track is significantly higher than the non-specific etching of the polymer material. In the case of PET these conditions are achieved in diluted solutions of sodium hydroxide (NaOH) at an elevated temperature. We used two types of conditions: 0.5 M NaOH at 70 °C, or 2 M NaOH at 50 °C. The diameter of the pore in this case is controlled by the amount of etching time.

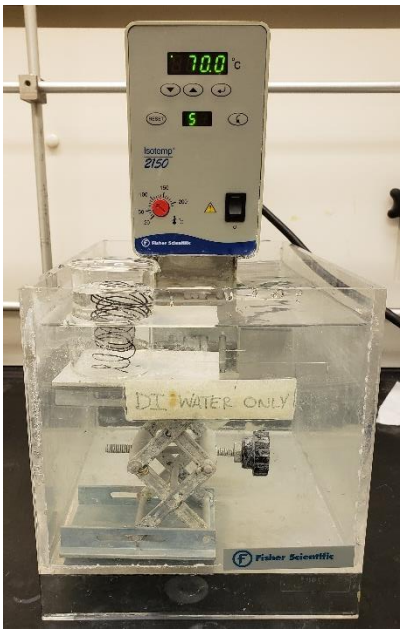

Figure 1.2: Hot water bath for etching cylindrical nanopores in polymer films. For PET, 0.5 M NaOH is placed in a beaker, as seen sitting in the bath, and heated to 70 °C. The membrane is placed into the beaker and held away from the beaker wall to ensure simultaneous etching from both sides.

Conical geometry of nanopores is achieved when the process of etching is performed asymmetrically, from one side only, and in conditions when the rate of etching along the track is only a few times higher than the non-specific etching of the material. Conical nanopores in PET are obtained by etching irradiated films at room temperature and with 9 M NaOH from one side. The other side of the film is in contact with acidic stopping medium composed of 1M HCOOH and 1M KCl. This asymmetric etching is performed in a conductivity cell where a film is placed between one chamber with NaOH and the other chamber containing the stopping solution. Once the pore is etched all the way through the stopping medium neutralizes the etchant and assures a slow increase of the nanopore opening diameter. The process of etching is monitored using platinum electrodes on either side of the membrane and measuring the resulting current with a Keithley 6487 picoammeter/voltage source (Figure 1.3).

Figure 1.3: Image of Keithley 6487 picoammeter/voltage source used in etching as well as electrochemical characterization experiments.

In the beginning of the etching process, we observe zero current. Once the etchant breaks through the whole thickness of the film a small amount of current is seen followed by a spike of current (Figure 1.4). At this point the NaOH can be removed and replaced with stopping solution in order to neutralize the reaction. This protocol will create the smallest possible nanopore diameter, down to few nanometers. If a larger diameter is desired the NaOH is left in to continue etching for the desired amount of time.

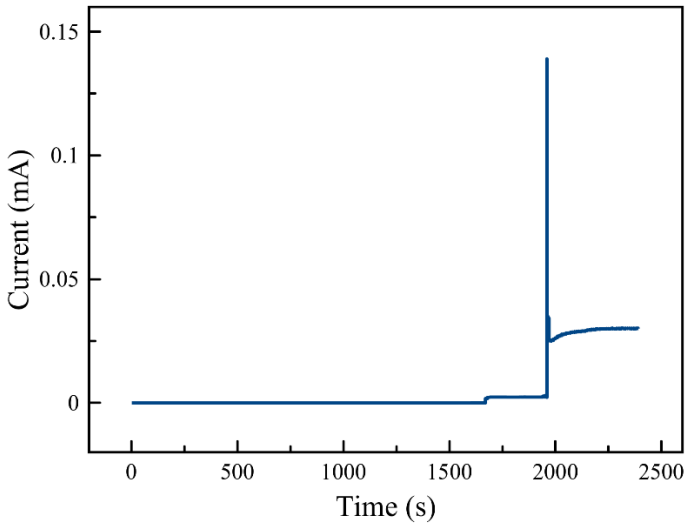

Figure 1.4: Example of an etching curve for a PET film. Current is monitored over time to view pore breakthrough, visible as a spike in current, and enlargement, which occurs after breakthrough.

The conductivity cell mentioned above is used for both etching and electrochemical characterization of the pores. The cell utilizes a metal chassis made of stainless steel,

aluminum, or brass. A large thumbscrew through one end of the chassis allows force to be applied in order to hold the conductivity cell blocks together and create a pressure seal with the membrane placed between them. The cell blocks are machined out of polychlorotrifluoroethelyne (Kel-F), whose chemical resistance allows it to be used in the extreme etching conditions required for chemical etching. Parafilm-M laboratory film is placed on either cell block between the Kel-F and the membrane in order to produce a satisfactory seal. A schematic of the conductivity cell is shown in Figure 1.5.

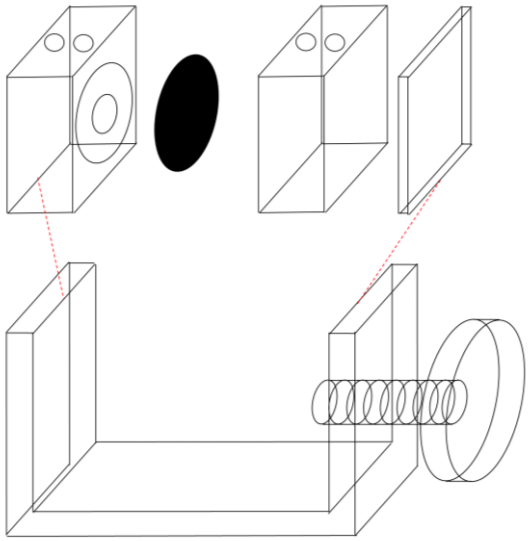

Figure 1.5: Schematic of conductivity cell setup for polymer films. Top level shows two Kel-F cell blocks with a polymer film (shown in black) placed between then. The right plate is a metal plate placed between the cell block and the screw in order to distribute pressure through the system more evenly. The top row is placed, in the order shown, into the chassis shown on the bottom row which then screws in to hold everything together.

1.3 Focused Ion Beam Drilling of Silicon Nitride Nanopores

The track-etching technique allows for a reproducible preparation of polymer nanopores with an opening diameter as small as a few nm. These pores however still have a micron scale thickness and thus some fundamental nanoscale effects are not visible with these large

aspect ratio pores. It would also be of interest to prepare pores whose length is comparable to the length of biological channels. As first shown by Li et al. [22], focused ion beam (FIB) drilling through silicon nitride or silica films provides a facile way to make nanopores through thinner films from 10 nm up to a few microns thick. Using this method, it is also possible to image the pores in order to get more exact pore sizes and even pore geometries. FIB uses a high beam intensity (10^7 A/m^2 or greater) along with a spot size, in our case, of tens of nanometers to drill a nanopore through silicon nitride or silicon dioxide membranes that are commercially available (Norcada). These pores generally have an hourglass shape with a half-opening angle of 5° [23] and can have diameters ranging from ~80 nm to many microns using the setup shown below (GAIA3, Tescan, Figure 1.6).

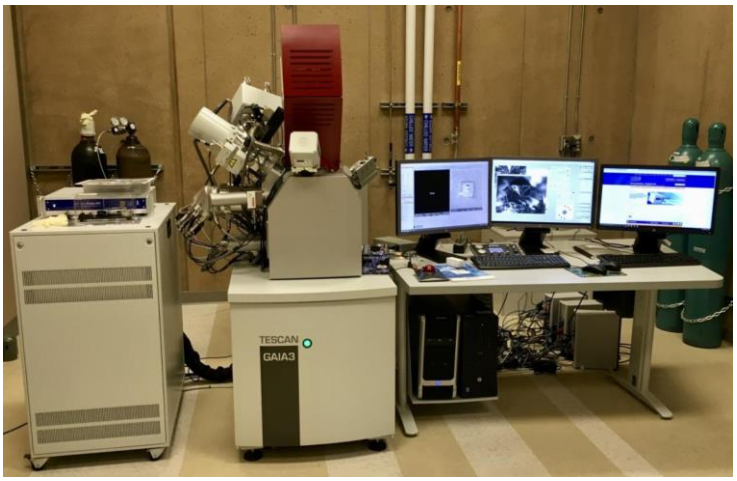

Figure 1.6: Image of the Tescan GAIA3 SEM-FIB at the University of California, Irvine's Materials Research Institute (IMRI).

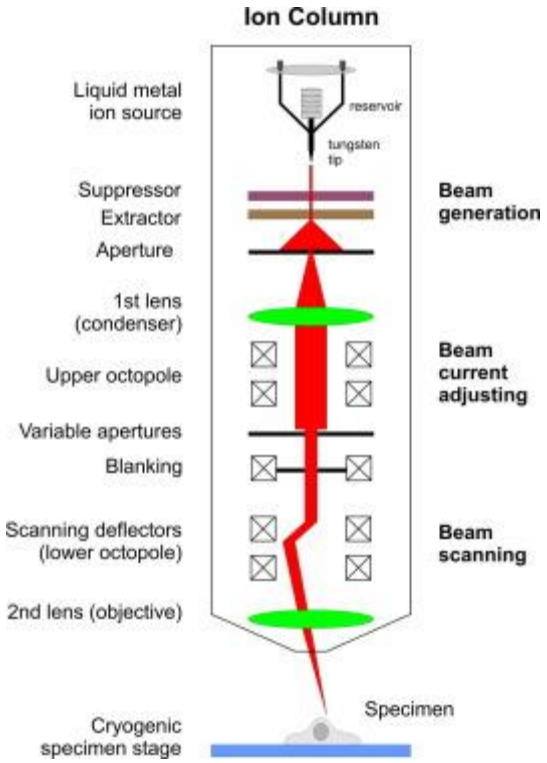

Figure 1.7: Beam generation in the ion beam column. The high-energy ion particle beam is produced from a liquid metal ion source at the top of the FIB column. It is condensed and focused onto the specimen by a set of electrostatic lenses and deflection coils [24]. Reprinted from Archives of Biochemistry and Biophysics, vol. 581, A. Rigort and J. M. Plitzko, Cryo-focused-ion-beam applications in structural biology, pp. 122-130, Copyright 2015, with permission from Elsevier.

A generic schematic of the setup of a FIB is shown above (Figure 1.7). The ion beam itself is generated by a liquid metal ion source (LMIS) which is shown at the top of the beam line. Usually gallium ions, Ga^+, are used due to low melting point and vapor pressure. Ions are extracted from the source via field evaporation and are then focused into a beam using electrostatic lenses. Typically, a LMIS contains a capillary tube with the reservoir of gallium and a tungsten needle with a very sharp tip running through it [24]. The reservoir is heated close to the temperature of evaporation which causes the liquid gallium to flow along the needle to the tip. Then the extractor, an extraction electrode, is used to force the liquid metal meniscus to form a sharp cone by using a strong electrostatic force. The high electric field (~6-9kV) extracts ions which are then accelerated towards the extractor. A series of lenses

and apertures are then used to focus the ion beam to a desired spot size (Figure 1.7). A spray aperture blocks the majority of ions that are not going in the direction of the desired beam. This beam is then focused and collimated by the set of upper condenser lenses. Astigmatism of the beam can be adjusted using the upper octupole lens. Beam current is controlled by adjustable size apertures in a range from 1 pA to 10 nA. A blanking deflector and aperture are used to keep the beam from reaching the sample when desired. The lower set of octupole lenses allows for the beam to be scanned over the sample as the user defines. Lastly, the lower objective lens is utilized for focusing and reducing the spot size of the beam. The impact of the beam on the sample surface leads to material removal by a sputtering process and thus allows patterns, such as nanopores, to be cut out of the material. This process can also cause damaging effects to the sample such as superficial gallium implantation. This effect depends on various properties of the FIB and specimen and as such, these properties must be controlled in order to minimize damages. An example of a pore fabricated using FIB is shown in Figure 1.8 below.

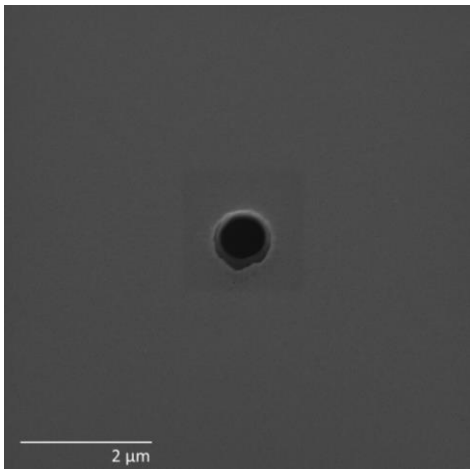

Figure 1.8: An example of an ~650 nm in diameter pore fabricated using FIB. Image taken using scanning electron microscope (SEM) with high voltage 10 kV. The pore was drilled in a 30 nm thick silicon nitride chip.

1.4 Transmission Electron Microscope Drilling of Silicon Nitride Nanopores

Focused ion beam can drill pores within fractions of a second, and in relatively thick substrates, but the diameter of the pores created, in our case, is limited to ~80 nm or larger. In order to produce smaller pores a different technology is required, e.g. transmission electron microscopy (TEM). Some of the first pores created using this technique are shown in Storm et al. [25]. The silicon nitride films used for preparation of nanopores by TEM must be very thin, less than 50 nm in thickness. In such thin films, nanopores with diameters of 4-5 nm can be drilled directly; a subsequent shrinking approach leads to further diminishing of the pore diameter to ~ 1 nm [25]. TEM drilled nanopores can also be examined for their opening diameter and even 3D geometry. In our work, we used a Joel JEM-2100F TEM, an image of which is shown in Figure 1.9.

Figure 1.9: Image of the Joel JEM-2100F TEM taken at the IMRI facilities at the University of California, Irvine.

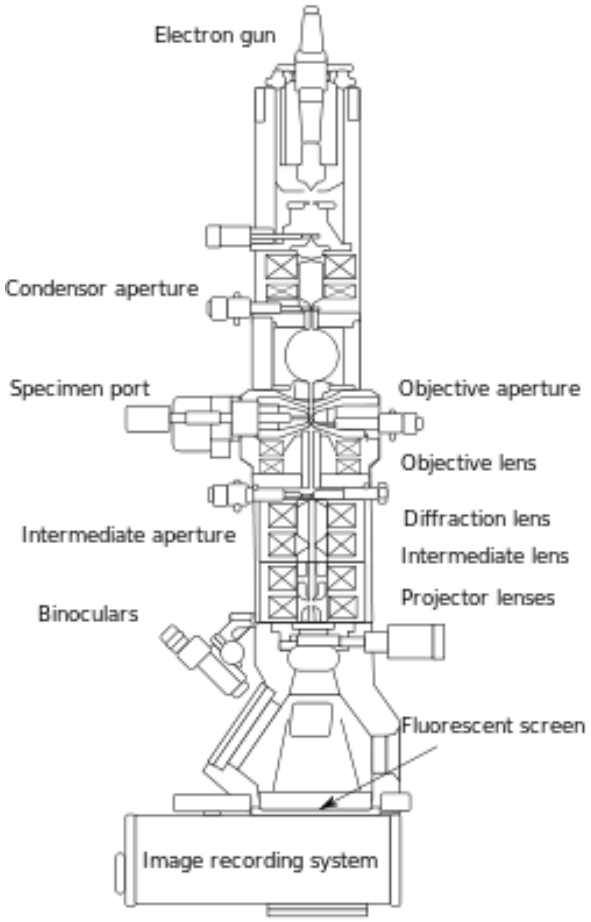

Figure 1.10: Diagram outlining the internal components of a basic TEM system. The high-energy electron beam is produced from a tungsten filament cathode, the electron gun, at the top of the TEM column. It is condensed and focused onto the specimen by a set of electrostatic lenses [26].

A schematic of a general TEM setup is shown in Figure 1.10. In TEM a beam of electrons is used as a nanofabrication and imaging tool, rather than ions, allowing for the ability to create smaller pore sizes and see smaller features. The beam is produced using a cathode with a high-voltage electricity power supply. The cathode, which in our case is a tungsten filament or needle, is given enough current to begin to emit electrons either by thermionic or field electron emission into the vacuum. Once the beam is created an electromagnetic coil acts as the first lens, concentrating the electrons into a denser beam. A second electromagnetic coil, acting as the second lens, focuses the beam onto a specific part of the sample – changing the

beam from wider to narrower. The beam is then restricted by the condenser aperture. The sample itself sits in the middle of the main microscope tube and the beam passes through it to gather an image which is then focused by the objective lens. Optional objective and intermediate apertures can be used to further restrict the beam. The image is passed through the projector and intermediate lenses, magnifying the image. Finally, the image becomes visible when the electron beam hits a fluorescent pad at the bottom of the machine. The image can be viewed directly or on a computer monitor [27].

In order to fabricate a nanopore the beam brightness must be focused and tuned finely into the smallest possible point. Once focused, the beam remains on the sample surface, and removes material, for a specified amount of time to create the desired pore size. Once finished the beam brightness is unfocused to keep from enlarging the pore further. In our case, a pore ~5 nm in diameter can be created within 3 minutes with an accelerating voltage of 300 kV at 250 kx magnification. An example of a nanopore fabricated using TEM is shown in Figure 1.11 below.

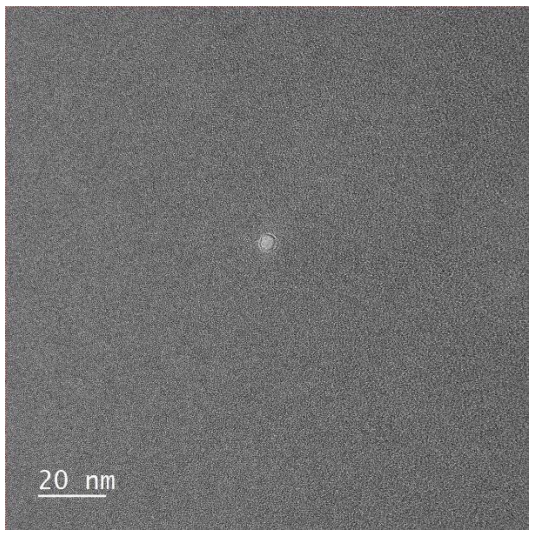

Figure 1.11: An example of an ~5 nm in diameter pore fabricated using TEM.

1.5 Sizing and Characterization of Nanopores

Different sizing characterization methods are necessary for different types of nanopores. For the polymer pores, electron imaging can be difficult for several reasons. For a single pore the area necessary to scan in order to find the pore is out of the range of scanning electron microscopy (SEM) and TEM requires much thinner samples to operate. Even when using multipore membranes, the smallest diameter of pores is below the resolution limit of SEM. It is also possible that imaging could damage the membrane surface and change the dimensions of the pores. Therefore, gold is usually used as a protective layer and to keep the dielectric surface from charging. However, this again changes the diameter of the pores, especially in smaller size ranges.

Thus, for single polymer nanopores, our lab uses measurement of ionic current as the simplest, non-destructive, and most accurate determination of pore diameter. If we treat the nanopore as a cylindrical resistor, we can solve for the pores resistance from first principles and use this to find the pore diameter. In order to decrease the influence of the electrical double layer on the pore sizing, high ionic strength solutions are used. Therefore, for our measurements we use 1 M KCl at pH 8. In 1M KCl the double layer length is ~ 0.3 nm [28] so that the linear dielectric approximation for our cylindrical resistor is valid for small voltages. The equation for resistance of a cylindrical resistor is given as:

$$R = \rho \frac{L}{A}$$

where ρ is material resistivity, L is cylinder length, and A is cross-sectional area. In our case of a pore filled with a solution, we use solution conductivity as $\sigma = \frac{1}{\rho}$ and area $A = \frac{\pi}{4}d^2$. Then we can solve for pore diameter, d, as:

$$d = \sqrt{\frac{4L}{\sigma \pi R}}$$

Conductivity for our solution of 1 M KCl is known to be ~11 S/m. Length, L, of the system is also known or can be estimated using bulk etching rate. Resistance of the cylinder is found from the slope of current-voltage, or IV, measurements of the pore, examples of which can be seen in Figure 1.12.

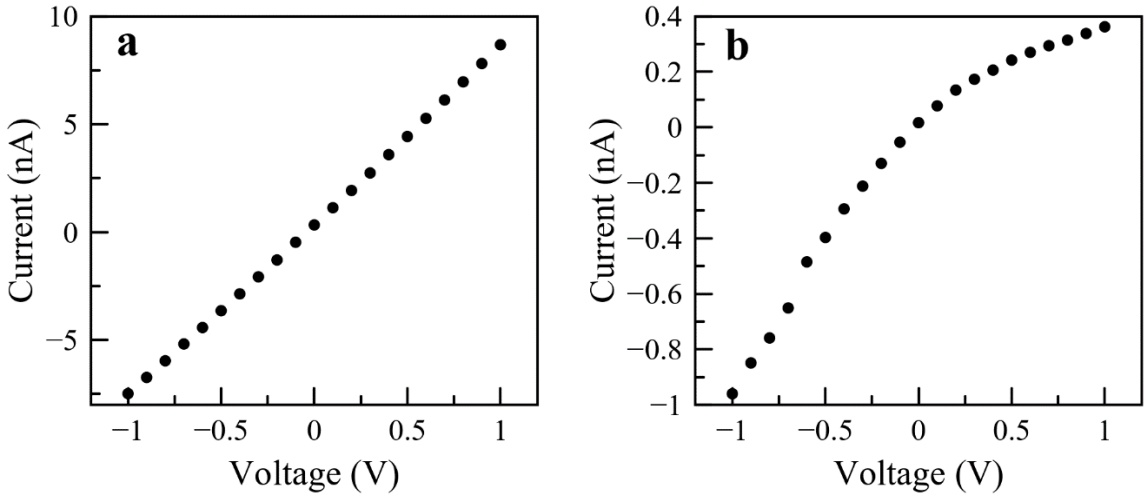

Figure 1.12: Example of current-voltage curves for a (a) cylindrical and (b) conical pore in PET in 1 M KCl. Pore sizes are 100 nm in diameter for (a) and tip diameter 2 nm, base diameter 510 nm for (b).

The IV curves are recorded by applying a scan of voltage across the pore using a pair of silver/silver chloride electrodes driven by a Keithley 6487 picoammeter/voltage source which simultaneously measures the ion current. The process is automated by computer via

a LabView program. The IV curve slope is only sampled at smaller voltages where linear behavior is displayed in order to keep the equation results as accurate as possible.

For conical nanopores the equation for resistance has to be adjusted to include the varying diameter along the pore axis. The resistance of a conical resistor is given as:

$$R = \rho \frac{4L}{\pi d D}$$

where d is the tip diameter and D is the base diameter. This can be solved similarly to get a tip diameter of:

$$d = \frac{4L}{\sigma \pi D R}$$

Here base diameter, D, is estimated using the bulk etchant rate of 2.13 nm/min for 9M NaOH at room temperature for PET [29].

It is important to realize that our current-voltage measurement is actually probing the total resistance of the system and not only the resistance of the pore itself. However, in the case of our polymer pores the resistance of the pore dominates the system with GΩ or MΩ resistances, allowing other resistances to be neglected.

For other systems, such as our thin silicon nitride membranes, other resistances must be taken into account in order to calculate pore diameter from IV measurements. In this case, because the aspect ratio is much lower compared to polymer pores (often less than 1), access resistance plays a significant role in the system and must be taken account. Introducing access resistance into the equation of the system resistance gives us:

$$G = \sigma\left(\frac{4L}{\pi d^2} + \frac{1}{d}\right)^{-1}$$

where G is the ionic conductance of the pore and $G = \frac{1}{R}$ [30]. Solving for d gives us the diameter of our pores in silicon nitride. Conductance is found similarly using the slope of current-voltage measurements. However, a different experimental setup is necessary for these measurements due to the small size and fragile nature of the silicon nitride chips. Instead of the Kel-F conductivity cell used for the polymer films a smaller cell block structure is utilized. These cells are made from polydimethylsiloxane (PDMS) using a plastic molding structure. The PDMS base polymer and hardening agent are mixed together at a 10-to-1 mass ratio and poured into the mold. These are cured at room temperature for 3 days to solidify the PDMS. Oxygen plasma is used to bind necessary pieces of the cells together in order to complete the structure. These cells do not require the use of parafilm to create a satisfactory seal with the membrane. The conductivity cell scheme is shown in Figure 1.13. The rest of the measurement setup remains similar to the polymer films, using silver/silver chloride pellet electrodes along with the Keithley 6487.

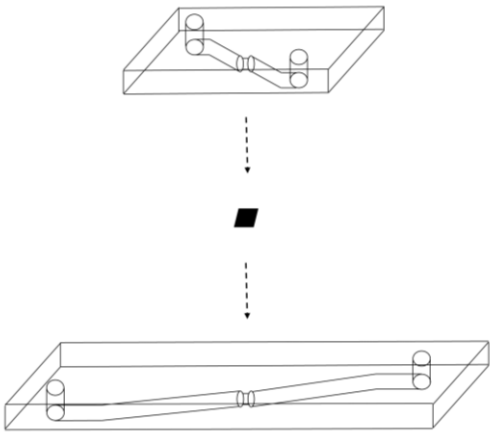

Figure 1.13: Schematic of conductivity cell setup for silicon nitride films. On the top and bottom are PDMS cell blocks with the silicon nitride chip (shown in black) placed between them. A hand clamp is used to hold the structure together.

For silicon nitride samples the determination of pore size through IV measurements is usually used as a verification method due to the fact that pore size can easily be measured through imaging right after the pore is created.

CHAPTER 2

The Theory and Modeling of Nanopore Transport

Transport of ions, molecules, and water through nanoscale channels is important in biology where protein channels through cellular membranes are responsible for heart-beat regulation, signal transduction, and maintaining salt and mineral concentrations necessary for life. The study of transport in synthetic nanopores may provide insight into biological processes due to the fact that both must obey the same laws of physics. Transport through nanopores in general is the combination of many processes, such as diffusion, migration, and convection; these processes are coupled to other nanoscale effects including the formation of an electrical double layer if the transport species and/or the pores carry surface charge. In order to understand transport mechanisms, basic fluid transport behaviors are reviewed in this chapter.

2.1 Ion Transport Theory

Throughout this work measurements of ion current through nanochannels are shown. These current readings are recorded due to application of an electrochemical potential difference. It is thus fundamentally important to understand the forces responsible for this ionic motion. A potential difference can be produced through various methods such as a gradient in the electric potential, pressure, concentration, or temperature. The research in this thesis uses only electric potential and conductivity gradients so we will focus on these.

The most basic type of motion undergone by ions is diffusion, which is transport due to a concentration gradient. Conceptually this is thought of as ions flowing from areas of high

concentration to areas of low concentration. The molecular basis for diffusion is Brownian motion, or random thermal motion of all species in solution. When a finite ionic concentration gradient is established, a measurable ionic current can be recorded, and predicted through so-called Fick's law [31]:

$$\vec{j}_i^{diffusion} = -D_i \nabla C_i. \tag{2.1}$$

This equation shows the flux, $\vec{j}_i$, of species i depends on both concentration gradient, ∇C_i, and on how quickly the charges can move, or the diffusion coefficient, D_i, of each particle. In more technical terms the diffusion coefficient is a measure of how far a solute particle will move in a solution of some viscosity, η, at a given temperature, T, for some set period of time. A quick derivation of the value for diffusion coefficient begins with equating Fick's law with the traditional equation for flux $\vec{j}_i = C_i v$ where v is velocity. Assuming we have particles suspended in a liquid subject to gravity, the concentration will behave according to the barometric distribution: $C_i = C_0 e^{-\frac{mgh}{k_B T}}$ where m is mass, g is the gravitational constant, h is height of the particle, and k_B is the Boltzmann constant. Substituting this into our equality and solving we find:

$$v = \frac{D_i m g}{k_B T} \tag{2.2}$$

Knowing also that under the action of gravity a particle acquires a speed $v = \mu m g$, where μ is the mobility of the specific particle or ion, we can equate these two velocity expressions and finally arrive at the Stokes-Einstein equation for diffusion coefficient:

$$D_i = \mu k_B T. \tag{2.3}$$

For charged particles in the presence of an electric potential gradient a force in addition to diffusion is seen. This force is called the electrophoretic force and is essentially electrical migration. Any charged particle within a potential gradient feels a force $q_i E$ due to the electric field. Since in solution the transport is considered over-damped, this force is balanced by friction, and a particle reaches so-called drift velocity:

$$q_i E = \gamma \, v_{drift} \tag{2.4}$$

where γ is a drag coefficient that for spherical particles can be found from the Stokes formula, so that:

$$v_{drift} = \frac{q_i E}{6\pi\eta r_i}, \tag{2.5}$$

where q_i is the ion charge ($q_i = z_i e$ where z_i is valency and e is charge of an electron), r_i is particle radius, and E is the electric field. The flux is then:

$$\vec{J} = v_{drift} c_i. \tag{2.6}$$

Using Einstein's relation we can then obtain the expression for electrophoretic flux as:

$$\vec{J_i}^{electrophoresis} = D_i \frac{qEc_i}{k_B T}. \tag{2.7}$$

The final type of transport that is important in our system is convection, thus when the solution is moving and carrying the ions along with it. Convective flux is given by the simple equation:

$$\vec{J_i}^{convection} = \vec{u} c_i. \tag{2.8}$$

In this equation $\vec{u}$ is the velocity of the fluid. The motion of the fluid in the system can be due to a number of different forces in the system, an example of which is pressure.

Now that we have equations for the three most important forces relating to ion motion, diffusion, electrophoresis, and convection, we can combine them into one equation describing the transport of charged particles through a nanopore system. This equation is called the Nernst-Planck equation:

$$\vec{J}_i = \vec{J}_i^{diffusion} + \vec{J}_i^{convection} + \vec{J}_i^{electrophoresis} \tag{2.9}$$

$$\vec{J}_i = -D_i \nabla c_i + \vec{u} c_i + c_i \mu_i^{ep} \vec{E}. \tag{2.10}$$

Here the electrophoretic mobility, μ_i^{ep}, has been defined as $\mu_i^{ep} = \frac{D_i q_i}{k_B T}$ from the Einstein-Smoluchowski relationship.

In order to directly compare the predicted flux with experimental observables, we are interested in finding an expression for ion current. To do this we multiply flux by the charge of the ionic species $q_i = z_i e$. To get the total current density we have to sum across all ionic species:

$$\vec{J} = \sum_i^{species} \vec{J}_i = \sum_i^{species} \vec{J}_i^{diffusion} + \vec{J}_i^{convection} + \vec{J}_i^{electrophoresis} \tag{2.11}$$

$$= \sum_i^{species} -z_i e D_i \nabla c_i + z_i e \vec{u} c_i + z_i e c_i \mu_i^{ep} \vec{E}. \tag{2.12}$$

In our experiments with nanopores, electrophoresis is usually the largest contributor to the experimentally observed ion current. Diffusion generally only plays a greater role in the system when there is a large conductivity gradient at play.

2.2 The Electrical Double Layer

Nanopores have high surface-to-volume ratios which make their transport properties unique and fundamentally interesting when compared to macroscale pores and channels. If

the walls are charged, ionic concentrations in the channel can be different than ionic concentrations in the bulk electrolyte in contact with the nanopore. Electrostatic interactions with the pore walls are one of the most studied effects in nanochannel systems and lead to interesting behaviors such as the formation of the electrical double layer. A representation of what the electrical double layer looks like is given in Figure 2.1.

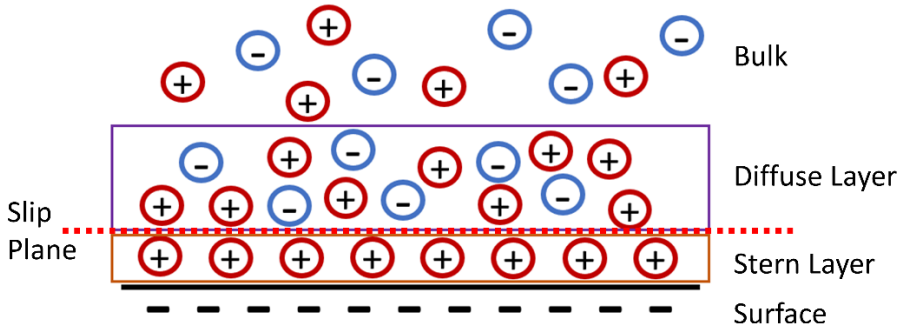

Figure 2.1: Scheme of the electrical double layer under the Gouy-Chapman and Stern model. Counterions, or ions with charge species opposite to that of the surface charge, adsorb near the pore surface with a reduced number of coions, or ions of the same charge species as the surface charge, just outside the Stern layer. Both species' concentrations are equal in the bulk.

As its name suggests, the electrical double layer is made up of two layers: the Stern layer and the diffuse layer composed of counterions to the charges on the pore walls. The Stern layer consists of ions that are the closest to the surface and are believed to be immobile relative to the surface. The diffuse layer is made of ions that are free to move in solution and is composed of ions that electrically screen the first layer. The diffuse layer contains both counterions and co-ions. At a distance when surface charges are screened, the concentrations of both ions reach the bulk values.

The diffuse layer can be mathematically described by what is known as the Poisson-Boltzmann distribution. This is derived using concepts from the Poisson equation and the

Boltzmann distribution. The Poisson equation is used to solve for complex potentials as a function of charge density in the system and it is given to be:

$$\nabla^2\varphi = \frac{-\rho_{charge}}{\varepsilon_r\varepsilon_0}. \tag{2.13}$$

Here ρ_{charge} is the charge density, ε_r is the dielectric constant of the fluid, ε_0 is the vacuum permittivity of free space, and φ is the electric potential. Typically, if we thought of a point charge near an infinite surface characterized with a finite charge density, we would just apply the Poisson equation to get our potential solution. In the case of electrolyte solution however, in the presence of the electrical double-layer, a test charge would feel not only the presence of the surface but also all the other charged particles (ions) around it. In order to account for this effect, the Boltzmann distribution is typically used as it describes the distribution of free charges in solution. It is given, for the case of concentration, to be:

$$c_i = c_{0,i}\mathrm{e}^{-\frac{z_i e\varphi}{k_B T}}. \tag{2.14}$$

Here $c_{0,i}$ is the bulk concentration and z_i is the valency of the charge species.

Now we can rewrite the charge density of the Poisson equation in order to get the Poisson-Boltzmann equation:

$$\nabla^2\varphi = -\frac{1}{\varepsilon}\sum_i z_i e c_{0,i}\mathrm{e}^{-\frac{z_i e\varphi}{k_B T}}. \tag{2.15}$$

This equation is used to solve for φ which can then be plugged back into the Poisson equation in order to obtain the ion concentrations, c_i. This process is generally solved numerically but analytical solutions exist for simple geometries with small electrostatic potentials within the solution.

We will now derive an equation that is often applied to estimate the thickness of the electrical double-layer and a range of electrostatic interactions. Here the unit normal is in the y-direction and the surface is characterized with homogeneous surface charge density, σ. The solution in contact with the surface contains an electrolyte at a concentration c, that for simplicity is dissociated into ions with equal valency z and identical diffusion coefficients, D_i. This case describes solutions of potassium chloride, used very commonly in our lab. The electrostatic potential energy of the ions is given by $U_i = z_i e\varphi(y)$ where φ is a function of y only due to the symmetry of the system. In this system the Poisson-Boltzmann equation becomes:

$$\frac{d^2\varphi}{dy^2} = \frac{zec_0}{\varepsilon}\left[\mathrm{e}^{\frac{ze\varphi}{k_BT}} - \mathrm{e}^{-\frac{ze\varphi}{k_BT}}\right]. \tag{2.16}$$

A simple solution can be obtained by linearizing the right-hand side of the equation with the assumption, $ze\varphi \ll k_BT$. Applying the correct boundary conditions gives us the Debye-Huckel approximation:

$$\varphi = \varphi_0 \mathrm{e}^{-\frac{y}{\lambda_D}} \tag{2.17}$$

$$c_i = c_{i,0} e^{-\frac{ze\varphi}{k_BT}} \tag{2.18}$$

$$\lambda_D = \sqrt{\frac{\varepsilon_r \varepsilon_0 k_B T}{2c_0 N_A e^2 z^2}} \tag{2.19}$$

where N_A is Avogadro's number. Here a new parameter is introduced, the Debye length, λ_D, which is a measure of the charge carrier's net electrostatic effect in a solution and how far that effect persists. Every Debye length, λ_D, the electric potential decreases in magnitude by $\frac{1}{e}$. The above solution reveals to us not only that the potential decays exponentially away

from the wall but also that the counterion species are enriched at the surface, the coions diminished, but recovering their concentration towards the bulk as we saw in the initial electric double layer scheme, Figure 2.1. The Debye length is one of the most useful parameters for nanopore systems as it gives a characteristic length for the region within the pore that departs from bulk behavior. As seen in its equation, the Debye length increases with decreasing ion concentrations. A table with some typical values for KCl solution is shown below (Table 2.1).

Concentration [M]	**Debye Length [nm]**
1	0.3
0.1	1
0.01	3
0.001	10

Table 2.1: Some examples of calculated values for Debye length in KCl at various concentrations at room temperature.

The values shown in Table 2.1 give good initial guidance for electrostatic interaction length scales. However, the Debye length equation was derived using very specific conditions for low surface potentials. Therefore, in reality the range of electrostatic interactions can be much higher than what is seen in Table 2.1.

Though we discussed here the electrical double layer in the context of a planar surface, most bodies immersed in solution will have some surface charge and therefore their own electrical double layer. The importance of the double layer in novel conductance properties of nanopores cannot be overstated and accordingly there are many phenomenon that arise as a direct consequence of the formation of the double layer.

2.3 Electroosmosis

One phenomenon that occurs due to the formation of the electrical double-layer (EDL) is electroosmosis. We know that ions migrate when exposed to an electric field and that when they move, they tend to drag fluid along with them due to viscous forces. Within a nanopore with some surface charge, counterions accumulate along the surface, as we have seen within the EDL. When an electric field is applied, force is acting on the region with net charge; consequently, this tube of ions moves dragging the solution in the interior of the pore along with it (Figure 2.2). This is called electroosmosis (EOF).

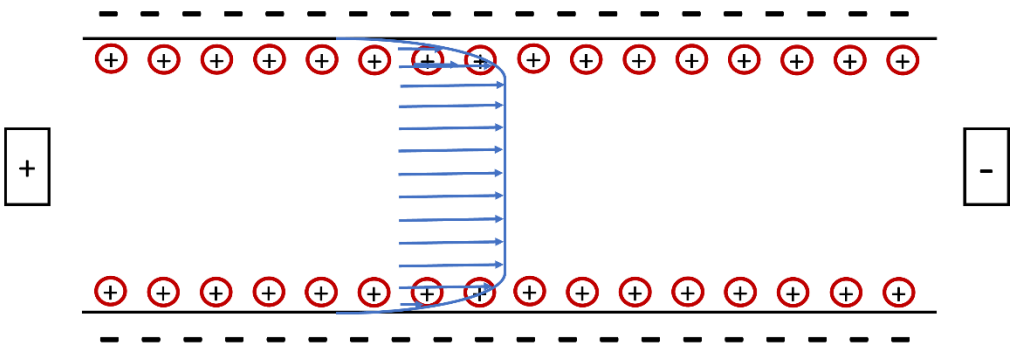

Figure 2.2: Scheme showing electroosmosis within a nanochannel. Plug flow is shown, keeping a constant fluid velocity outside of the double layer.

Though the effect originates due to only a ~1nm thick EDL, electroosmosis is observable in micro- and even milli-sized systems. This is due to the viscous coupling of the fluid at the surface to the rest of the nanopore interior. In the bulk solution EOF does not produce current due to net charge neutrality, however in the EDL EOF does contribute to measured ionic current. In larger systems this effect is usually negligible, but it can become important as the size of the system decreases.

The Poisson-Boltzmann and Navier-Stokes equations, discussed later, can be solved in order to get the electroosmotic velocity next to a charged plane:

$$u = -\frac{\varepsilon_r \zeta}{\eta} E_{ext} \tag{2.20}$$

where E_{ext} is the external electric field and ζ is the zeta potential, or the local electric potential in the screening layer. More technically, the zeta potential is within the double layer at the location of the slip plane, where mobile fluid is separated from fluid that remains attached to the surface, relative to a point in the bulk fluid away from the interface (Figure 2.1). By using equation 2.20 it is possible to measure the pore's zeta potential by experimentally observing the fluid flow velocity, for example by tracking the motion of small particles moving in the fluid flow.

2.4 Ion Current Rectification

An ion channel or a nanopore rectifies when its conductance for one voltage polarity is different than the conductance for the opposite voltage polarity. The presence of the electrical double layer by itself cannot induce ion current rectification since the system is symmetric with respect to switching the electrodes, and the direction of electric field. However, rectification can occur by introducing asymmetry into the system, along with ion selectivity. There are many ways to introduce asymmetry into the system such as varying pore geometry and surface charge pattern. Another example considered in more detail in a future chapter introduces asymmetric electrolyte conditions such as varying concentrations or viscosities.

Looking more into the case of varying pore geometries, consider a conical nanopore with a negative surface charge. This system will present rectification due to the unequal pore openings at the membrane sides. At the tip-side of the pore there will be an excess of counterions due to the presence of the electrical double layer, and the comparable size of the electrical double layer and the pore radius; the base-side of the pore will more closely resemble the bulk (Fig. 2.3). Ion current rectification occurs in this system due to the fact that the number of ions in the pore is voltage dependent. For one voltage polarity there is an enhancement of ionic concentrations compared to the bulk and for the opposite polarity a depletion zone is created, as can be seen in Figure 2.3. This means that the ionic current is greater for one voltage polarity than at the opposite polarity, or there is ion current rectification (Figure 2.4).

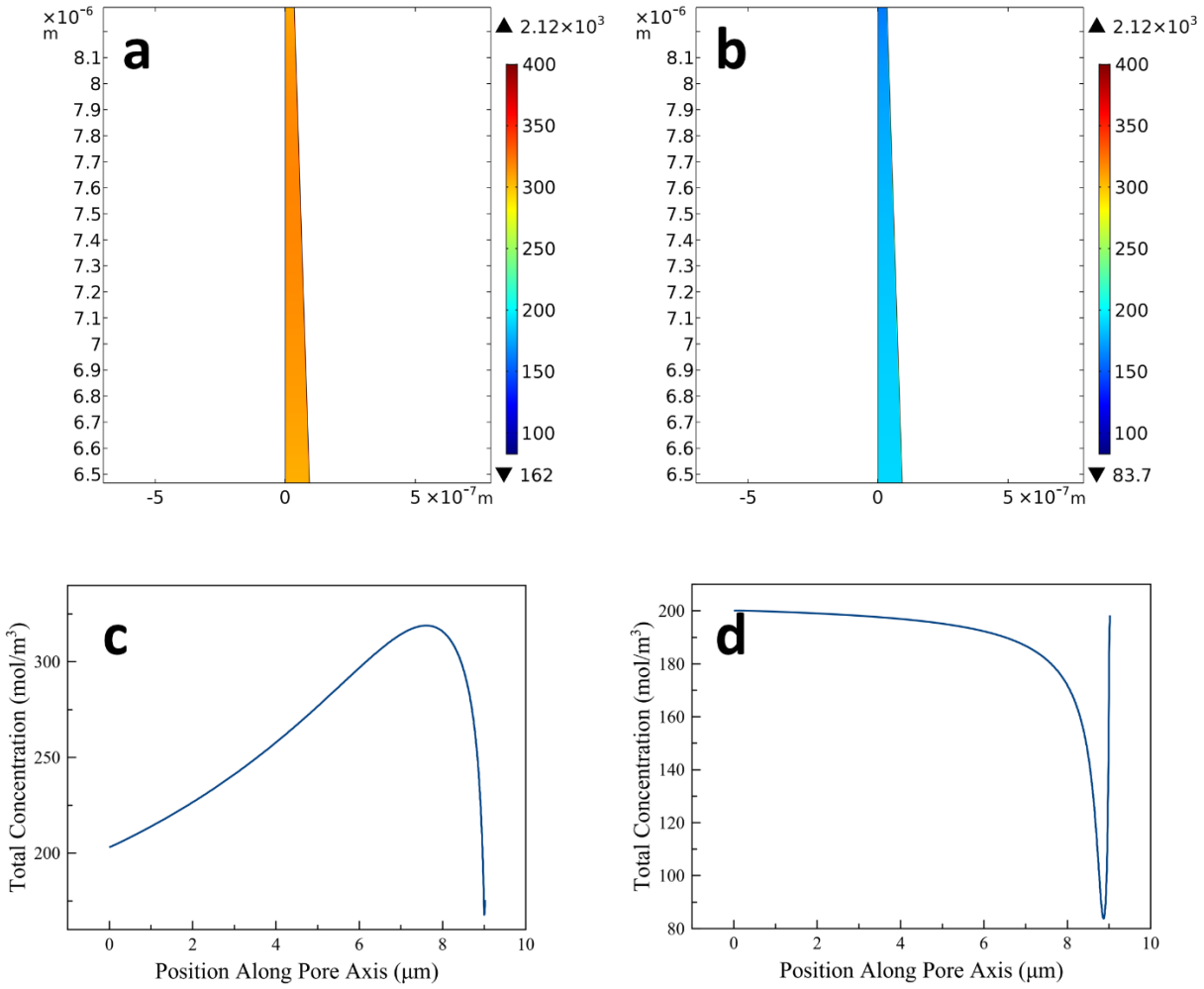

Figure 2.3: Ionic concentrations within a conical nanopore to demonstrate ion current rectification. Tip diameter is 40 nm with base diameter 600 nm. Pore length is 11 μm and system is in 100 mM bulk solution. (a,b) 2D axis-symmetric image of ionic concentrations at the tip side of a conical nanopore. (c,d) Total concentration of cations and anions along the nanopore central axis where position zero occurs at the base side of the pore. (a,c) have -1V applied on the base side while (b,d) show +1V applied at the base. The bulk solution concentration is 100 mM, giving a total ionic concentration (cations plus anions) of 200 mM. With positive voltage applied there is a clear depletion zone exhibited at the tip side of the pore while for the negative voltage polarity an enhancement of current is shown, indicating ion current rectification.

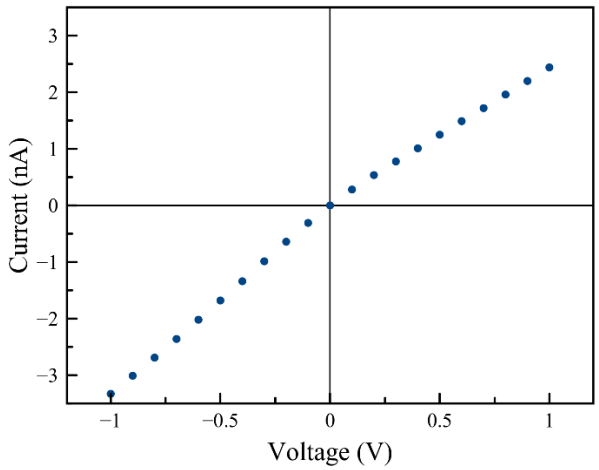

Figure 2.4: Example of a current-voltage curve exhibiting ion current rectification. This is evidenced by a current magnitude of 2.4 nA at 1V and 3.4 nA at -1 V. Current measured for a conical pore modeled in COMSOL with the same pore geometry as Figure 2.3 in 100 mM KCl. Current is measured at the ground which is placed on the tip side of the pore.

Breaking symmetry of an electrochemical potential of a nanopore can also be achieved by introducing surface charge patterns. An example of a surface charge pattern that resembles in its operation a semiconductor np junction is shown in Figure 2.5, as a junction between a zone with positive surface charges and a zone with negative surface charges. This system again creates voltage dependent ionic concentrations. For voltages of one polarity, ionic concentrations are enhanced, while for the opposite voltage polarity a depletion zone is formed, leading to a low conductance.

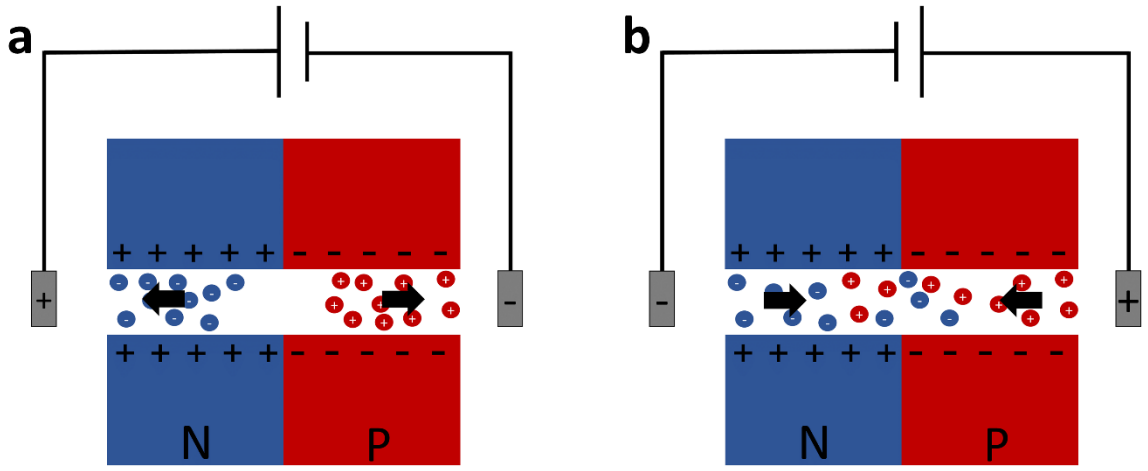

Figure 2.5: Illustration of ionic diode operation. In (a) the electrode setup demonstrates a depletion zone occurring while (b) exhibits the opposite voltage polarity allowing current flow through the junction.

This system of an ionic diode functions as an ionic switch, similar to the electronic switch created by a np junction [32].

2.5 The Poisson-Nernst-Planck-Stokes (PNPS) System

To model the activity in a nanopore a system of partial differential equations (PDEs) is used. The PNPS equations achieve equilibrium quickly in our system and as such it is sufficient to solve the equations in steady-state. The system of PDEs needs to describe both the electrostatics, the ion currents, and the fluid flow. The Poisson and Nernst-Planck equations derived in the above sections (2.1 and 2.2) describe the electric field effects. The fluid flow on the other hand is described by the Navier-Stokes (NS) equations. Together these equations form the PNPS equations.

The NS equations are three coupled second order non-linear partial differential equations that utilize the continuum approximation. The solution of these equations gives the fluid vector velocity, $\vec{u}$. These equations are derived simply using Newton's second law and basic

conservation principles. Starting with the continuity equation, which shows conservation of a quantity, we consider a given control volume (Figure 2.6). There exists an integrable quantity, φ, that is convected within a fluid with velocity $\vec{u}$. Due to conservation, the time rate of change of φ in the volume must be equal to the addition of flux through the boundaries and the sources and sinks which create or consume the fluid field. The continuity equation is then:

$$\frac{d}{dt}\int_V \varphi dV = -\int_A \varphi\vec{u}\cdot\hat{n}dA - \int_V sdV \tag{2.21}$$

where dV is the control volume, dA is the surface boundaries, $\hat{n}$ is the unit normal to the surface dA, and s is the sources and sinks present in the control volume, where sinks are positive and sources are negative.

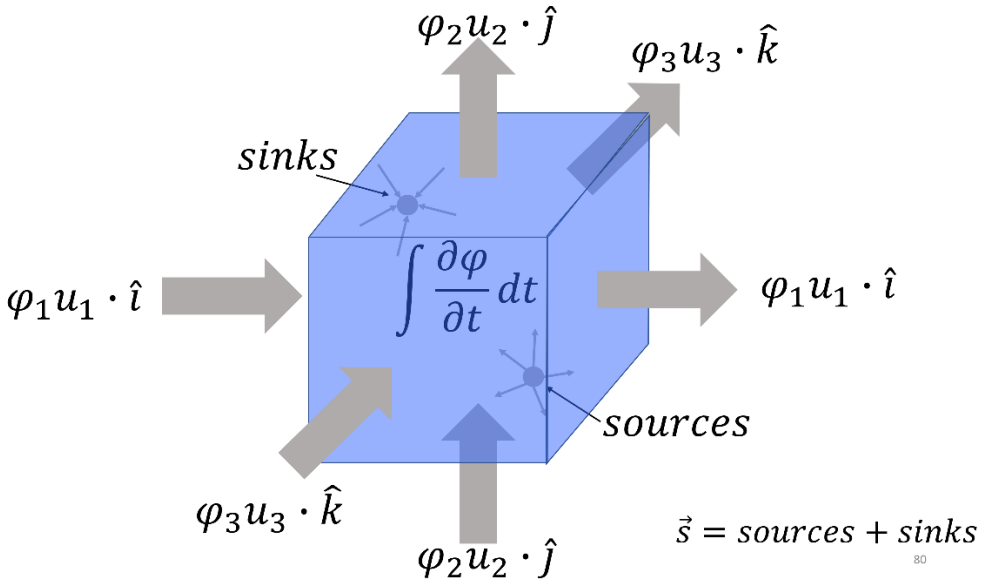

Figure 2.6: A control volume descriptive of the continuity equation 2.21.

Now if we consider the conserved quantity to be momentum, $\rho\vec{u}$, we end up with:

$$\rho \frac{\partial \vec{u}}{\partial t} + \rho \vec{u} \cdot \nabla \vec{u} = \vec{s} \tag{2.22}$$

$$\rho \frac{D\vec{u}}{Dt} = \vec{s} \tag{2.23}$$

where $\frac{D}{Dt}$ is then the material derivative. The term $\rho \vec{u} \cdot \nabla \vec{u}$ describes the transport of the momentum due to the motion of the flow field and is known as the convective term.

The next step is to replace the source and sink terms with physical terms, $\vec{s} = \vec{\nabla} \cdot \sigma + \sum_i \vec{f_i}$ where σ is the Cauchy stress tensor and $\vec{f_i}$ is a body force acting on the control volume. We can break the Cauchy stress tensor down into two separate components: a pressure tensor, p, and a stress tensor, τ, due to viscous forces. For Newtonian fluids, of which water is one, $\tau = 2\eta\varepsilon$ where η is the fluid viscosity and ε is the strain rate tensor. After this replacement we arrive at the Navier-Stokes equations:

$$\rho \frac{\partial \vec{u}}{\partial t} + \rho \vec{u} \cdot \nabla \vec{u} = -\nabla p + \eta \nabla^2 \vec{u} + \sum_i \vec{f_i}. \tag{2.24}$$

Solving these equations subject to boundary conditions gives the velocity $\vec{u}$ throughout the system. In small channels, which we considered in this work, the convective term $\rho \vec{u} \cdot \nabla \vec{u}$ is often negligible as long as fluid velocity is low. This is quantified by the Reynolds number:

$$Re = \frac{\rho u L}{\eta}. \tag{2.25}$$

Here L is the characteristic length scale of the flow which in nanopores is chosen to be the diameter. Reynolds number is the ratio of inertial forces to viscous forces within a fluid. Therefore, a high Reynolds number indicates turbulent flow, and a low Reynolds number indicates laminar flow. Nanofluidic systems are almost always in the laminar flow regime, allowing for dropping of the convective term above (in equation 2.24).

Now with the NS equations we have the whole set of PNPS equations:

$$\nabla^2\varphi = \frac{\rho_{charge}}{\varepsilon_r\varepsilon_0} \tag{2.26}$$

$$0 = \nabla\cdot\vec{j} \tag{2.27}$$

$$\vec{J_i} = F(-D_i\nabla c_i + \mu_i^{ep}c_i\nabla\varphi + c_i\vec{u}) \tag{2.28}$$

$$\rho\frac{\partial\vec{u}}{\partial t} + \rho\vec{u}\cdot\nabla\vec{u} = -\nabla p + \eta\nabla^2\vec{u} + \sum_i\vec{f_i} \tag{2.29}$$

$$0 = \nabla\cdot\vec{u} \tag{2.30}$$

where F is Faraday's constant. Here equations 2.27 and 2.30 are expressions stating incompressible flow, which is the case for our system, where the flow is constrained so that the volume of fluid elements is constant. Detailed boundary conditions such as surface charges and bulk concentrations must be used to obtain solutions and will be discussed further in the next section for a generic model.

2.6 COMSOL Multiphysics Modeling Using Finite Element Analysis

To solve the above system of partial differential equations finite element analysis (FEA) is used within a software called COMSOL. FEA leads to prediction of a systems' reaction to real forces while allowing the system to contain complex geometries. Briefly, FEA subdivides a large system into many smaller parts called finite elements. This is achieved by implementation of a mesh, which has a finite number of points discretizing the space. FEA approximates the unknown function over the domain. The simple equations modeling the finite elements are assembled into a larger system of equations that models the entire problem. FEA then uses variational calculus methods to approximate a solution by minimizing an error function.

In order to get a solution using the COMSOL software a geometry is first defined. Physics modules are added that utilize the PNPS equations described above. Using these modules, boundary conditions are defined for any charges or solution present. A mesh is created, and the study is run to produce solutions. The mesh is tuned to the point where, if the mesh elements are decreased in size, the solution results do not change. After the software is finished running, results can be tuned to produce useful data.

An example of setup and results for a generic nanopore experiment is presented here. The geometry for a cylindrical nanopore is shown in Figure 2.7a. Because this system is symmetric, a 2D axis-symmetric model can be used; here only one half-plane of the system is created and then rotated around the central pore axis in order to get the full solution. A 2D axis-symmetric model allows for a decrease in software run time compared to a 3D model. In Figure 2.7a the top and bottom squares represent electrolyte reservoirs while the elongated middle rectangle is the nanopore. Reservoir size is chosen so that it can be as small as possible, in order to decrease runtime, while still supplying sufficient number of ions so that ionic concentrations in the reservoirs do not change during simulations. If the reservoir becomes too small, the ions will become depleted and thus the solution will not be accurate.

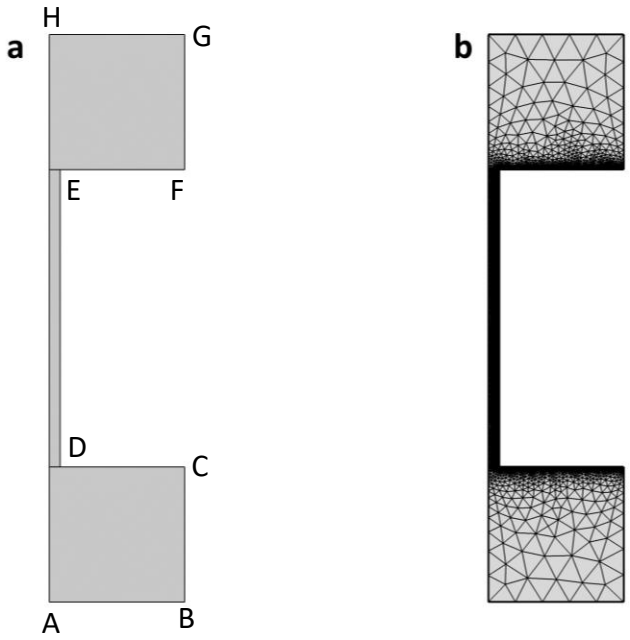

Figure 2.7: Geometry (a) and mesh (b) used in COMSOL for a cylindrical nanopore. Pore diameter is 800 nm with 11 μm length.

Once a geometry is created an initial mesh can be chosen (Figure 2.7b). It is possible to change element shape as well as number of elements over different areas of the geometry in order to achieve the best solution, with both accurate results and as low runtime as possible. After running the software, the mesh can be refined to get convergent results.

Generally, for our modeling three physics modules are used: electrostatics, transport of diluted species, and laminar flow. The first two modules listed describe the PNP system while the laminar flow module models the NS equations. The modules exchange inputs and outputs, such as electric potential, from one another in order to cohesively model the full solution. Boundary conditions must be given in each of these modules in order to calculate a solution. Examples of these boundary conditions for the geometry given in Figure 2.7 are shown in Table 2.2.

Surface	Poisson	Nernst-Planck	Navier-Stokes
HG	Constant potential $\varphi=0$	Constant concentration $c_i = 100mM$	Constant pressure p=0 No viscous stress $\mathbf{n} \cdot [\mu \ (\nabla \mathbf{u} + (\nabla \mathbf{u})^{\mathrm{T}})] = 0$
GF, CB	No charge $-\mathbf{n} \cdot (\varepsilon \nabla \varphi) = 0$	No flux $\mathbf{n} \cdot \mathbf{N}_i = 0$	No slip $\mathbf{u} = 0$
EF, ED, DC	$-\mathbf{n} \cdot (\varepsilon \nabla \varphi) = \sigma_w$	No flux $\mathbf{n} \cdot \mathbf{N}_i = 0$	No slip $\mathbf{u} = 0$
AB	Constant potential $\varphi = \mathrm{V_{app}}$	Constant concentration $c_i = 100mM$	Constant pressure p=0 No viscous stress $\mathbf{n} \cdot [\mu \ (\nabla \mathbf{u} + (\nabla \mathbf{u})^{\mathrm{T}})] = 0$
HA	Axial symmetry	Axial symmetry	Axial symmetry

Table 2.2: Boundary conditions used in example modeling results. Coupled Poisson-Nernst-Planck and Navier-Stokes equations were solved with COMSOL Multiphysics package. Surfaces are as defined in Figure 2.7a. $\boldsymbol{\varphi}, \boldsymbol{\varepsilon}, \boldsymbol{C_{bulk}}, \boldsymbol{p}, \boldsymbol{n}, \boldsymbol{N_i}, \boldsymbol{u}, \boldsymbol{\sigma_w}, \boldsymbol{V_{app}}, \boldsymbol{\mu}$ are the surface potential, dielectric constant, bulk concentration, pressure, normal vector, flux of ions, fluid velocity, surface charge density of the pore wall, applied voltage, and solution viscosity, respectively.

Once all the above steps are completed, we are ready to find a solution. The software will iterate until it gets below an error that is defined by us, in this case to be 10^{-3}. Different studies can be defined in order to run solutions for various parameters. Typically, our models are run over a voltage range that is similar to those used in our experiments. Once the model is finished running one can analyze the distribution of various parameters, including local potential, concentrations, and fluid velocity (Figure 2.8).

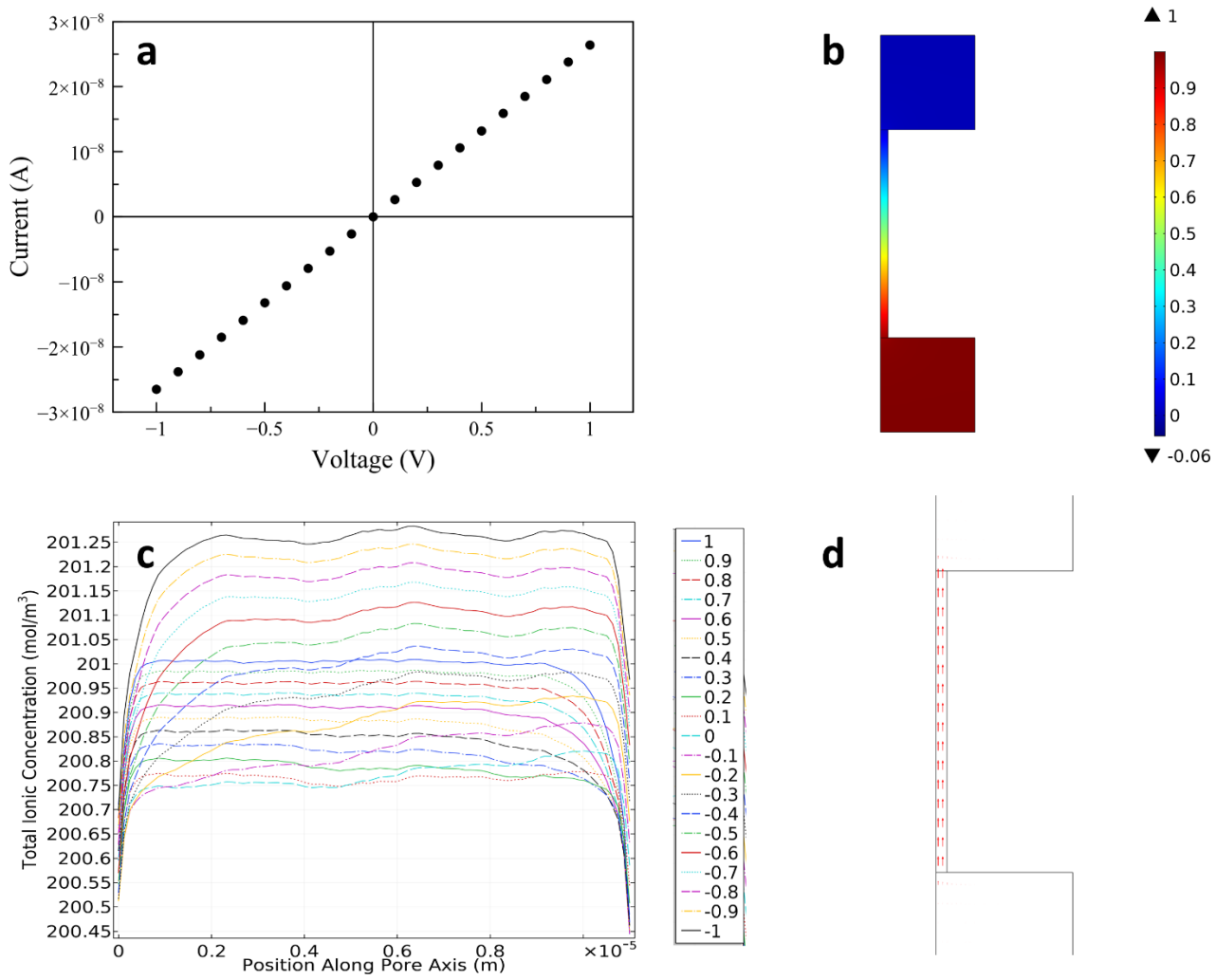

Figure 2.8: Example solution results obtained from COMSOL modeling of the geometry shown in Figure 2.7. Bulk concentration is 100 mM. (a) Typical current-voltage curve that can be compared to those taken experimentally. (b) Potential distribution within the system. Legend shows voltage (V). (c) Total concentration along the pore axis with position 0 at the pore mouth on the working electrode side. (d) Distribution of velocity within the nanopore.

CHAPTER 3

Organic Solvents' Effect on Electrokinetic Phenomena

As seen in the first two chapters, tuning of ionic current can be achieved through tailoring of pore geometry, surface charge, concentration, type of ion, and even addition of molecules. This chapter explores the combined role of type of solvent, concentration of salt, as well as voltage polarity on surface properties of pores and consequently ion transport. Ionic transport and electrokinetic phenomena are indeed very sensitive to even local changes in the pore walls characteristics. As an example, surface charges of biological channels and pores can determine which ions are transported and at which rate. Transport properties and functions of man-made pores are also affected by pattern and type of charges. On a nanoscale these finite surface charges can lead to ionic selectivity, so that a nanopore with positive surface charges will mainly transport negatively charged ions. Deviations from electrochemical symmetry within a nanopore system can lead to ion current rectification. Ion current rectification, as described in Chapter 2.4 "Ion Current Rectification", is the preferential transport of ionic current at one voltage polarity over transport at the opposite polarity, often described as a rectification factor i.e. the ratio of currents at one voltage magnitude but opposite polarities. The property of ion current rectification has been already exploited for many applications including biosensing, desalination, and energy production [33]–[37]. The majority of ion transport electrokinetic experiments with nanopores have been performed in aqueous media to mimic biological conditions. But nonaqueous media are important in many applications including energy storage devices such as batteries and capacitors as well as in chemical and biomedical separations [38]–[43]. Thus, it is crucial to

understand how surface charge properties and ion transport change when a pore is exposed to nonaqueous media. These effects are explored in this chapter through current-voltage measurements which take advantage of electroosmotic flow as well as through COMSOL modeling.

3.1 Experimental Scheme and Theory

In a study prior to this work, an experimental setup was developed to probe surface charge properties using electro-osmotically driven rectification [18]. This approach can be used with pores of any geometry and diameter. When a pore with finite surface charge is placed between two solutions that differ in conductivity, the current is rectified, and the current-voltage curve can be predicted quantitatively based on the conductance of both solutions. In the previous experiments, cylindrically shaped pores with negative surface charges were used. Depending on the voltage polarity the pore was entirely filled either with a solution of higher conductivity or one with lower conductivity. Consequently, ion current rectification occurred with rectification degree equal to the ratio of conductivities of the two solutions present on either side of the membrane. As an example, if 100 mM $LiClO_4$ and 10 mM $LiCLO_4$ were on either side of a pore, the current for positive voltages would be 7 times higher than that for negative voltages due to the fact that the conductivities of the two solutions differ by a factor of ~7. In these experiments the direction of rectification agrees with electroosmotic flow due to negative surface charges on the pore walls. Thus, with the ground electrode placed in the solution with lower concentration, positive voltages electro-osmotically fill the pore with the higher conductivity solution.

With these prior results as a basis, we begin our investigation into solvent effect on electrokinetic phenomena by confirming the dominant role of electroosmosis in inducing ion current rectification. To do this we modified the pore walls so that the effective surface charge was switched from negative to positive. This modification was achieved by electrostatic adsorption of positively charged polyelectrolyte - poly(allylamine hydrochloride) (PAH). This was done by incubating the pore in 2.5 mM PAH in pH 6 deionized water for 30 min. Both before and after the modification, the pore was exposed to an aqueous 100 mM/10 mM $LiClO_4$ gradient. It is seen in Figure 3.1 that, as expected, the current-voltage curves before and after modification were symmetric with respect to the origin of the coordinate system, thus suggesting that the surface charge indeed switched polarity. These measurements provide guidelines for the interpretation of surface charge polarity. Thusly – a pore with effective negative surface charge features positive currents that are higher than the currents for the opposite polarity and vice versa for a pore with positive surface charge.

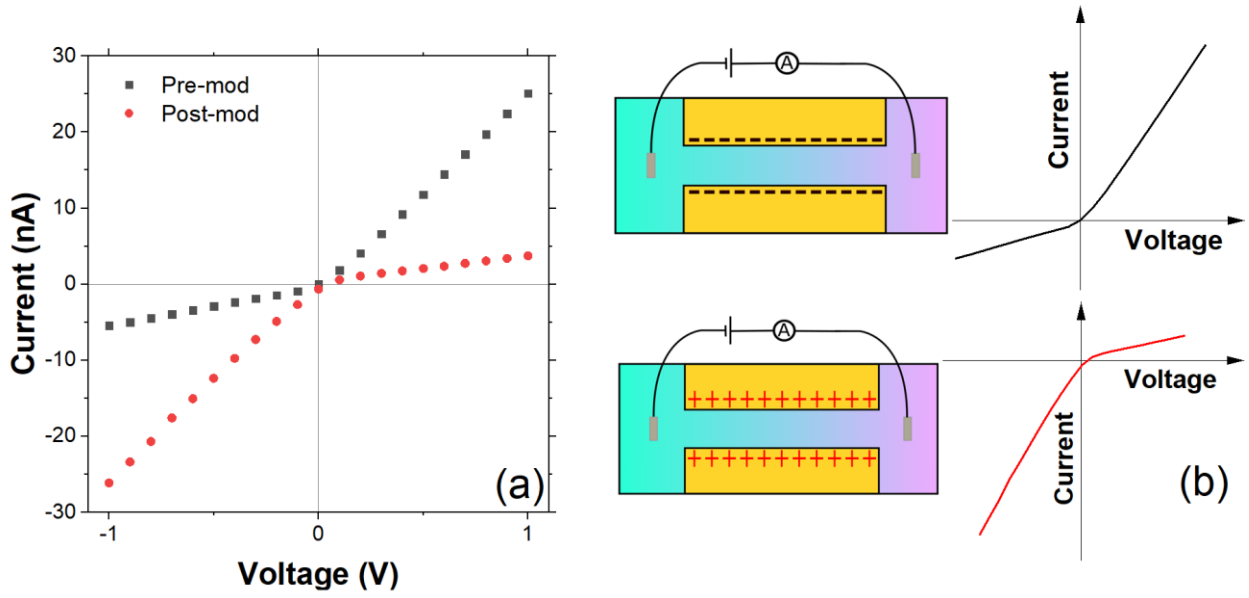

Figure 3.1: (a) Current-voltage curves of a single polymer cylindrically shaped pore with an opening diameter of 700 nm before and after modification with positively charged polyelectrolyte (PAH), which changed the surface charge from negative to positive. Aqueous 10 mM $LiClO_4$ was present on the side of the membrane in contact with the ground electrolyte, while 100 mM $LiClO_4$ was placed on the opposite side of the membrane. (b) Scheme of the experimental set-up and expected current-voltage curves for a pore with negative and positive surface charges [44]. Reprinted with permission from R. A. Lucas, C.-Y. Lin, and Z. S. Siwy, "Electrokinetic Phenomena in Organic Solvents," *J. Phys. Chem. B*, vol. 123, no. 28, pp. 6123–6131, Jul. 2019, doi: 10.1021/acs.jpcb.9b04969. Copyright 2019 American Chemical Society.

3.2 Experimental Materials and Methods

Experiments were performed with single pores prepared in 12 μm thick polyethylene terephthalate (PET) films by the track-etching technique. The process started with irradiation of the film with single heavy ions with total kinetic energy of ~GeV. The irradiation step was performed at the UNILAC accelerator at the Institute of Heavy Ions in Darmstadt, Germany. Heavy ion irradiation leads to formation of so-called latent tracks that can be further developed into pores via UV irradiation followed by wet chemical etching. Our pores were etched in 2 M NaOH at 50 °C; these conditions were shown before to lead to cylindrical geometry of PET pores. The pore diameter is known to increase with the etching

time in a linear fashion. Etching of the pore in NaOH has been shown before to lead to formation of carboxyl groups on membrane surfaces and the pore walls. The density of carboxyl groups was estimated to be ~1 per nm^2, thus as prepared PET nanopores are highly negatively charged in aqueous neutral and basic solutions.

After preparation, each pore was first characterized by its current-voltage measurement in 1 M KCl. The determined resistance is then used to estimate effective pore opening diameter assuming a cylindrical pore geometry. Using this method pores with diameters from 400 nm – 700 nm were produced. After measurements in organic solvents were performed, recordings in 1 M KCl were taken again in order to confirm the material did not undergo significant swelling and that pore diameter was stable (Figure 3.2).

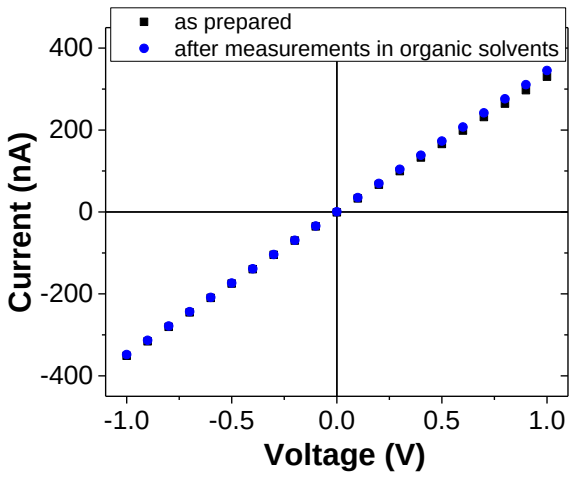

Figure 3.2: Current-voltage curves of a 700 nm in diameter pore in aqueous 1 M KCl. The recordings were done for an as prepared pore and after all measurements in propylene carbonate and acetone had been completed. This is the pore used in all experiments done with the 700 nm diameter pore [44]. Reprinted with permission from R. A. Lucas, C.-Y. Lin, and Z. S. Siwy, "Electrokinetic Phenomena in Organic Solvents," *J. Phys. Chem. B*, vol. 123, no. 28, pp. 6123–6131, Jul. 2019, doi: 10.1021/acs.jpcb.9b04969. Copyright 2019 American Chemical Society.

Conductivities of all solutions were measured using a Fisher Scientific Accumet Basic AB30 Conductivity meter. Because chemical etching etches the surface in addition to the pore track, the membrane thickness decreases from 12 to ~11 μm during this process.

Electrochemical measurements of single pores were taken by placing the membrane in a conductivity cell between two chambers filled with electrolyte (Figure 3.3). Current–voltage curves were recorded using a Keithley 6487 picoammeter/voltage source and Ag/AgCl pellet electrodes. The voltage was changed between −1 and +1 V with 0.1 V steps, between −2 and +2 V with 0.2 V steps, or between −5 and +5 V with 0.5 V steps.

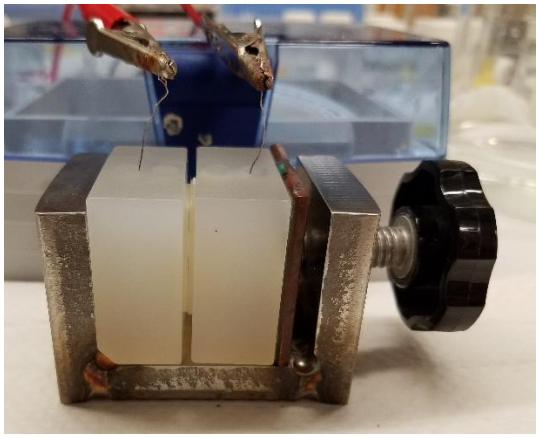

Figure 3.3: Conductivity cell setup. Two chambers of the Kel-F conductivity cell are clamped on either side of the membrane. Electrodes are placed in solution and alligator clipped to connect with a 6487 Keithley picoammeter/voltage source.

3.3 Measurements in Organic Solvents

The first set of measurements taken to investigate surface properties in organic solvents was done in the presence of alcohols. The same 700 nm in diameter pore was used as in the guideline experiment of Figure 3.1. Figure 3.4 shows current-voltage measurements in symmetric salt conditions but with varying ethanol content on only one side of the

membrane. The solutions with ethanol have lower conductivity than the fully aqueous solution present on the other side of the membrane. We also expected that in alcohol solutions, the pore walls would still be negatively charged, although the charge density could be lower than in aqueous media [45]. Therefore, with the working electrode on the fully aqueous side, we predicted the pore would be filled with the fully aqueous solution for positive voltages such that the positive currents would be higher than negative currents. Results in Figure 3.4 confirm these expectations and suggest that the surface charge density is sufficient to induce electroosmotic filling of the pore. Rectification degrees were also calculated, as the ratio of currents at +1V and -1V, and were found to be equal to the ratios of solution conductivities (Figure 3.4b), providing support for the claim that the pore was filled with the solution on either side of the membrane.

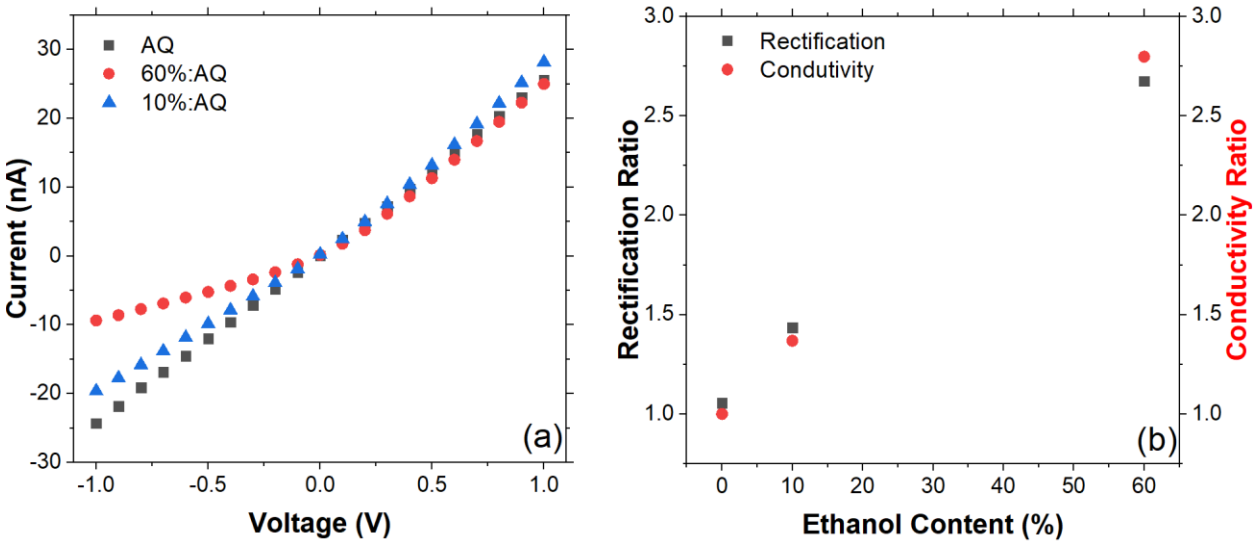

Figure 3.4: (a) Current-voltage curves through a single PET pore placed in contact with an aqueous solution of 100 mM $LiClO_4$ on one side, and 100 mM $LiClO_4$ solution in water/ethanol mixtures on the other side. (b) Rectification degree calculated as a ratio of currents at +1V and -1V together with the ratio of conductivities: conductivity of the aqueous solution and of water/ethanol mixtures. The pore had a diameter of 700 nm [44]. Reprinted with permission from R. A. Lucas, C.-Y. Lin, and Z. S. Siwy, "Electrokinetic Phenomena in Organic Solvents," *J. Phys. Chem. B*, vol. 123, no. 28, pp. 6123–6131, Jul. 2019, doi: 10.1021/acs.jpcb.9b04969. Copyright 2019 American Chemical Society.

A similar set of experiments was performed with $LiClO_4$ in methanol/water mixtures, which gave similar results and conclusions as seen for the experiments with ethanol/water-based solutions (Figure 3.5).

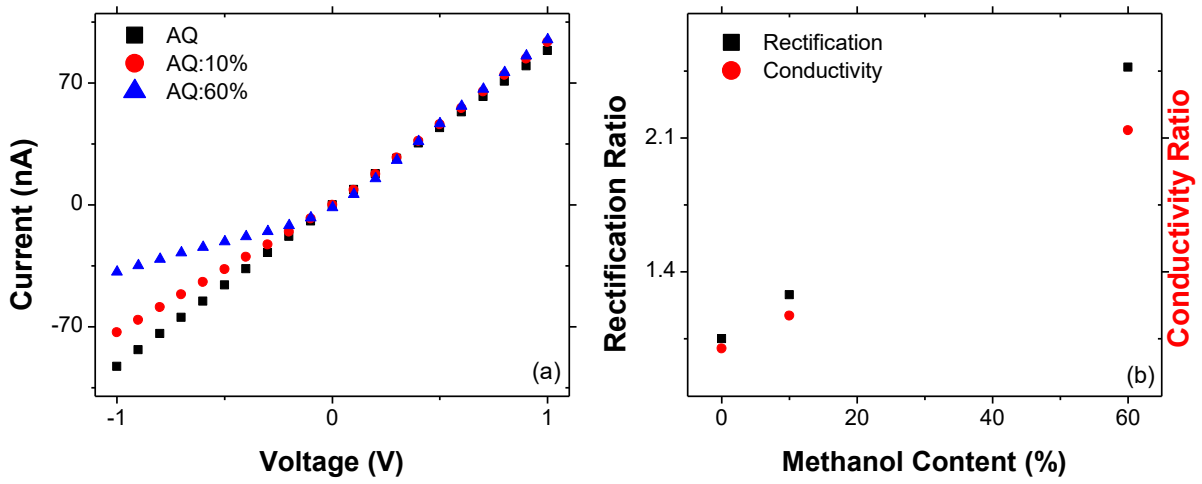

Figure 3.5: (a) Current-voltage curves of a single PET pore placed in contact with an aqueous solution of 100 mM KCl on one side, and 100 mM KCl solution in water/methanol mixtures on the other side. (b) Rectification degree calculated as a ratio of currents at +1V and -1V together with the ratio of conductivities: conductivity of the aqueous solution and of the water/methanol mixtures. The pore had a diameter of 400 nm [44]. Reprinted with permission from R. A. Lucas, C.-Y. Lin, and Z. S. Siwy, "Electrokinetic Phenomena in Organic Solvents," *J. Phys. Chem. B*, vol. 123, no. 28, pp. 6123–6131, Jul. 2019, doi: 10.1021/acs.jpcb.9b04969. Copyright 2019 American Chemical Society.

As the next step, solutions of the same salt, $LiClO_4$, in organic solvents, such as propylene carbonate and acetone, were used as the background electrolyte. Because propylene carbonate is a polar aprotic solvent, we expected that the surface carboxyl groups of PET would not deprotonate and the pore walls would remain neutral. However, it was previously shown that propylene carbonate could induce positive surface charge on surfaces, such as PET pores, even if they were negatively charged in water-based solutions [46]. It was hypothesized that the flip in surface charge polarity in propylene carbonate stemmed from a partial ordering of the solvent molecules that are characterized by a high dipole moment of almost 5 D as well as adsorption of lithium ions [46]–[51]. These measurements were done

in conically shaped nanopores and did not allow for the deconvolution of rectification occurring due to solution properties versus pore properties. Thus, in order to evaluate the role of lithium ions in the formation of positive charge, surface properties were probed using a cylindrically shaped mesopore. With this pore shape, no rectification is induced by the pore geometry and solution/surface properties can be probed directly. Therefore, if lithium ions are necessary to obtain a positive surface charge, different directions of ion current rectification should be observed in low versus high concentrations of $LiClO_4$. Two sets of experiments were performed to test this hypothesis. The first set utilized two gradients of 100mM/1mM and 10mM/1mM $LiClO_4$ (Figure 3.6b). In the second set the low concentration was kept constant at 10 mM $LiClO_4$, and the opposite side of the membrane was gradually increased from 10 mM to 500 mM (Figure 3.6c).

The character of the IV curves recorded in the two sets of experiments is indeed very different. In the 10 mM/1 mM gradient, the pore behaves as an Ohmic resistor suggesting that at these conditions the pore did not carry any excess surface charge. The curves recorded in the 100 mM/ 1mM gradient as well as all other gradients with 10 mM solution on one side of the membrane rectified in a direction indicating the effecting charge of the pore walls was positive. Rectification ratio compared with ionic conductivity ratio showed lack of agreement for these cases. This suggests that the charge density of the pore surface could be dependent on salt concentration or even voltage.

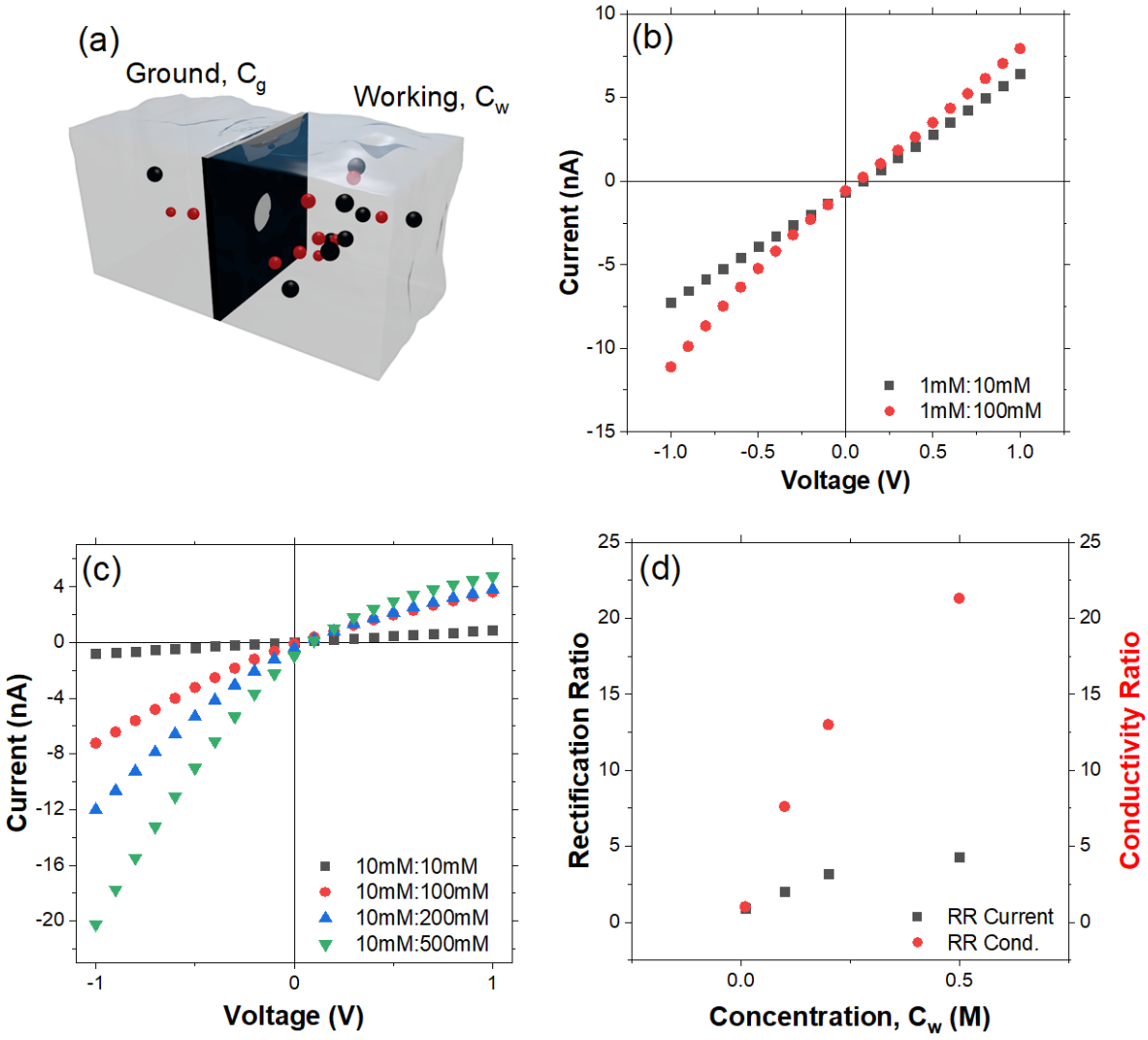

Figure 3.6: (a) Scheme of the experimental setup. The ground electrode was placed in the solution with lower salt concentration. (b–d) Experimental data for a 700 nm in the diameter PET pore placed in contact with gradients of $LiClO_4$ concentration in propylene carbonate. Current–voltage curves together with rectification degrees and ratios of ionic conductivities. (d) Analysis of IV curves shown in (c) with the $LiClO_4$ concentration of 10 mM kept constant on the side of the membrane with the ground electrode; salt concentration on the opposite side of the membrane was changed between 10 and 500 mM. Rectification was calculated as the ratio of currents at −1 and +1 V [44]. Reprinted with permission from R. A. Lucas, C.-Y. Lin, and Z. S. Siwy, "Electrokinetic Phenomena in Organic Solvents," *J. Phys. Chem. B*, vol. 123, no. 28, pp. 6123–6131, Jul. 2019, doi: 10.1021/acs.jpcb.9b04969. Copyright 2019 American Chemical Society.

In order to understand the dependence of charge density on lithium-ion concentration a new set of experiments was performed. It was hypothesized that charge density should increase with the increase of $LiClO_4$ concentration until a certain threshold value where the effective

charge density would saturate and remain unchanged. This was tested by holding the high concentration solution constant at 700 mM $LiClO_4$ and varying the concentration on the other side of the membrane from 10 mM to 500 mM (Figure 3.7a,c). Again, we see that the IV curves are rectifying in a direction that suggests the pore is effectively positively charged. In this case it is seen that the rectification degrees were in good agreement with conductivity ratios suggesting that the surface charge indeed saturated at ~100mM $LiClO_4$.

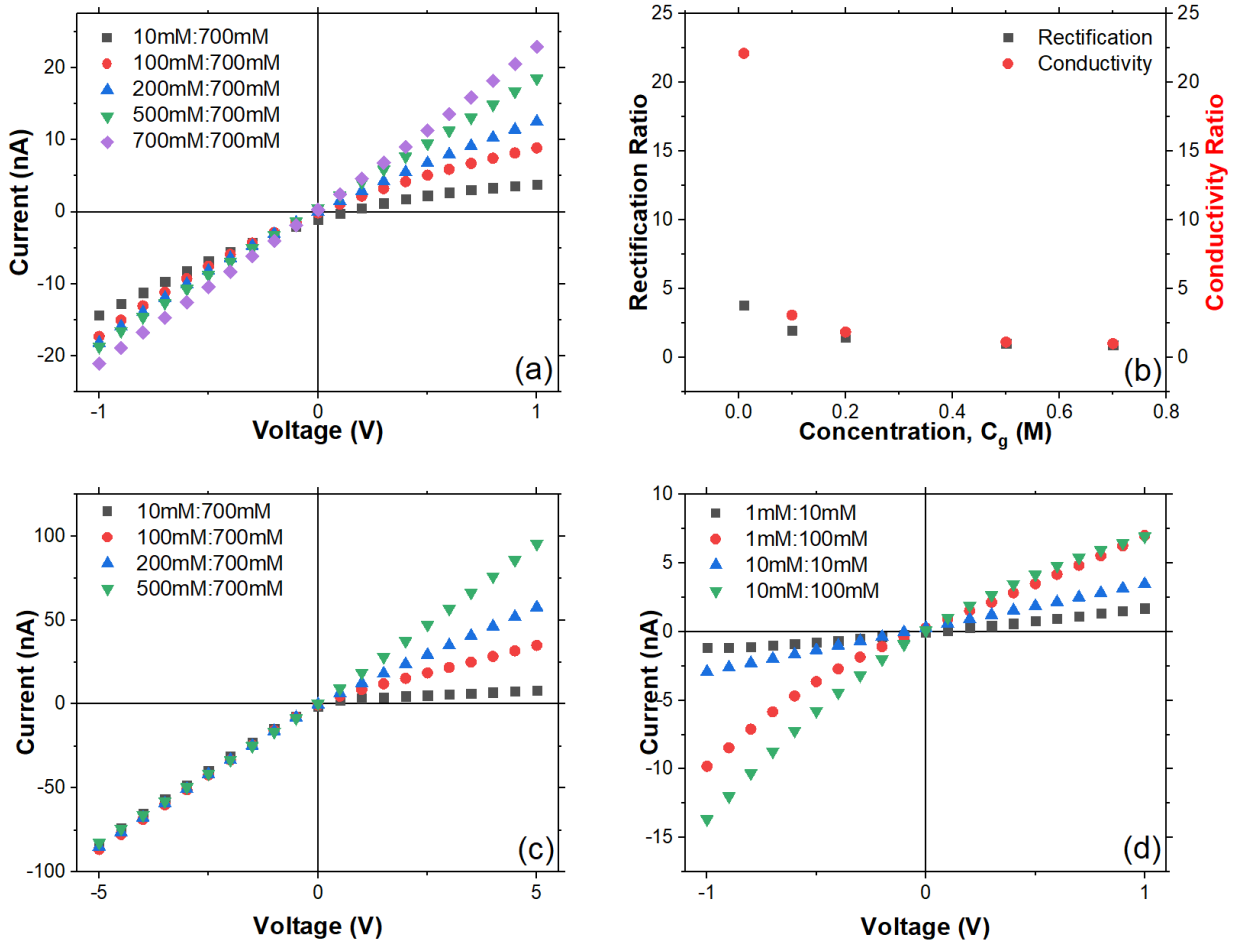

Figure 3.7: (a–c) Current–voltage curves for a single PET pore in $LiClO_4$ concentration gradients in propylene carbonate together with conductivity ratios and rectification degrees calculated based on currents measured at ±1 V. Note that panels (a,c) show behavior of the same pore in two different voltage ranges. (d) Current–voltage curves recorded when a pore was in contact with $LiClO_4$ gradients in acetone. The ground electrode was placed in the solution with lower salt concentration. All recordings were performed with a 700 nm diameter pore [44]. Reprinted with permission from R. A. Lucas, C.-Y. Lin, and Z. S. Siwy, "Electrokinetic

Phenomena in Organic Solvents," *J. Phys. Chem. B*, vol. 123, no. 28, pp. 6123–6131, Jul. 2019, doi: 10.1021/acs.jpcb.9b04969. Copyright 2019 American Chemical Society.

Finally, one last set of experiments was performed using another organic solvent, acetone, and the same salt, $LiClO_4$. Similar to the results seen in propylene carbonate, the walls of PET became effectively positively charged when the $LiClO_4$ concentration in acetone exceeded 10 mM. For the gradient, 10 mM/1 mM $LiClO_4$, the pore rectified in a direction suggesting the pore was still effectively negatively charged. Experiments in both propylene carbonate and acetone solutions of $LiClO_4$ provided evidence that the switch of the polymer walls surface charge occurs only when a threshold concentration of lithium ions is exceeded. The possible role, postulated before, of ordering of the solvent molecules on the distribution of ions at the interface and formation of the effective positive charge will be studied by us in the future.

3.4 Modeling of System Response

The experimental results were modeled using coupled Poisson-Nernst-Planck (PNP) and Navier-Stokes (NS) equations solved using finite element analysis through COMSOL. Similar to our experimental set-up, in the modeling a 700 nm in diameter and 11 μm in length pore was placed between two solution reservoirs. The reservoir that is grounded always contains the lower salt concentration. To solve the coupled PNP-NS equations it was assumed that the charge density on the pore walls was lithium-ion concentration dependent through adsorption. A sigmoid function was used due to the fact that Li^+ concentration can change both magnitude and sign of the surface charge density:

$$\sigma_W = a + \left(\frac{b}{1 + c\, e^{-d[Li^+]_s}}\right)$$

Here $[Li^+]_s$ is the molar concentration of lithium ions on the pore surface, dependent on bulk concentration, salt gradient, and voltage. Coefficients *a*, *b*, *c*, and *d* are function controlling parameters for determining charge density. Two cases were considered by choosing different coefficients for surface charge properties of two different solvents: propylene carbonate and acetone. Values chosen for the coefficients for these two cases are shown in Table 3.1 below.

Solvent	**a**	**b**	**c**	**d**
Propylene carbonate	-0.2	80	1325	0.12
Acetone	-10	90	21.7	0.1

Table 3.1: Values of parameters chosen to fit surface charge equation for propylene carbonate and acetone.

Figure 3.8 shows the simulated IV curves agree well with the experimental results. For the 100 mM/10 mM concentration gradient the rectification indicates positive surface charge for both solvent types. For the 10 mM/1 mM $LiClO_4$ gradient the current-voltage curve for the propylene carbonate solutions is linear, as seen experimentally; for the acetone solutions, the pore rectifies in the direction indicating negative surface charge, again as seen experimentally. A different concentration gradient, 100 mM/1 mM is shown in Figure 3.9 and confirms that effective surface charge density depends on both solvent and salt concentration.

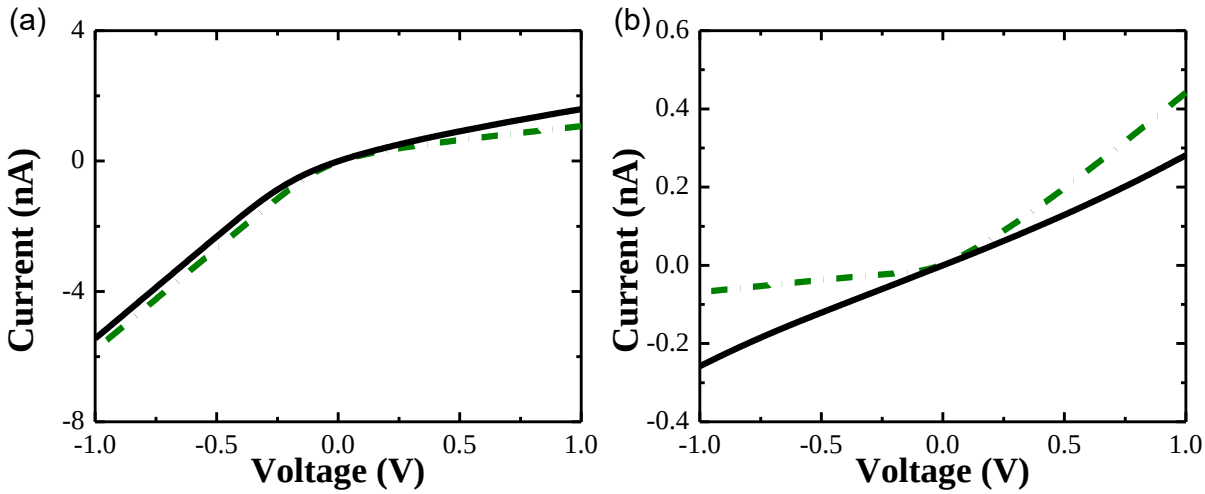

Figure 3.8: Numerically predicted current-voltage curves of a single mesopore placed in contact with a salt concentration gradient. The model considers dependence of surface charge density on the pore wall on Li^+ concentration. Simulated current-voltage curves of an 11 μm long cylindrical pore with the pore diameter of 700 nm for various $LiClO_4$ concentration gradients. (a) C_{high}=100 mM and C_{low}=10 mM; (b) C_{high}=10 mM and C_{low} =1 mM. Black and green curve were obtained using charge density calculated as denoted for propylene carbonate and acetone, respectively [44]. Reprinted with permission from R. A. Lucas, C.-Y. Lin, and Z. S. Siwy, "Electrokinetic Phenomena in Organic Solvents," *J. Phys. Chem. B*, vol. 123, no. 28, pp. 6123–6131, Jul. 2019, doi: 10.1021/acs.jpcb.9b04969. Copyright 2019 American Chemical Society.

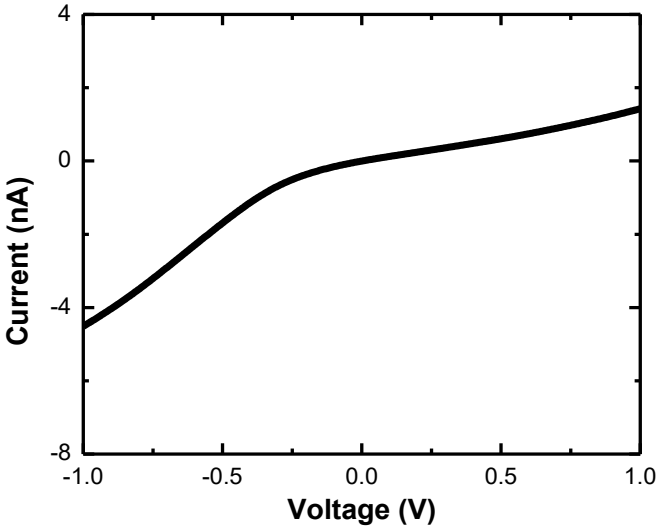

Figure 3.9: Simulated current-voltage curves of a 700 nm in diameter and 11 μm in length cylindrical pore for $LiClO_4$ concentration gradient of C_{high}/C_{low}=100 mM/1 mM. The density of surface charges depends on lithium ion concentration according to the case given for propylene carbonate [44]. Reprinted with permission from R. A. Lucas, C.-Y. Lin, and Z. S. Siwy, "Electrokinetic Phenomena in Organic Solvents," *J. Phys. Chem. B*, vol. 123, no. 28, pp. 6123–6131, Jul. 2019, doi: 10.1021/acs.jpcb.9b04969. Copyright 2019 American Chemical Society.

To investigate the results further, the axial variation of the surface charge for various experimental conditions is plotted in Figures 3.10 and 3.11. Due to the salt gradient across

the pore, the concentration of lithium ions is dependent on the position along the pore axis. At the concentration gradient of 100 mM/10 mM, for the case of propylene carbonate in Figure 3.10, the pore surface is positively charged for both positive and negative voltage polarities, though with the charge density dependent on voltage polarity. A higher charge density is seen for negative voltages where the pore is filled with the more concentrated salt solution. At -1V and the gradient of 100 mM/10 mM, the charge density is almost position-independent because 100 mM is the concentration where charge density reaches its maximum value and allows for a complete electro-osmotic filling of the pore. The concept of salt concentration-dependent charge density is visibly seen for +1V where the side of the pore in contact with 100 mM demonstrates positive surface charge and the opposite side of the pore in contact with 10 mM shows a neutrally charged surface. For the salt concentration gradient 10 mM/1 mM in acetone the pore is suspected to have a negative surface charge. This is verified through both modeling and experiments (Fig. 3.11b and Fig. 3.7d). However, for the case of propylene carbonate in this same concentration gradient, the surface charge is close to zero as confirmed by charge distribution along the pore axis (Figure 3.10b). No rectification was observed for this case in either modeling or experiments. Figures 3.10 and 3.11 also show surface charge of a pore in a concentration gradient at 0V. As expected, if no bias is applied, the surface charge density changes in a linear fashion along the pore axis. Both the external voltage in combination with the concentration gradient as well as cation adsorption synergistically lead to tunable charge density and rectification.

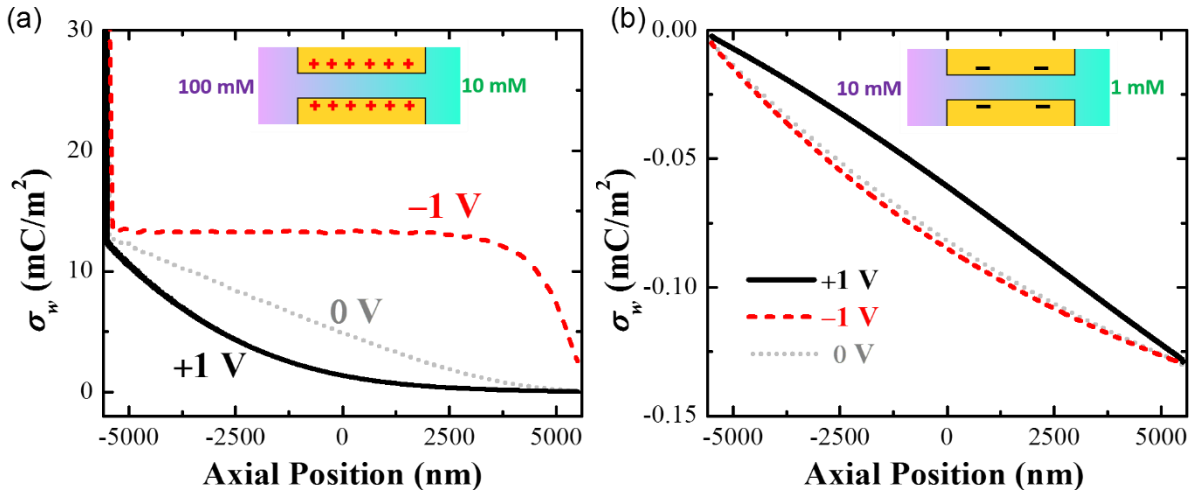

Figure 3.10: Axial variation of surface charge density of the pore wall σ_w at three levels of applied voltage for conditions for propylene carbonate surface charge density. (a) C_{high}=100 mM and C_{low}=10 mM; (b) C_{high}=10 mM and C_{low} =1 mM [44]. Reprinted with permission from R. A. Lucas, C.-Y. Lin, and Z. S. Siwy, "Electrokinetic Phenomena in Organic Solvents," *J. Phys. Chem. B*, vol. 123, no. 28, pp. 6123–6131, Jul. 2019, doi: 10.1021/acs.jpcb.9b04969. Copyright 2019 American Chemical Society.

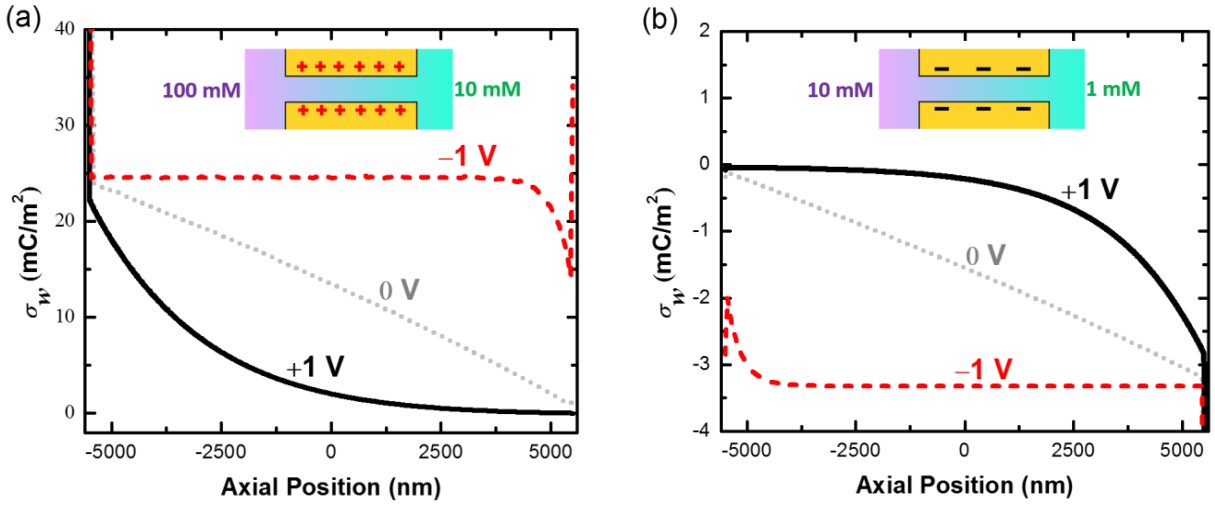

Figure 3.11: Axial variation of surface charge density of the pore wall σ_w at three levels of applied voltage for surface charge density described for acetone. (a) C_{high}=100 mM and C_{low}=10 mM; (b) C_{high}=10 mM and C_{low} =1 mM [44]. Reprinted with permission from R. A. Lucas, C.-Y. Lin, and Z. S. Siwy, "Electrokinetic Phenomena in Organic Solvents," *J. Phys. Chem. B*, vol. 123, no. 28, pp. 6123–6131, Jul. 2019, doi: 10.1021/acs.jpcb.9b04969. Copyright 2019 American Chemical Society.

In this work, we successfully demonstrated a method to probe effective charge of surfaces via electroosmosis induced rectification in pores that are in contact with solutions that differ

in ionic conductivity. The dependence of surface charge on type of solvent, salt concentration, and voltage can be mapped using this approach. Our experiments provided evidence that a polymer carboxylated surface can switch surface charge polarity from negative in aqueous media to positive in propylene carbonate and acetone containing $LiClO_4$. Increase of the salt concentrations leads to increase of the positive charge density; at concentrations greater than or equal to ~100 mM the positive charge density saturated in both propylene carbonate and acetone-based solutions. This work helps our overall understanding of the effective surface charge in organic solvents and its impact on ionic transport. It will inspire future studies to unravel the molecular details at the solid/liquid interface. Numerical modeling was developed and can be used for systems with varying charge density along a surface due to experimental conditions. In the future, the mechanism of lithium-ion adsorption and the structure of the electrical double layer in organic media will be investigated through experiments in a range of different salts and solvents with varying dielectric constants. This direction of research will provide new ways of controlling transport on nano- and mesoscales.

CHAPTER 4

Ionic Circuits with Ionic Bipolar Junction Transistors

For many years scientists have been interested in creating ionic equivalents of electronic devices in order to manipulate ionic and molecular signals in a solution [52]–[58]. Biological ion channels have been providing excellent examples of a similar type of signal manipulation since existence. Thus, inspired by both electronics and biology, ionic circuit components have been created, for example, with nanopores due to their large surface-to-volume ratios which provide transport dependent on surface properties. One of the first ionic components created was the ionic diode which allows the flow of current at one voltage polarity but produces a depletion zone at the opposite voltage polarity [10]. One of the most promising ionic circuit components is the transistor which can be used to precisely control and amplify current within circuits. Combination of transistors into ionic circuits allows for complex operations including increase of amplification from that of an individual transistor. This chapter explores the creation and characterization of such a system. The unique properties offered by ionic transistors can be used for a variety of applications such as making headway towards a more accurate emulation of a biological neuron. Ionic amplification is observed in this system in addition to spatially and chemically complex ion transport. A neuron enables relaying of signals over macroscopic distances without any losses; this is followed by selective release of ions and molecules at the presynaptic terminal, diffusion in the confined space of the synaptic cleft, and selective uptake in the post-synaptic cleft [59]. Realizing a system like this has been out of the range of current technologies. Ionic transistor applications also include the possibility of utilizing the amplifying device to measure

currents from biological nanochannels that produce signals below the detection limit of solid-state technology, such as the Na^+-glucose cotransporter which plays a key role in dietary uptake of glucose [60], [61].

4.1 The Ionic Bipolar Junction Transistor Scheme and Theory

Inspiration of ionic bipolar junction transistors is taken from their solid-state counterparts. A solid-state BJT is composed of three regions called emitter, base and collector that are doped semiconductors. In an npn (pnp) BJT, the emitter and collector are n-doped (p-doped) and the base is p-doped (n-doped). These regions are stacked on one another such that there are two junctions between the three charged regions. These junctions can be controlled, by biasing three separate electrical connections, either to allow or block current flow across them. Depending on the number of blocked junctions, one can distinguish the three modes of operation of BJTs. In the on state, also called saturation mode of the device, current flows across both junctions. In the off state, current flows across neither junction, and the so-called cut-off mode is created. And finally, if current flows only across one junction of the transistor, the device is in a mode called active mode. This is the only mode allowing amplification (Figure 4.1).

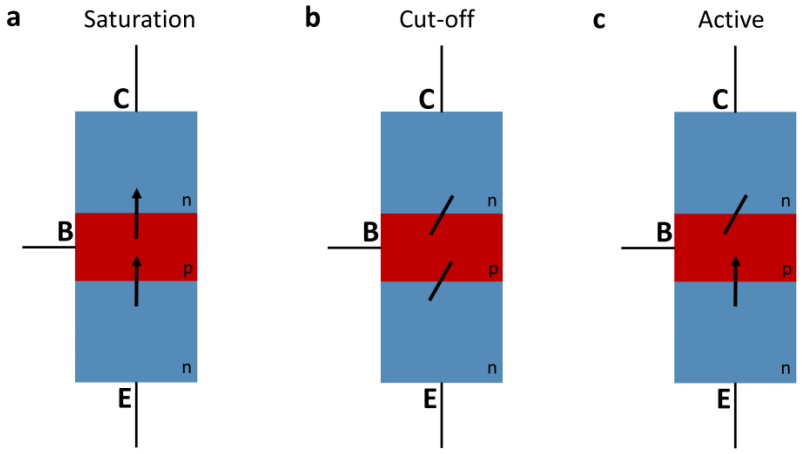

Figure 4.1: Solid-state npn bipolar junction transistor scheme and modes of operation. (a) Saturation mode, or the on-state, allows current flow across both diode junctions. (b) Cut-off mode has current flow across neither junction and thus is the off-state of the device (c) Active mode allows current flow across only one junction. This is the only mode capable of producing amplification.

In an electronic transistor these three modes of operation correspond to specific voltage ranges for each electrode (Table 4.1). It is expected that an ionic equivalent should behave similarly for similar voltage ranges.

Voltage Relations	NPN Mode	PNP Mode
$V_e < V_b < V_c$	Active	Reverse active
$V_e < V_b > V_c$	Saturation	Cut-off
$V_e > V_b < V_c$	Cut-off	Saturation
$V_e > V_b > V_c$	Reverse active	Active

Table 4.1: Mode of operation dependent on voltage range of each electrode for both npn and pnp type transistors [62]. Here V_e, V_b, and V_c are voltage at the emitter, base, and collector, respectively.

BJTs can be operated in three different configurations called common-emitter, common-collector, or common-base. The collector refers to the high voltage contact, on one side of the device. The emitter is the low voltage contact on the other side of the device and

finally, the base is the gate placed in the middle of the device (Figure 4.2). The word 'common' refers to which contact is grounded. One of the three configurations is chosen based on which types of amplifications are desired. Common-emitter allows both current and voltage gain, common-collector only allows current gain, and common-base provides only voltage gain. For the ionic device created here the common-emitter configuration was used with the low contact grounded. Therefore, the solid-state equivalent of this configuration is displayed in Figure 4.2.

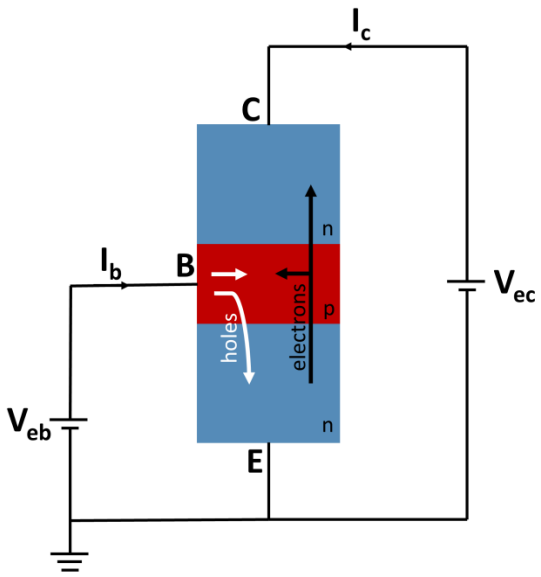

Figure 4.2: Common-emitter circuit setup for solid-state npn transistor. Here C, B, and E are collector, base, and emitter respectively. I_b and I_c represent base and collector current respectively. V_{ec} and V_{eb} are collector voltage and base voltage [12]. Reprinted with permission from R. A. Lucas, C.-Y. Lin, L. A. Baker, and Z. S. Siwy, "Ionic amplifying circuits inspired by electronics and biology," *Nature Communications*, vol. 11, no. 1, Art. no. 1, Mar. 2020, doi: 10.1038/s41467-020-15398-3.

Transitioning from a solid-state device to an ionic one we want to use a similar concept of doping. In nanopores, it is the surface charge that determines which type of ions (positive or negative) are the majority charge carrier in the nanopore interior, see Chapter 2.2 "The Electrical Double Layer". When a pore is placed in contact with a salt solution such that the pore radius is comparable to the Debye length, it can be assumed that the pore is

predominantly filled with counterions. For example, if the pore surface is positively charged it will contain a higher concentration of anions, creating the ionic equivalent of an 'n' semiconductor. If instead the pore walls are negatively charged the pore contains a higher density of cations, creating a 'p' equivalent (Figure 4.3). In principle, the ionic device will have the same modes of operation as the solid-state one.

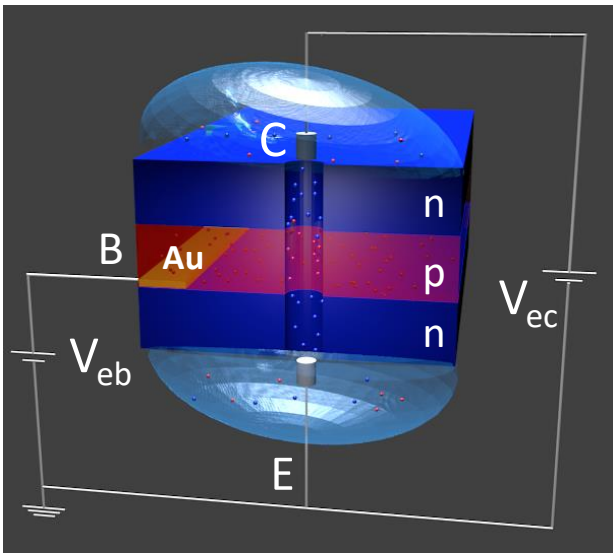

Figure 4.3: Ionic equivalent of electronic npn transistor [12]. Reprinted with permission from R. A. Lucas, C.-Y. Lin, L. A. Baker, and Z. S. Siwy, "Ionic amplifying circuits inspired by electronics and biology," *Nature Communications*, vol. 11, no. 1, Art. no. 1, Mar. 2020, doi: 10.1038/s41467-020-15398-3.

4.2 Realization of a single Ionic Bipolar Junction Transistor (IBJT)

An IBJT was assembled using two 40 nm thick silicon nitride films on a silicon support. The two films were bound together by a spin-coated Nafion layer between them. The thickness of the Nafion layer was estimated by scanning electron microscope (SEM) to be ~ 1 μm (Figure 4.4a). Once the chips were assembled a cyanoacrylate glue was applied around the stack to hold it together. The device has three terminals which provide voltage to the

transistor. The collector produces the working voltage across the nanopore, V_{ec}, while the base provides voltage, V_{eb}, at the gate electrode in the middle of the device, as show in Figure 4.3. A 10 nm layer of gold sputter-coated onto one of the silicon nitride surfaces prior to Nafion spin-coating is utilized as the gate electrode.

Two types of IBJT were prepared that differed in the diameter and alignment of pores (Figure 4.4c,d). To prepare the first type of IBJT (Figure 4.4c), a stack of SiN/Nafion/SiN was created as described above, and focused ion beam (FIB) was used to drill a nanopore through the entire structure. Due to ~ 1 micron thickness of the stack, the diameter of the drilled pore was at least 200 nm to make sure the pore reached through the entire structure. Devices prepared using this method had diameters between 200 and 600 nm. Because ion beams have a damaging effect on polymers, it was assumed the region with Nafion would have an opening wider than the pore diameter visible from the top view of the silicon nitride. This difference in opening was found to be no larger than the factor of three according to SEM measurements (Figure 4.4b). The final step in device fabrication was to impart positive surface chare on the silicon nitride pore walls and external surfaces. To this end, a silanization reaction with amine terminated silanes was performed. This reaction targets silanol groups alone so that it should not modify the Nafion. With the device completed the Nafion acts as a cation source due to its negative charge. Thus, when positive voltage is applied to the base, cations are forced into the pore which increases the collector current. If instead negative gate voltages are applied, cations are brought towards the base electrode and the collector current will decrease.

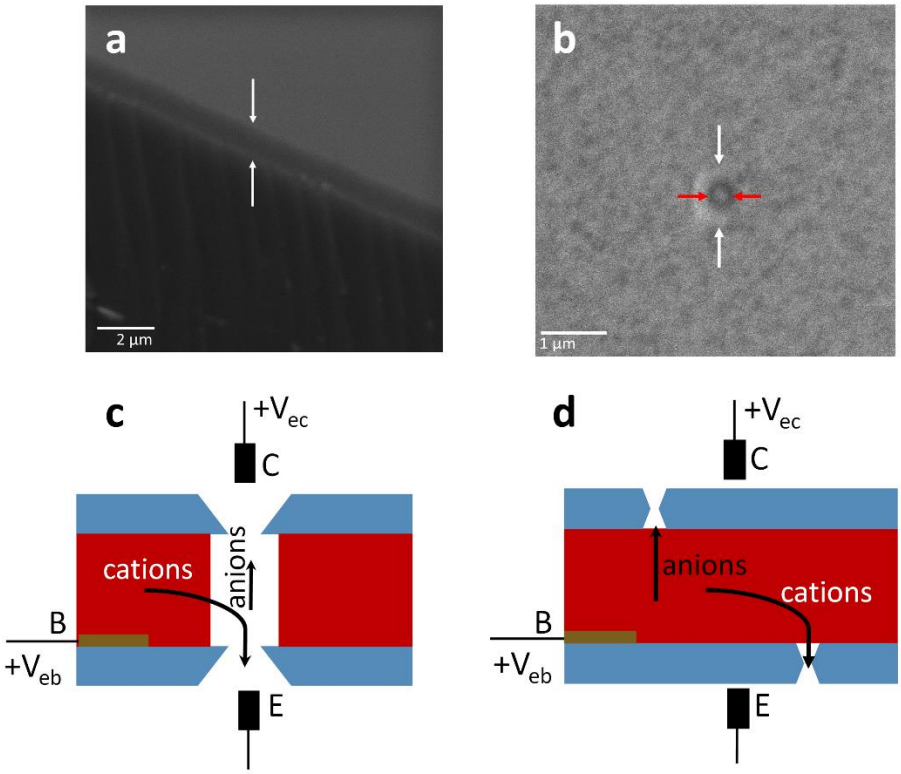

Figure 4.4: (a) Scanning electron microscope (Tescan GAIA3) image of a cleaved silicon nitride chip with Nafion layer on top. Spin coating conditions were the same as those used in preparation of devices. White arrows indicate the Nafion layer. (b) A pore drilled with focused ion beam through a silicon nitride chip with a Nafion layer on top. Fabrication conditions were similar to those used for device preparation. Red arrows indicate the diameter of the pore. White arrows indicate the diameter of the damaged Nafion surrounding the pore. (c) Arrangement of the two 40 nm thick silicon nitride chips (shown in blue) and the Nafion film (red) used in the ionic transistor. A pore through the silicon nitride and Nafion sandwich was drilled by focused ion beam. Here blue is representative of a positive surface charge and red of a negative surface charge. (d) Device scheme for the transistors with smaller pore size. This transistor was assembled using two silicon nitride chips with nanopores drilled prior to the device assembly [12]. Reprinted with permission from R. A. Lucas, C.-Y. Lin, L. A. Baker, and Z. S. Siwy, "Ionic amplifying circuits inspired by electronics and biology," *Nature Communications*, vol. 11, no. 1, Art. no. 1, Mar. 2020, doi: 10.1038/s41467-020-15398-3.

We also prepared another type of stacked devices that consisted of pores with a smaller opening diameter (Figure 4.4d). For this route of device fabrication, FIB was first used to drill individual nanopores in the two silicon nitride chips separately. The chips were then subject to the silanization reaction to render them positively charged. Because the drilling thickness in this case is only 40 nm thick, nanopores as small as ~100 nm in diameter were producible. After silanization, each chip was spin-coated with Nafion and assembled

into a device using an optical microscope (Figure 4.5). Note that in this type of IBJT, the two nanopores are not aligned.

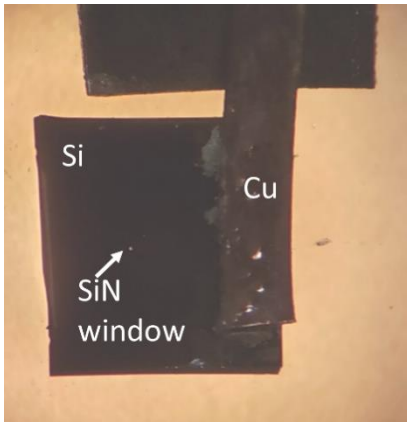

Figure 4.5: Optical microscope image of an assembled device. Image is at 4 times magnification. The white arrow indicates the silicon nitride window where a nanopore was drilled. Copper tape was used as an electrical connection to the gold electrode deposited on one of the silicon nitride chips [12]. Reprinted with permission from R. A. Lucas, C.-Y. Lin, L. A. Baker, and Z. S. Siwy, "Ionic amplifying circuits inspired by electronics and biology," *Nature Communications*, vol. 11, no. 1, Art. no. 1, Mar. 2020, doi: 10.1038/s41467-020-15398-3.

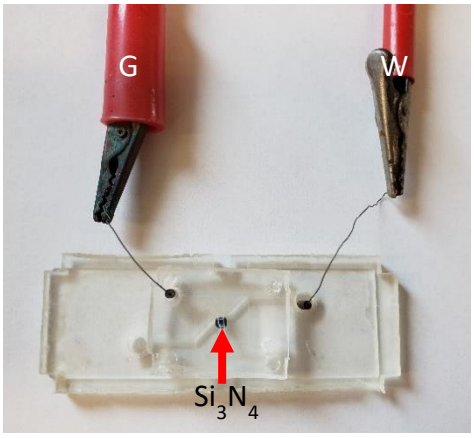

Figure 4.6: Image of generic conductivity cell setup. Ground and working electrodes are indicated by G and W respectively. The placement of the silicon nitride device is indicated by a red arrow.

Once device fabrication was complete, characterization began by placing the device in a conductivity cell with the same concentration of KCl at pH 8 placed on either side of the nanopore (Figure 4.6). Ag/AgCl pellet electrodes were placed in each of the reservoirs and a

Keithley 6487 picoammeter/voltage source was used for current-voltage measurements. A Keithley 2450 was used to supply voltage through the gate electrode at the base.

To ensure that chemical modification was successful, IV curves were recorded between the emitter and base with the collector electrode disconnected (Figure 4.7). Complete modification was confirmed with a flip in rectification post-silanization.

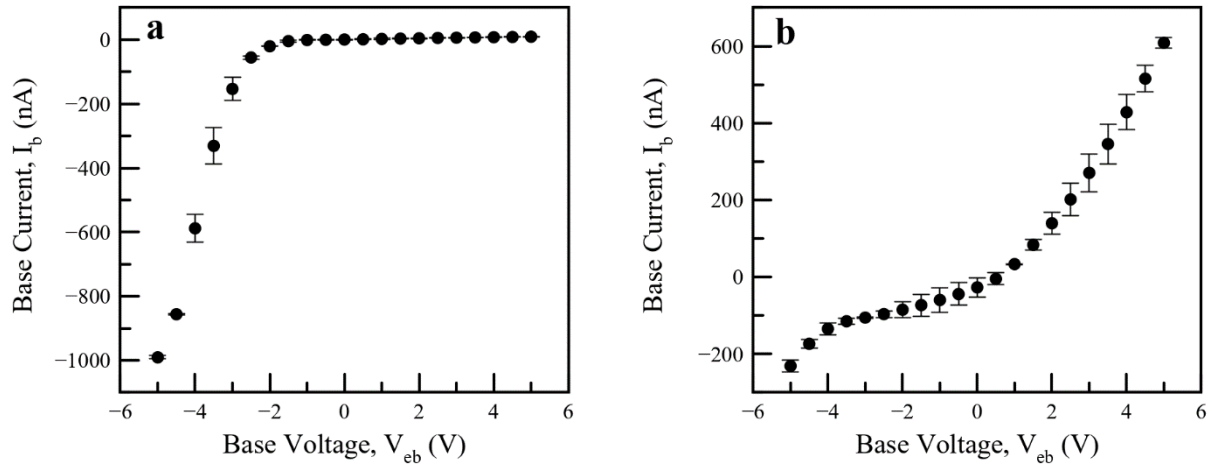

Figure 4.7: Recordings for a transistor with opening diameter of 600 nm in 10 mM KCl. Current-voltage curves with voltage applied between emitter-base junction with collector electrode disconnected. (a) Measurement with an as prepared device, i.e. pre-silanization; (b) Measurements after silanization, which rendered the silicon nitride surface and pore wall positively charged. Error bars were calculated as standard deviation from an average of at least two independent voltage scans [12]. Reprinted with permission from R. A. Lucas, C.-Y. Lin, L. A. Baker, and Z. S. Siwy, "Ionic amplifying circuits inspired by electronics and biology," *Nature Communications*, vol. 11, no. 1, Art. no. 1, Mar. 2020, doi: 10.1038/s41467-020-15398-3.

As the next step, we probed performance of the IBJT using two voltage signals, V_{ec}, and V_{eb}. Typical characteristic curves for pores made using both fabrication methods are shown in Figure 4.8 for 10 mM and 100 mM KCl for the larger and smaller device respectively. Using the three electrodes described, ion current output can be adjusted through change of base input voltage, V_{eb}. Recordings can be analyzed by plotting the collector current, I_c, at a single collector voltage V_{ec}, for each base voltage (Figure 4.8b,d). One of the first visible differences between the two devices is the base voltage span they

were responsive to. The 600 nm in diameter device required gate voltages at least 1V in absolute value. This device also required V_{ec} > 1V. The smaller transistor, 140 nm in diameter, was able to respond to base voltages as low as 0.2V with V_{ec} = 1V. Another difference between the devices is the salt concentration the devices were most responsive in. The smaller device could respond in larger concentrations and was thus measured in 100 mM KCl, while the larger device required 10-fold lower concentrations to see a response. Recordings confirm the need for lower concentrations in the larger device as only large V_{eb} of ±5V modulated output current in 100 mM KCl (Figure 4.9).

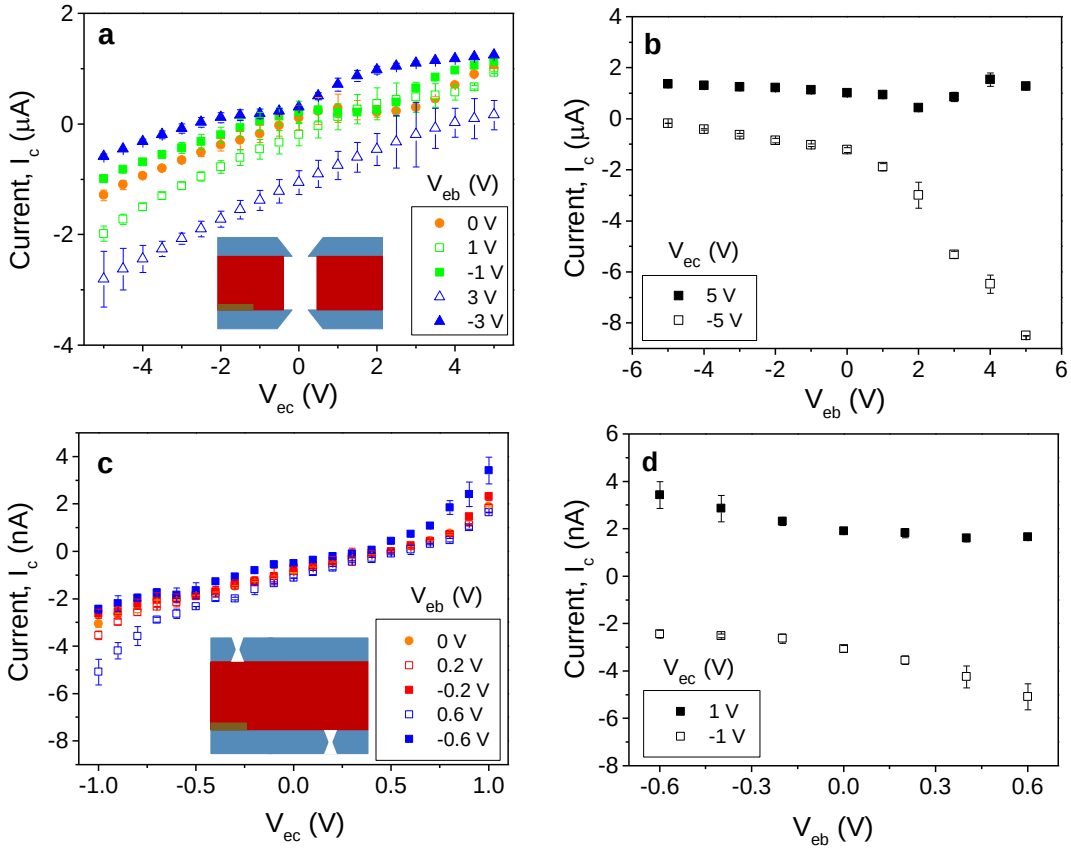

Figure 4.8: Characteristic curves of individual ionic transistors. (a-b) Recordings for a device with opening diameter of 600 nm in 10 mM KCl; (c-d) recordings for a device with an opening diameter of 140 nm in 100 mM KCl. (b) and (d) were created based on current-voltage curves in (a) and (c) and show I_c at chosen V_{ec} for

different gate inputs. Error bars were calculated as standard deviation from an average of at least two independent voltage scans [12]. Reprinted with permission from R. A. Lucas, C.-Y. Lin, L. A. Baker, and Z. S. Siwy, "Ionic amplifying circuits inspired by electronics and biology," *Nature Communications*, vol. 11, no. 1, Art. no. 1, Mar. 2020, doi: 10.1038/s41467-020-15398-3.

As is seen in the characteristic curves of the devices in Figure 4.8 the operation of the two npn structures depends on both polarity of gate voltage and polarity of V_{ec}.

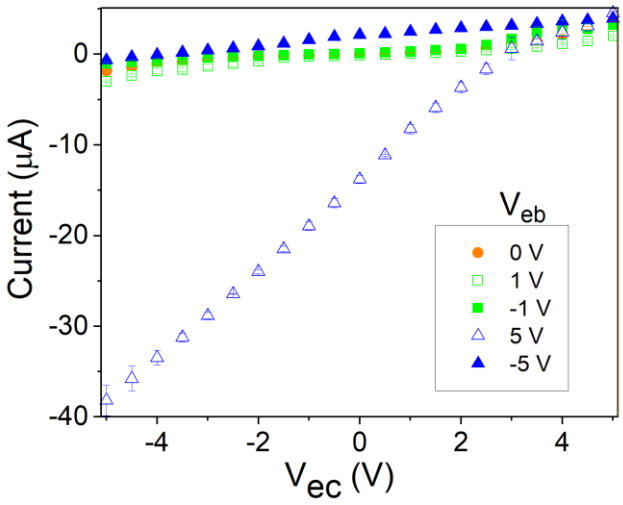

Figure 4.9: Experimental current-voltage curves with various base voltage inputs for a transistor with an opening diameter of 600 nm in 100 mM KCl [12]. Reprinted with permission from R. A. Lucas, C.-Y. Lin, L. A. Baker, and Z. S. Siwy, "Ionic amplifying circuits inspired by electronics and biology," *Nature Communications*, vol. 11, no. 1, Art. no. 1, Mar. 2020, doi: 10.1038/s41467-020-15398-3.

4.3 COMSOL Modeling for an Individual Ionic Transistor

In order to analyze the experimental results in more depth, modeling of ionic concentrations and currents was performed using COMSOL. Coupled Poisson-Nernst-Planck and Stokes-Brinkman equations were solved using finite element analysis, see Chapter 2.5 "The Poisson-Nernst-Planck-Stokes (PNPS) System" and Chapter 2.6 "COMSOL Multiphysics Modeling Using Finite Element Analysis". Using the Stokes-Brinkman equations, rather than Navier-Stokes and Poisson-Nernst-Planck alone, allows us to include the effect of additional friction that is present due to the presence of Nafion in the system. Specifically, there is an additional

term, $h\rho_{PE}$, added to the Poisson equation, and a term, $-h\gamma_{PE}\vec{u}$, added to the Navier-Stokes momentum equation. Here ρ_{PE} is the volume charge density of the polyelectrolyte, $\vec{u}$ is fluid velocity, γ_{PE} is the hydrodynamic frictional coefficient of the polyelectrolyte layer, and h is a coefficient which allows the presence ($h = 1$) of the Nafion layer in some regions and not in others ($h = 0$). Due to the two different fabrication methods, two different geometrical models were developed to represent the two transistor structures (Figure 4.10). In both cases the Nafion region was represented as a volume charge density.

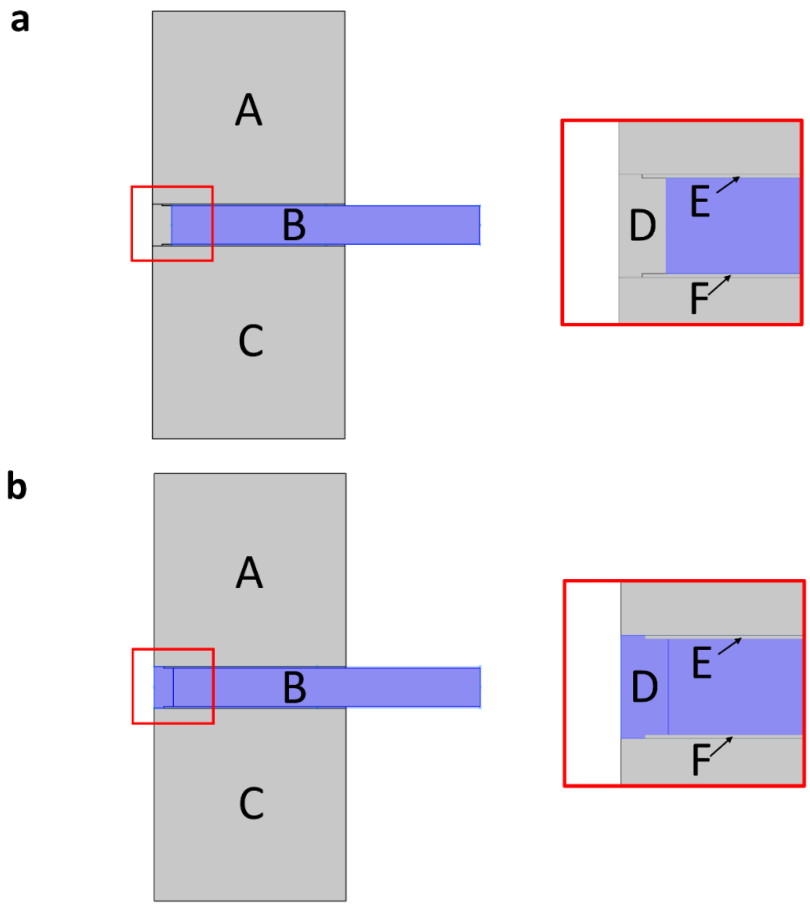

Figure 4.10: Model geometry used for predicting ion transport through a bipolar junction ionic transistor: the total thickness of the devices is 1 μm. Pore diameter is 500 nm for larger devices and 150 nm for smaller devices. (a) Scheme used for large devices and (b) small devices where purple shaded regions are representative of Nafion space charge. In (a) the Nafion region had a diameter twice as large as the silicon nitride pores [12]. Reprinted with permission from R. A. Lucas, C.-Y. Lin, L. A. Baker, and Z. S. Siwy, "Ionic amplifying circuits inspired by electronics and biology," *Nature Communications*, vol. 11, no. 1, Art. no. 1, Mar. 2020, doi: 10.1038/s41467-020-15398-3.

For the larger device a pore diameter of 500 nm was modeled. The smaller device contained pores with 150 nm diameter. Concentrations used for modeling were the same as those used for experiments. Assumed boundary conditions were as follows: (1) Ionic concentration in the reservoirs essentially reaches the bulk concentration value. (2) The membrane surface is ion-impenetrable and non-slip. (3) Potential biases are applied to the edges of regions C and B (regions as shown in Figure 4.10) while the far-side of region A is grounded so that the ends of C and B correspond to the collector and base respectively while the end of region A corresponds to the emitter. (4) Region B is modeled with a space charge of $1.5 \cdot 10^5$ C/m^3. This value was chosen based on previous work with polyelectrolytes [63], [64] and reduced by a factor of 100 to achieve convergence of the system. (5) The silicon nitride surfaces of regions E and F are given a surface charge density of +0.04 C/m^2 for the silanized device, a value that is close to the magnitude of surface charge of as prepared silicon nitride nanopores [65].

For a solid-state npn transistor we would expect that with $V_{ec} < 0$ and a positively biased gate the device should be in saturation mode with both junctions in the on-state. This is clearly observed for our ionic device, as shown by modeling through ionic concentrations greater than the bulk values at both junction positions (Figure 4.11a,d). In this mode of operation, ionic concentrations increase with increase of the gate signal and the highest currents are produced in this configuration. With application of negative base voltages and positive transmembrane potential a solid-state transistor is in what is called cut-off mode with no current flowing. It is seen for this configuration of the ionic device, depletion zones are indeed created at both junctions (Figure 4.11b,e). However, in both experiments and modeling the current does not become negligible in this mode of operation. The finite amount of current being conducted likely stems from multiple sources one of which is the

thickness of the silicon nitride films which is only tens of nanometers thick. It has been shown that when a short zone with surface charge of one polarity is connected to a longer ion selective region with opposite charge polarity, the diode junction is only able to create an off-state at small voltages [66]. Larger voltages cause the depletion zone to extend outside the nanopore causing breakdown. Another contributing factor is the, relatively, larger pore diameter of at least 100 nm which does not allow complete formation of a depletion zone so that some ionic current may still be conducted. Finally, in the case that $V_{ec} > 0$ and $V_{eb} > 0$, the npn device should be in the active mode where only one of the diode junctions is in the on-state (Figure 4.11a,d). The ionic concentrations confirm the predictions and show one region with ionic enhancement at a position of ~1040 nm and one region of ionic depletion located at ~40 nm (Figure 4.11a,d). If V_{eb} and V_{ec} are both negative the device works in reverse active mode, which along with active mode can produce amplification. In reverse active mode the emitter-base junction is a depletion zone rather than the collector-base junction as in active mode (Figure 4.11b,e).

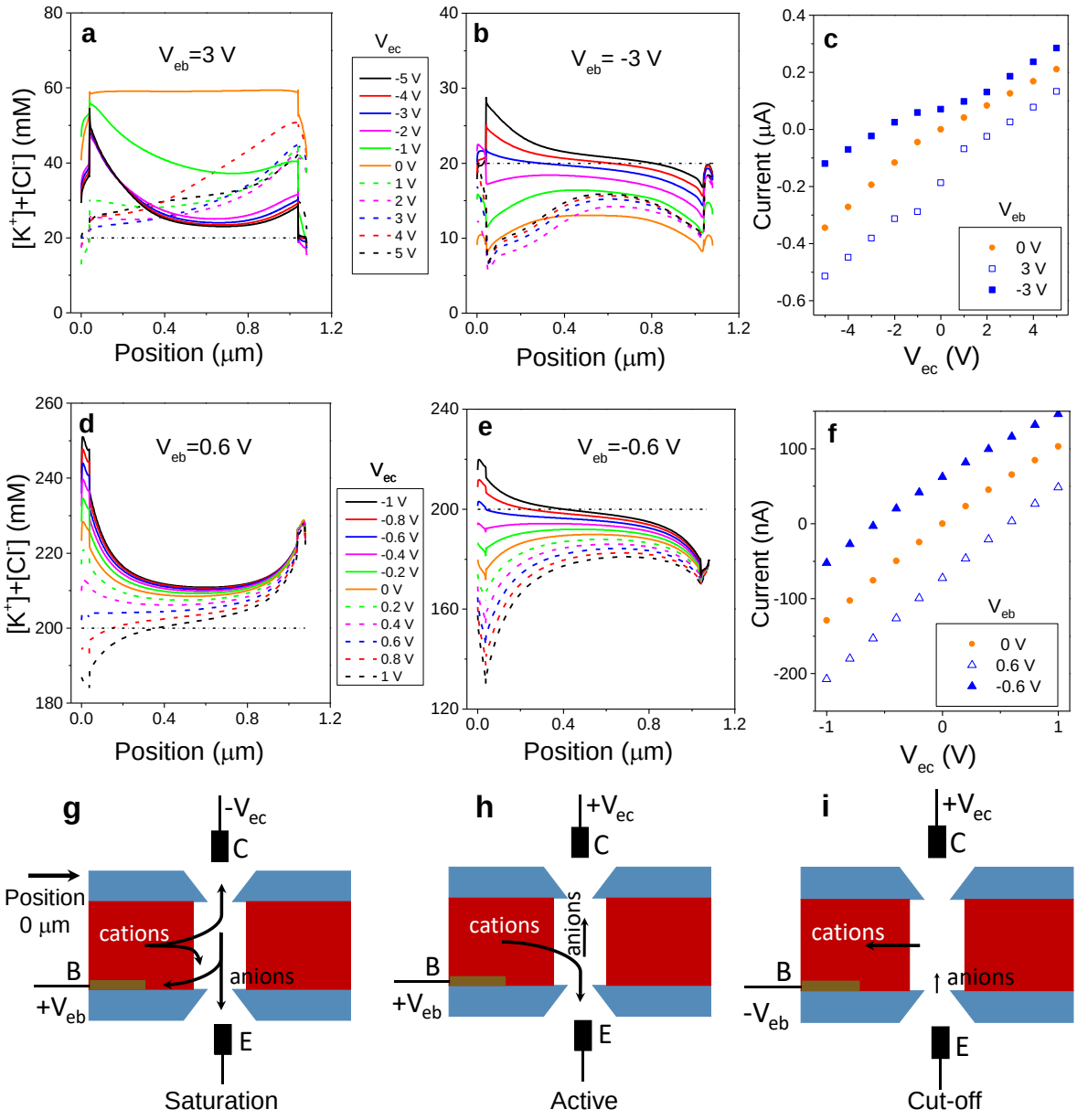

Figure 4.11: (a-c) Analysis of a device with a 500nm in diameter pore in 10mM KCl, pH 8. Concentration profiles along the pore axis for (a) V_{eb} =3V, and (b) V_{eb} =−3 V, and V_{ec} varied as shown in the legend. (c) Current-voltage curves predicted from the model for V_{eb} =±3V. (d–f) Analysis of a device with 150nm in diameter pores in 100mM KCl, pH 8. Concentration profiles along the pore axis for (d) V_{eb} =0.6V and (e) V_{eb} =−0.6V, and V_{ec} varied as shown in the legend. (f) Current-voltage curves predicted from the model for V_{eb} =±0.6V. All concentrations shown are cross-section averaged. A dashed-dotted line in a, b, d, and e indicates bulk concentration of ions. The collector is placed at the position 0μm. Note that the pores in the two transistors modeled were assumed to be aligned to assure axial symmetry of the system. (g–i) Schemes of saturation (g), active (h), and cutoff (i) modes of operation of an ionic transistor [12]. Reprinted with permission from R. A. Lucas, C.-Y. Lin, L. A. Baker, and Z. S. Siwy, "Ionic amplifying circuits inspired by electronics and biology," Nature Communications, vol. 11, no. 1, Art. no. 1, Mar. 2020, doi: 10.1038/s41467-020-15398-3.

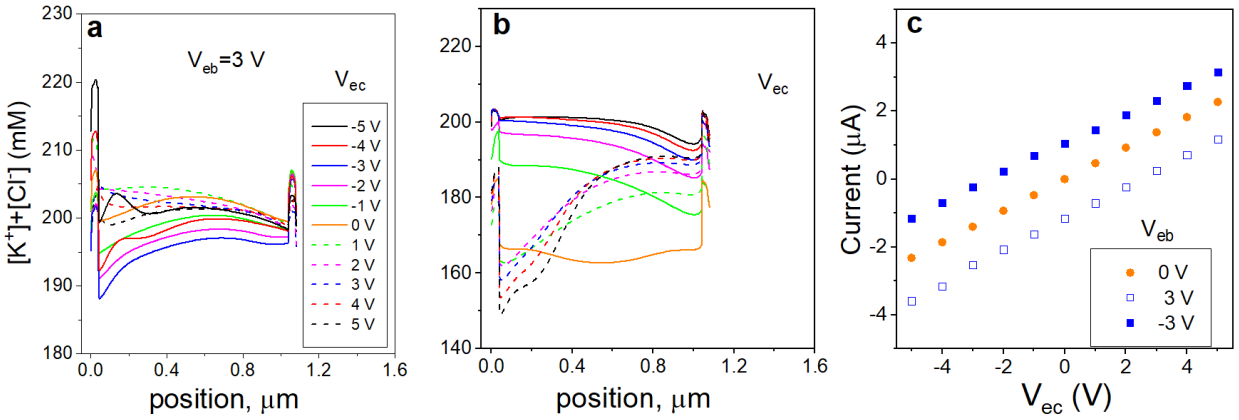

Figure 4.12: (a-c) Results of numerical modeling for a transistor based on 500 nm in diameter pores in 100 mM KCl. These panels should be compared with Figure 4.11a-c, which show modeling for the same device in 10 mM KCl [12]. Reprinted with permission from R. A. Lucas, C.-Y. Lin, L. A. Baker, and Z. S. Siwy, "Ionic amplifying circuits inspired by electronics and biology," *Nature Communications*, vol. 11, no. 1, Art. no. 1, Mar. 2020, doi: 10.1038/s41467-020-15398-3.

This modeling along with experimental results confirms that ionic transistors up to several hundreds of nanometers in diameter were functional and responsive to input base voltages. This is evidenced through the voltage-modulated currents through the pores. However, it was confirmed through modeling of the larger device in 100 mM KCl that influence on ionic concentrations declined when the device was in contact with this higher concentration solution (Figure 4.12). The transistor, in this higher concentration could not display saturation mode, so that ionic concentrations in the saturation mode voltage region stayed at values close to bulk concentration.

Thus, modeling in proper ionic strength solutions of ionic concentrations in both large and small devices revealed they could establish the four modes of operation of a bipolar junction transistor. However, for the 150 nm in diameter device the magnitude of I_c which resulted from modeling was much larger than what was measured. It was hypothesized that this discrepancy could possibly result from the fact that for the smaller device the two chips

with nanopores were not directly aligned. To test this theory a 3-dimensional numerical model was built to calculate ion current with pores that were offset by either 500 or 750 nm (Figure 4.13).

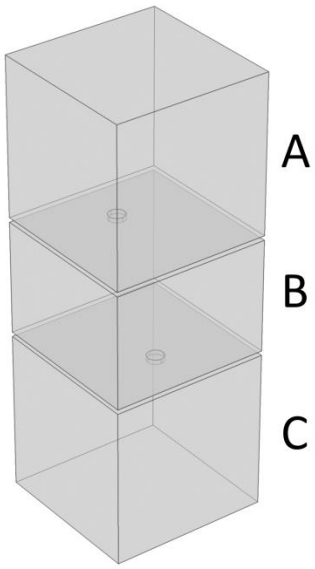

Figure 4.13: Geometry of a model used for predicting ion transport through a bipolar junction ionic transistor: the pores in silicon nitride are 40 nm in length each, and their diameter is 150 nm. Similar boundary conditions are used as for the axisymmetric model. Regions A and C are representative of electrolyte reservoirs while region B contains the Nafion membrane as a space charge. In the model shown the pores are offset by 500 nm [12]. Reprinted with permission from R. A. Lucas, C.-Y. Lin, L. A. Baker, and Z. S. Siwy, "Ionic amplifying circuits inspired by electronics and biology," *Nature Communications*, vol. 11, no. 1, Art. no. 1, Mar. 2020, doi: 10.1038/s41467-020-15398-3.

In Figure 4.14 it can be seen that current was independent of nanopore offset suggesting that the lack of nanopore alignment did not cause the discrepancy between measured and modeled current values. Another possibility for the small currents seen experimentally is the influence of the Nafion membrane on the distribution of the electric field within the device. For this small ionic transistor, the pore does not continue through the Nafion meaning that the fluxes of cations and anions are separated more fully to opposite sides of the membrane [67]. Previous publications show the presence of this setup induces a concentration

polarization and formation of a dynamic depletion zone with local inhomogeneous ionic concentration [68]. The additional resistance of this depletion zone could be responsible for the reduced collector current which is measured. Including the possible destabilization of the depletion zone by local vortices was outside the range of this work.

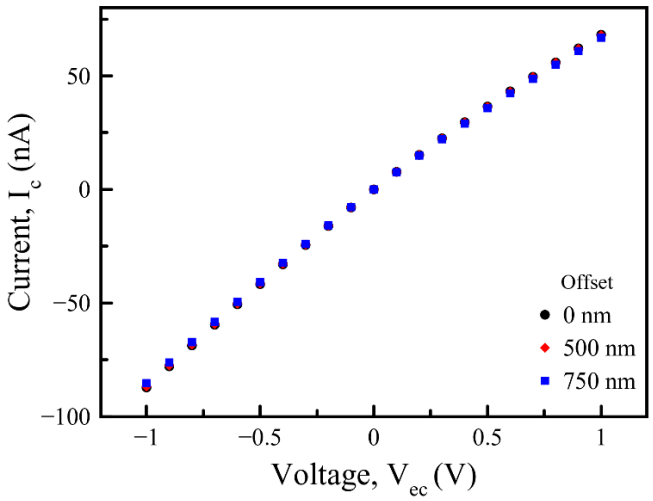

Figure 4.14: Collector current-voltage results from a 3-dimensional model. Curves shown for pores at various offset distances where 0 nm corresponds to the case when the pores are aligned [12]. Reprinted with permission from R. A. Lucas, C.-Y. Lin, L. A. Baker, and Z. S. Siwy, "Ionic amplifying circuits inspired by electronics and biology," *Nature Communications*, vol. 11, no. 1, Art. no. 1, Mar. 2020, doi: 10.1038/s41467-020-15398-3.

4.4 Ionic Current Amplification for a Single NPN Device

In order to characterize current amplification, the base input signal was changed from voltage to current, I_b. Figure 4.15a,c shows collector current as a function of base current for chosen values of V_{ec}. Data for two devices are shown: (i) 540 nm in diameter device with measurements performed in 1 mM KCl, and (ii) 140 nm diameter device with measurements performed in 100 mM KCl. For the larger device a lower ionic strength was required in order to observe the amplification effect. In Figure 4.15b,d the amplifications for both devices are

shown with current gain calculated as $\beta = \frac{I_c}{I_b}$. Here I_c is the recorded output current through the device, and I_b is the current input into the base region. Because amplification occurs in the active mode of solid-state bipolar junction transistors, all calculations were performed only for the active mode. Thus, amplification of the 540 nm transistor was calculated at V_{ec} = +5V and positive I_b and for V_{ec} = -5V and negative I_b. For the 140 nm in diameter transistor gain values were computed at V_{ec} = 1V and V_{ec} = -1V. In order to report only significant values, only those for which the difference $(I_c\ (I_b) - I_c(I_b = 0))$ was larger than the average error of measuring I_c are shown. The smallest current measured for the 540 nm device was 70 nA with a gain of ~6. With similar gain values, the 140 nm device detected currents 70-times smaller at ~1 nA in 100-times higher ionic strength solution.

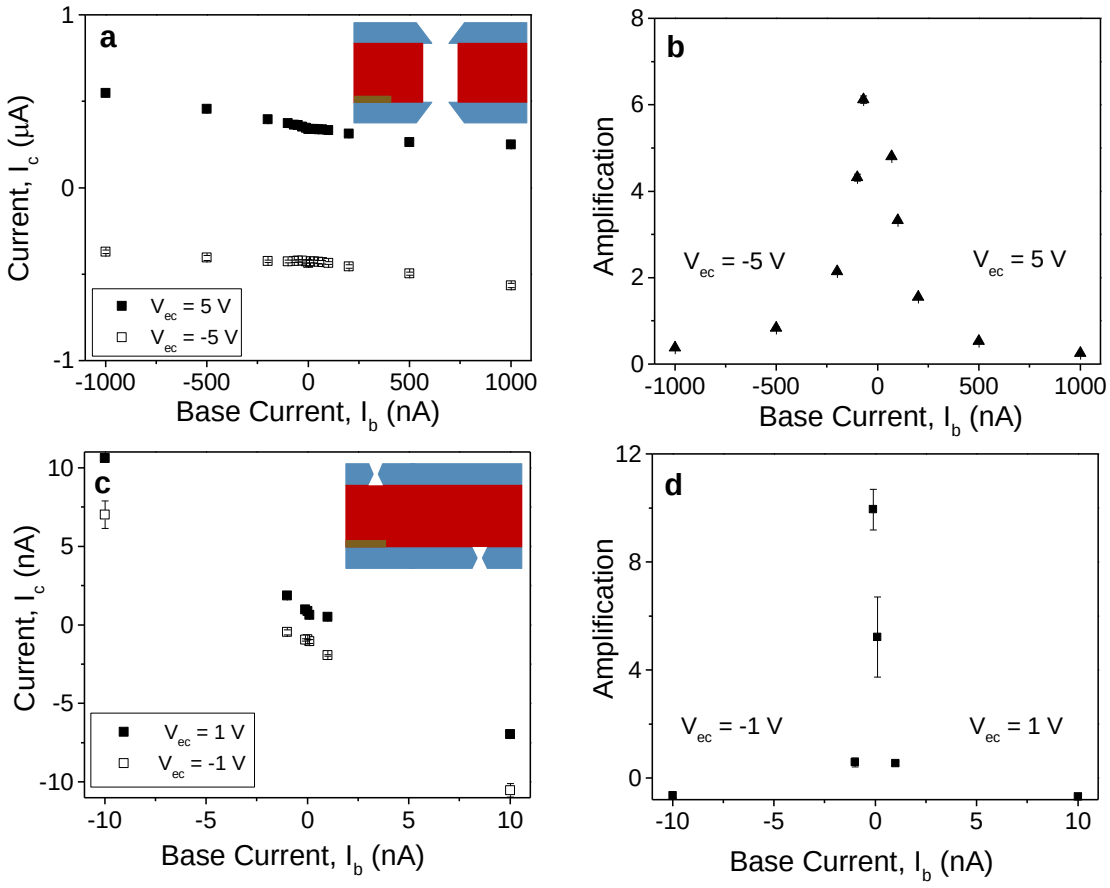

Figure 4.15: (a-b) Measurements for an ionic transistor with an opening diameter of 540 nm in 1 mM KCl. (a) Current, I_c, at a collector voltage of either V_{ec} = -5 V or V_{ec} = 5 V as a function of base current, I_b. (b) Current gain calculated as a function of base current. Values calculated for V_{ec} = -5 V at negative base currents, and V_{ec} = 5 V at positive base currents correspond to the active mode of the device. (c-d) Measurements for an ionic transistor with an opening of 140 nm in 100 mM KCl. (c) Current, I_c, at collector voltages of -1 V and +1 V as a function of base current together with current gain shown in (d) calculated at V_{ec} = ±1V. Error bars calculated as standard deviation from an average of values in at least two voltage scans [12]. Reprinted with permission from R. A. Lucas, C.-Y. Lin, L. A. Baker, and Z. S. Siwy, "Ionic amplifying circuits inspired by electronics and biology," *Nature Communications*, vol. 11, no. 1, Art. no. 1, Mar. 2020, doi: 10.1038/s41467-020-15398-3.

We would like to note that the ionic transistors are able to amplify only small ionic signals; with the increase of I_b, the gains of the two transistors decreased. We believe that this effect is caused by high ionic concentrations in the region of the pore which is connected to Nafion (the gate region) leading to an ionic connection between the collector, emitter, and base zones. This leads to the collector current, I_c, being affected by the combination of

voltages V_{eb} and V_{ec}. When I_b is low, the gate signal will amplify the ionic flow between emitter and collector, similar to a solid-state transistor. As I_b increases, connectivity between the three charge regions of the transistor increases the current between emitter and gate leading to a smaller collector current, I_c, and thus lower amplification. Therefore, the ionic transistors are indeed most powerful in amplifying small gate signals as is displayed in Figure 4.15b,d.

Upon increasing V_{ec} from V_{ec} = 1V to a value of V_{ec} = 3V for the ionic transistors with smaller pore diameters, substantially larger amplifications are achieved. Figure 4.16 shows a transistor with 155 nm diameter pores that at V_{ec} = 3V provided an amplification of ~300

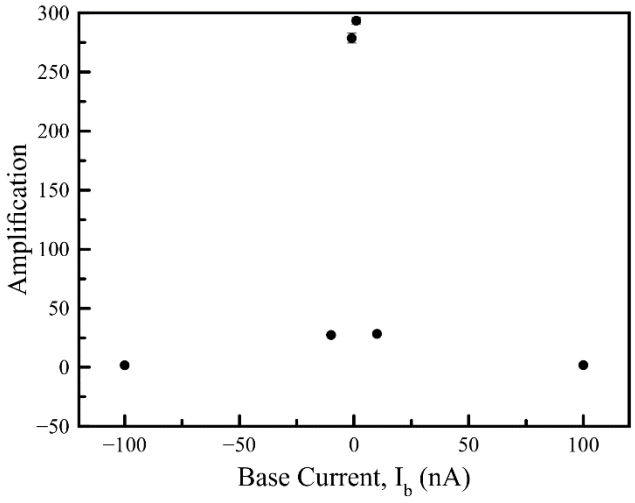

Figure 4.16: Measurements done for a transistor with an opening diameter of 155 nm in 100 mM KCl. Values calculated for V_{ec} = -3 V at negative base currents, and V_{ec} = 3 V at positive base currents, corresponding to the active modes of the device. Error bars were calculated as standard deviation from an average of values in at least two voltage scans [12]. Reprinted with permission from R. A. Lucas, C.-Y. Lin, L. A. Baker, and Z. S. Siwy, "Ionic amplifying circuits inspired by electronics and biology," *Nature Communications*, vol. 11, no. 1, Art. no. 1, Mar. 2020, doi: 10.1038/s41467-020-15398-3.

for a 1 nA input current.

4.5 Creation of an Ionic Darlington Amplifier

In order to achieve higher amplifications than those offered by individual transistors, a Darlington amplifier circuit setup was prepared. This circuit is composed of two transistors which are connected to one other so that the amplified output of the first transistor becomes the input signal of the second one, to again be amplified (Figure 4.17a,b). In solid-state transistors this arrangement can produce amplifications up to the gains of the individual devices multiplied plus each individual gain.

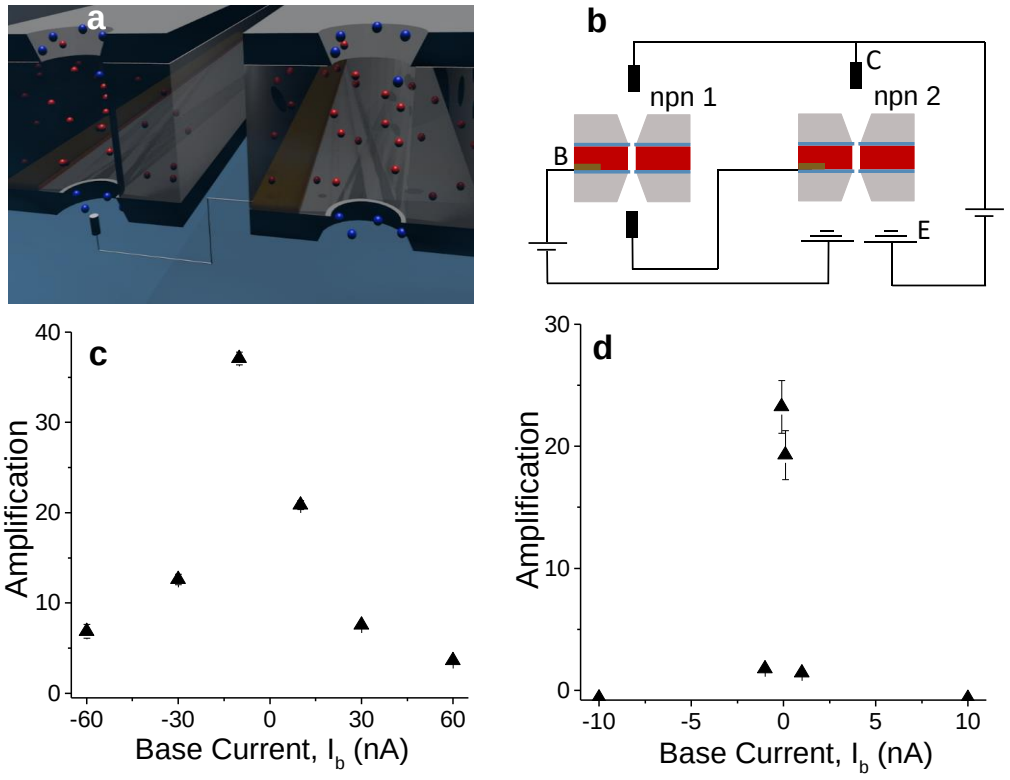

Figure 4.17: (a,b) Darlington amplifier circuit scheme and setup, respectively. (c) Current gain as a function of base current, I_b, for two bipolar transistors connected in a Darlington amplifier circuit in 1 mM KCl. Devices had pore sizes of 540 nm and 520 nm. (d) Current gain for a Darlington circuit composed of two bipolar transistors that contained pores with diameter of 140 nm and 150 nm; measurements were taken in 100 mM KCl. Error bars calculated as standard deviation from an average of values in at least two voltage scans [12]. Reprinted with permission from R. A. Lucas, C.-Y. Lin, L. A. Baker, and Z. S. Siwy, "Ionic amplifying circuits inspired by electronics and biology," *Nature Communications*, vol. 11, no. 1, Art. no. 1, Mar. 2020, doi: 10.1038/s41467-020-15398-3.

Characterization of two Darlington circuits composed of larger pores and smaller pores is shown in Figure 4.17. For the first Darlington pair, devices with 540 nm and 520 nm

opening diameter were used. This setup amplified ion current with gains up to 40 (Figure 4.17c), over 6 times higher than amplification values for an individual transistor. The higher gain of the Darlington setup allows for lower input currents, I_b, to be probed. Therefore, the same span of base voltages generates higher amplifications with smaller input currents in this setup than for a single ionic transistor alone.

Figure 4.17d exhibits amplifications of two individually prepared IBJT with opening diameters of ~150 nm. This circuit was tested in 100 mM KCl and produced a gain of 25, three times higher than the gain offered by one of the npn devices. The Darlington setup with these devices was able to detect a current of 0.1 nA, 10-fold lower than what was detectable by a single transistor alone.

While taking measurements it was noted that the overall gain offered by the Darlington amplifier is dependent on the position of the transistor that when probed individually produced a higher gain. Data shown in Figure 4.17 were obtained for the circuits where the device with the lower amplification was placed as npn 1 in the circuit setup as shown in Figure 4.17b. If positions of the two transistors in both Darlington pairs were switched, smaller overall gains were obtained, 7 and 15, for the ~520 nm and ~150 nm transistors, respectively (see Figure 4.18). Investigation of this effect is left to future experiments.

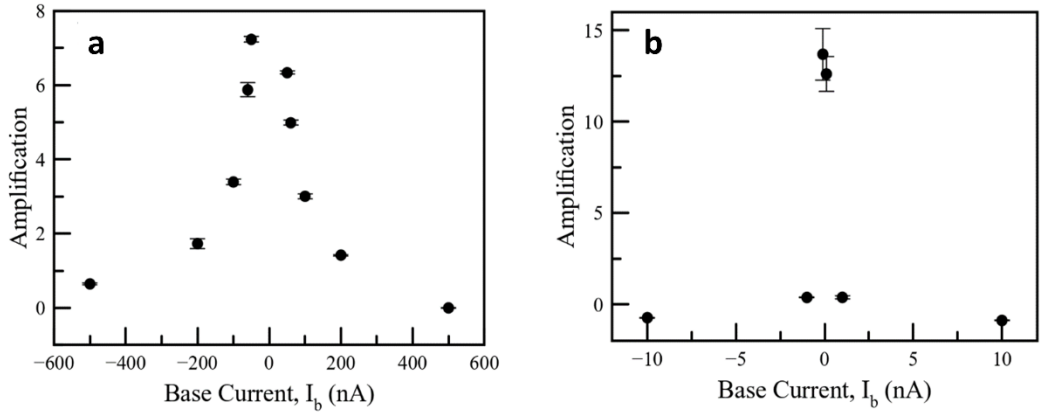

Figure 4.18: (a) Amplification values for the Darlington setup such that the 520 nm in diameter device provides the input for the 540 nm device. (b) Amplification for the Darlington setup such that a transistor with 150 nm pores provides input for the transistor with 140 nm in diameter pores. Error bars for both plots were calculated as standard deviation from an average of values in at least two voltage scans [12]. Reprinted with permission from R. A. Lucas, C.-Y. Lin, L. A. Baker, and Z. S. Siwy, "Ionic amplifying circuits inspired by electronics and biology," *Nature Communications*, vol. 11, no. 1, Art. no. 1, Mar. 2020, doi: 10.1038/s41467-020-15398-3.

We successfully demonstrated nanofluidic ionic bipolar junction transistors with fully ionic inputs and outputs. It was shown these components can be easily rearranged into amplifying units. Having taken inspiration from electronic amplifiers, the Darlington setup is just one of many possibilities for these ionic devices. Future work will increase selectivity of the device as well as decrease device size in order to detect current levels as low as fA. The equivalent of a pnp transistor will be created and with this addition a differential amplifier will be assembled. The type of ionic amplification displayed could be utilized in preparation of artificial biocircuits. One of the most classic examples in biology is the ion transport that exists within the synaptic cleft, where specific signaling molecules are released from the presynaptic terminal, travel across the confined space in the synaptic cleft, and are collected by receptors on the postsynaptic terminal. Solid-state systems are not currently capable of reaching this leveling of complexity, however, we can use layered designs to construct crude devices, inspired by this example. In the system studied here, the devices are selective mainly

to charge polarity. However, biological channels can differentiate between ions of the same charge, such as potassium and sodium. Taking inspiration from biology, it could be possible to impart chemical species selectivity as has been shown in the past with crown-ether functionalization [69]. These types of ion selective channels would allow a specific response of amplifying circuits to particular ionic species. These initial steps provide an example of how models of controlled ion transport can be combined with inspiration from electronic devices to realize new concepts of amplification or control of ionic transport switching in ionic systems.

CHAPTER 5

Tunability of Nanopore Arrays

Recently, ionic circuits have become of more interest [12], [52], [55], [56], [70]–[72]. Similar to integrated circuits in electronics, complex ionic circuits were predicted to exhibit functionalities that are impossible to achieve with individual devices. Complex ionic circuits with multiple devices have achieved logic gate functionalities [52]–[54], [56], voltage multiplication [71], current amplification [12], and half- and full-wave rectifiers [55]. However, creation of the majority of these circuits requires integration of multiple individual devices that leads to difficult to manufacture systems. Many require external connection of individual devices through electronic pathways [12], [71] or multiple ionic baths [55]. A new possibility explored in this chapter would allow for a design of ionic circuits all within a single membrane and with component resolutions down to those which exist for current nanofabrication techniques. This device creation relies on interactions between adjacent nanopores as well as the use of external signaling mechanisms to exert some control over these interactions. In designing the arrays with interacting nanopores, we were inspired by a cell membrane that also contains multiple channels and pores. In biology, new functionalities can indeed be created when different channels function together creating a responsive and adaptive ionic circuit. As a particular example, within an axon, two different types of voltage-gated channels enable transduction of nerve signals through space and time [73].

To investigate interactions between nanopores within the same membrane and identify mechanisms to control transport through all nanopores or only a subset of the pores, we

modeled behavior of cylindrical nanopore arrays composed of 3, 6, or 9 nanopores. There is a multitude of different external signals that could be used to exert control over nanopore interactions. The signals include electrolyte pH and concentration, potential differences applied across the membrane and locally, presence of different types of ions or molecules that can modulate ionic transport through nanopores, as well as inclusion of nanopores with non-linear current-voltage behaviors. In this analysis, we investigate the effects of varying concentration of the bulk electrolyte, surface charge of the pore walls, and potential differences applied to the system. Experimentally, the introduction of an electrode system and simple changing of the potential bias is one of the easiest ways to control transport properties of a nanopore array. We examine ion current through individual nanopores in an array and identify conditions when the transport of the nanopore array depends on the number and position of neighboring pores as well as variation of the external signals discussed above. For example, we see that applying local potential on one side of the membrane to a gate electrode results in different transport properties of nanopores within the array, even though the nanopores have the same electrochemical properties. Specifically, within one array some nanopores will rectify current such that positive currents are higher than negative currents, while the remaining pores will rectify in the opposite direction. We also provide understanding of how the inclusion of nanopores with diode-like behavior influences ionic transport of other nanopores in the array.

Applications of these nanopore arrays could include building ionic circuits which can transduce signals through space and time, potentially mimicking the behavior of an axon. Another application could be realization of amplified chemical sensing with controlled delivery of ions or molecules to specific locations within the array and mimicking the

amplified and specific response of biological signaling cascades. Nanopore arrays could also become the basis for complex logic gates.

5.1 Nanopore Array Theory and Background

Exploration of the nanopore array systems begun with the analysis of a 9-pore array with voltage applied across it, V_m. The array is composed of a square of 3 by 3 nanopores all 5 nm in diameter and 40 nm in length (Figure 5.1). The system was modeled numerically using the Poisson-Nernst-Planck equations, as shown below:

$$-\varepsilon_f \nabla^2 \varphi = \sum_{i=1}^{2} F z_i c_i \tag{5.1}$$

$$\nabla \cdot \boldsymbol{J}_i = \nabla \cdot \left[\boldsymbol{u} c_i - D_i \nabla c_i - \frac{z_i F}{RT} D_i c_i \nabla \varphi \right] = 0 \tag{5.2}$$

where φ is electric potential, $\boldsymbol{u}$ is fluid velocity, $\boldsymbol{J}_i$ is flux of the ith ionic species, c_i is concentration of the ith ionic species, D_i is diffusivity of the ith ionic species, z_i is valence of the ith ionic species, ε_f is fluid permittivity, F is Faraday's constant, R is the gas constant, and T is absolute temperature. Boundary conditions are as follows: (i) ionic concentration in the reservoirs essentially reaches bulk concentration, (ii) the membrane surface is ion-impenetrable and non-slip, and (iii) potential bias is applied to the bottom surface of the lower reservoir. The top surface of the upper reservoir is grounded. Ionic current was calculated as $\int_{\Pi} (\sum_{i=1}^{2} F z_i \boldsymbol{J}_i) \cdot \boldsymbol{n} d\Pi$ where Π represents volume of the domain where current is wished to be calculated.

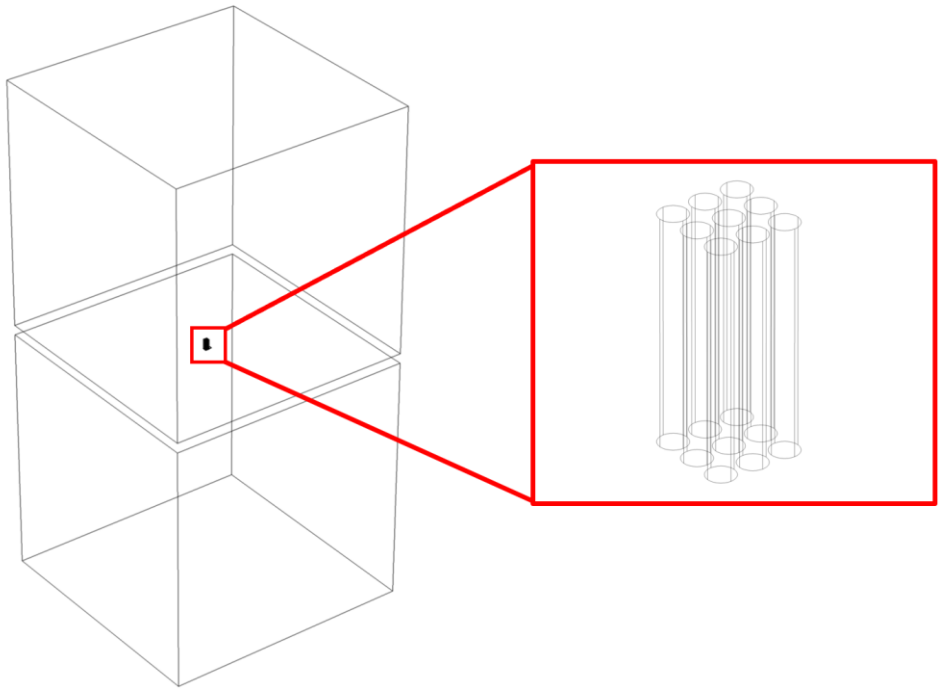

Figure 5.1. Simulation geometry. A COMSOL model used for predicting ionic transport through an array of 9 nanopores. The reservoirs were 1 μm long and 1 μm wide. (left) Entire model geometry. (right) Magnified view of 9-pore array [4]. Adapted with permission from R. A. Lucas and Z. S. Siwy, "Tunable Nanopore Arrays as the Basis for Ionic Circuits," *ACS Appl. Mater. Interfaces*, vol. 12, no. 50, pp. 56622–56631, Dec. 2020, doi: 10.1021/acsami.0c18574. Copyright 2020 American Chemical Society.

It is known from previous reports on nanopore arrays as well as nanoelectrode arrays that the distance between these nanoscale objects determines whether the behavior of one nanopore affects the behavior of another neighboring pore [74]–[77]. Therefore, the first parameter that we investigated was center-to-center distance between nanopores in the array (Figure 5.2). The walls of these pores were charged, thus applying external voltage led to the concentration polarization effect. This effect occurs in nanopores due to their selective nature. With a Debye length similar to the radius of the pore, the nanopore will be filled mainly with counterions. Therefore, when a potential is applied across the pore, ions of only one charge type can pass and thus one entrance of the pore will be in contact with a region

depleted of ions, while the other one will be in contact with a region containing a higher concentration of ions than in the bulk. This is known as concentration polarization. Based on previous reports [76], [77], we hypothesized that the interconnection of nanopores would be highly dependent on spacing. We predicted that nanopores within an array would influence each other's transport properties when the depletion/enhancement zones of neighboring pores start overlapping.

We considered the 9-nanopore arrays with a distance between pores that varied between 6 nm and 100 nm. Figure 5.2c,d shows current-voltage curves through whole arrays in 100 mM KCl. The results suggest that with a distance between pores of less than 100 nm, the nanopores do not conduct current independently, as evidenced by a reduction in overall current through the array compared with what is expected based on the conductance of a single, isolated nanopore. This finding agrees with what has been seen previously for arrays where diffusion at the individual pores was only found to be independent from one another at distances 56 times the pore radius [77]. Current-voltage curves shown in Figure 5.2c,d also reveal plateauing of current at higher transmembrane potentials. The effect of current saturation for higher voltages stems from concentration polarization and formation of the depletion zone at one pore entrance [78]. Concentration polarization was further confirmed by modeling of current-voltage curves through arrays that contained nanopores with two charge densities of the pore walls. Figure 5.2c shows results for nanopores that carry a surface charge density of -0.05 C/m^2, while Figure 5.2d shows results for -0.1 C/m^2. The ion current plateauing occurs at lower voltages for the array with a higher surface charge compared to the array with less charged pores, supporting our hypothesis on the influence of concentration polarization on ionic transport of the nanopore arrays.

The formation of a depletion zone at one pore entrance can also be analyzed through the ion concentration profiles shown in Figure 5.2e,f. Depletion zones form around the pore mouths in contact with the electrode biased at +1V, thus at the side of the membrane from where cations are sourced. As the distance between pores is decreased, the depletion zones of the neighboring pores start overlapping, as seen in Figure 5.2f. As mentioned previously, it is when these zones overlap that the array current is dependent on the distance between pores. This property was utilized to create ionic circuits which are responsive to external stimuli.

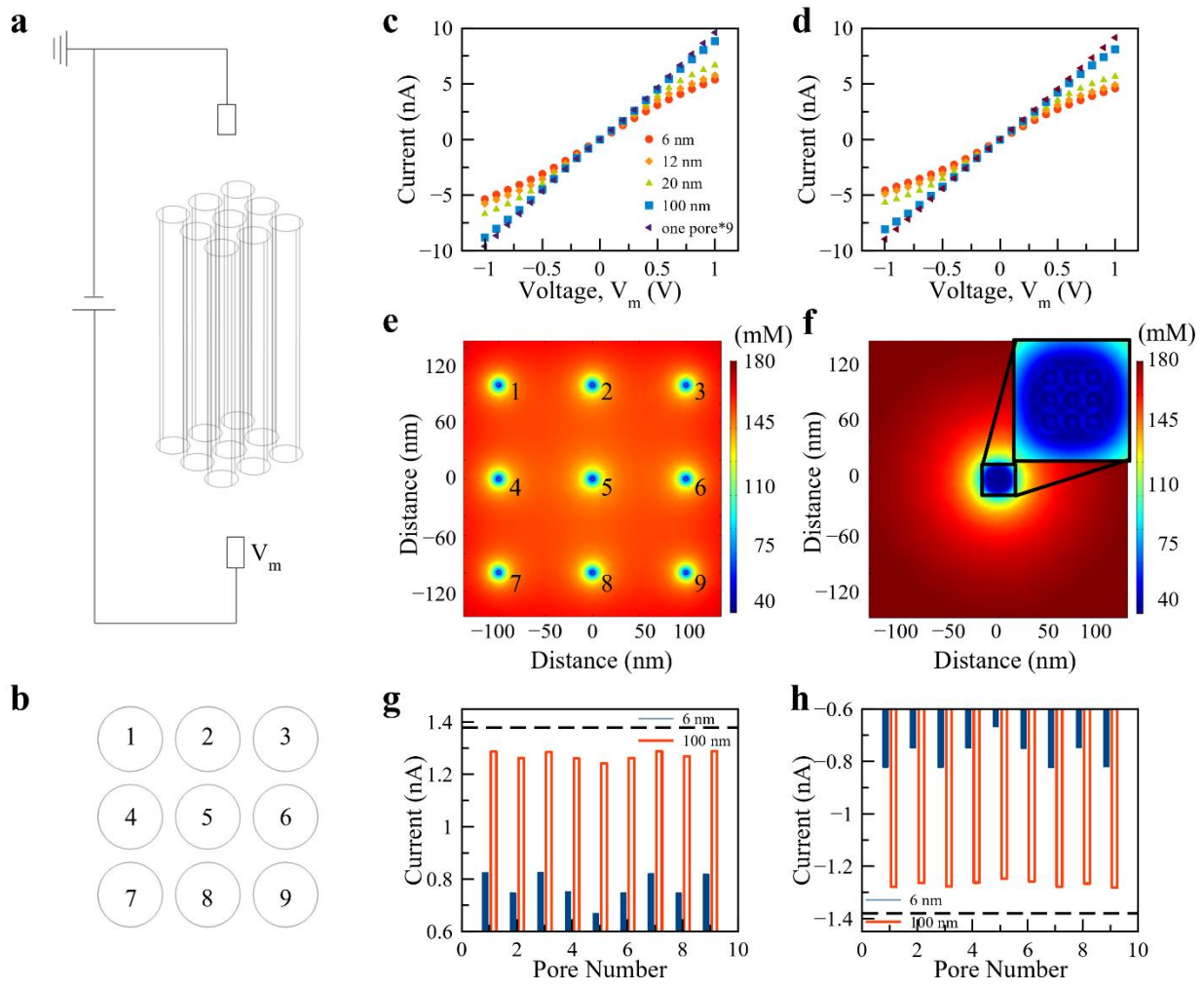

Figure 5.2: Modeling of a nanopore array consisting of 9 pores. The pores were 5 nm in diameter and 40 nm in length; simulations were performed in 100 mM bulk KCl solution. (a) Schematic of nanopore array system showing electrode placement where V_m provides the potential difference across the membrane. (b) Cross-

sectional view of the array with assigned pore numbers. (c) Current-voltage curves for 9-pore arrays with varying center-to-center pore distance. Surface charge density of the pore walls is -0.05 C/m^2. (d) Same as (c) with a pore surface charge density of -0.1. C/m^2. (e) (f) 2D profiles of total ionic concentrations when the distance between pores is 100 nm and 6 nm, respectively; surface charge density of -0.05 C/m^2 was used in the simulations. Concentrations at the surface in contact with a positively biased (working) electrode at V_m = 1 V are shown. (g) Current through each individual pore in the array for two different center-to-center pore distances at the transmembrane potential, V_m =1 V, and with a surface charge density of -0.05 C/m^2. The dashed line represents the current through a single isolated pore. (h) Same as (g) at V_m =- 1 V [4]. Reprinted with permission from R. A. Lucas and Z. S. Siwy, "Tunable Nanopore Arrays as the Basis for Ionic Circuits," *ACS Appl. Mater. Interfaces*, vol. 12, no. 50, pp. 56622–56631, Dec. 2020, doi: 10.1021/acsami.0c18574. Copyright 2020 American Chemical Society.

After examining the ion current through the whole array, the next step was to understand the properties of ionic transport through individual pores of the array. The values of ion current through each pore of the 9-pore array are shown in Figure 5.2g,h for two different distances between pores: 6 nm and 100 nm. Each pore is numbered by its position in the array as shown in Figure 5.2b. Our modeling results revealed that the corner pores, with the lowest number of neighbors, had the highest current, while the center pore, in position 5, with the greatest number of neighbors, had the lowest current. The dependence of ion current of nanopores in an array on the number of neighboring pores agrees with what we have seen where more overlapping depletion zones will produce a lower current. Conceptually, the results are also in agreement with our intuition that the more pores nearby competing for the same resources (ions) the lower the current will be. We also performed a control simulation of a nanopore array containing uncharged nanopores, where the pores can interact only through overlapping access resistances and diffusion zones (Figure 5.3). In this array, only a weak dependence of ion current through individual pores on the number of neighbors was found, confirming that the main contribution for ionic transport in the array with charged pores is concentration polarization.

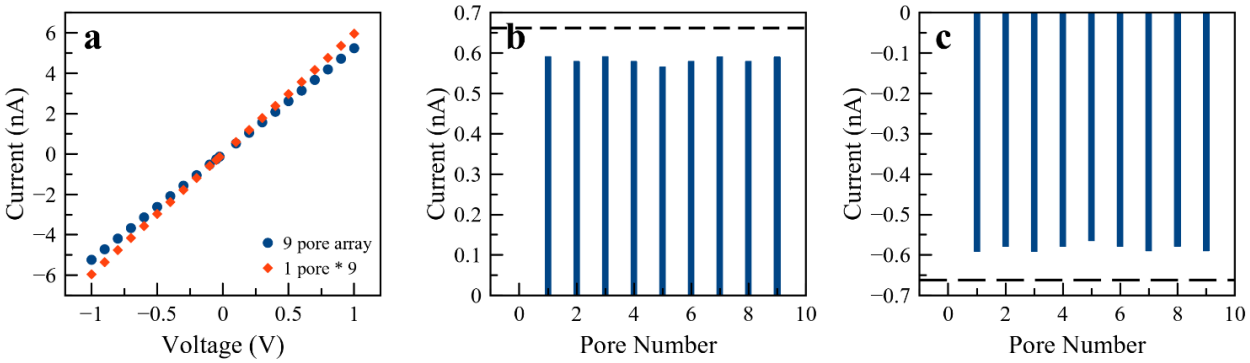

Figure 5.3: Ion current in an array composed of 9 pores with uncharged walls and separated by a distance of 6 nm. (a) Current-voltage of the whole array as well as current-voltage curve of an isolated uncharged nanopore with currents multiplied by 9. (b) Current through each pore in the 9-pore array at the transmembrane potential of V_m = 1 V. The dashed line represents the current at this voltage for a single isolated nanopore. (c) Same as (b) at V_m = -1 V [4]. Reprinted with permission from R. A. Lucas and Z. S. Siwy, "Tunable Nanopore Arrays as the Basis for Ionic Circuits," *ACS Appl. Mater. Interfaces*, vol. 12, no. 50, pp. 56622–56631, Dec. 2020, doi: 10.1021/acsami.0c18574. Copyright 2020 American Chemical Society.

To investigate further the effect of number of pores surrounding an individual nanopore on its ionic transport we analyzed arrays with 3 and 6 nanopores. The center-to-center distance between these pores was kept constant at 6 nm. Current through individual nanopores in 3, 6, and 9-pore arrays in 100 mM KCl solution is shown in Figure 5.4. The most important finding in Figure 5.4 is the dependence of ion current not only on the numbers of neighbors but also the total number of pores in the array. It should be noted that this dependence is expected to occur only up to a threshold number of nanopores. In arrays where the number of pores inside the array outnumber those on the perimeter the current through individual pores is no longer expected to be affected by further increase in number of pores [76].

In order to produce the largest effect on nanopore interactions a distance between pores of 6 nm was used for the remaining simulations shown here.

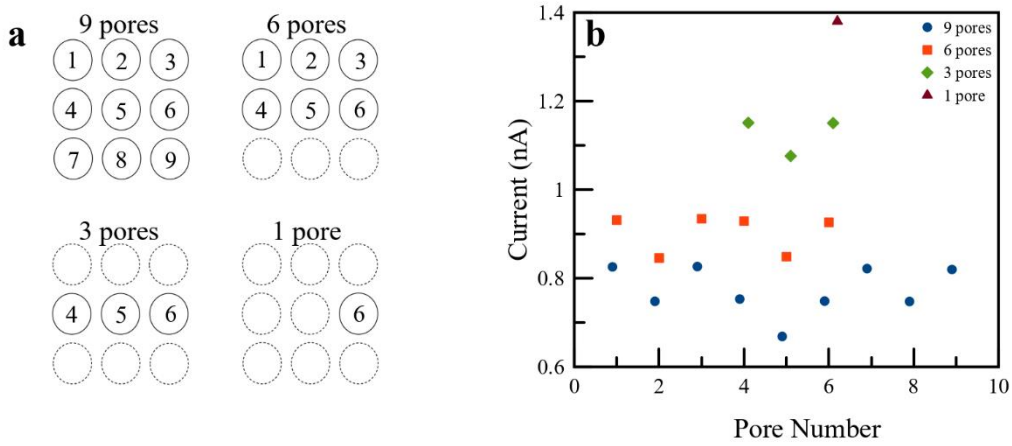

Figure 5.4: Dependence of ion current on number of pores in an array. (a) Scheme showing layout of arrays with various numbers of pores. Each pore in the arrays is numbered; the number correlates with that shown in (b) and indicates the pore location. (b) Current at V_m = 1 V in 100 mM KCl through individual pores for arrays containing 3, 6 and 9 nanopores; current through an isolated nanopore is shown as well. All nanopores were 5 nm in diameter, 40 nm in length with homogeneous surface charge density of -0.05 C/m^2. The pores were distant from each other by 6 nm [4]. Reprinted with permission from R. A. Lucas and Z. S. Siwy, "Tunable Nanopore Arrays as the Basis for Ionic Circuits," *ACS Appl. Mater. Interfaces*, vol. 12, no. 50, pp. 56622–56631, Dec. 2020, doi: 10.1021/acsami.0c18574. Copyright 2020 American Chemical Society.

5.2 Controlling Array Properties through Gate Voltage Application

The analysis shown above reveals that when nanopores are packed close to one another their transport properties are dependent on the number of neighbors and the total number of pores in an array. The total current of an array was shown lower than the magnitude predicted based on isolated nanopores due to concentration polarization. We thought therefore that if we could control the effect of concentration polarization and local ionic concentrations at the pore mouths with the depletion zone, the nanopore array could be made responsive to external signals. Applying potential difference presents one of the simplest ways to change nanopore transport properties, thus a gate electrode was placed on the membrane surface near the openings of the nanopore array (Figure 5.5a). We hypothesized that control of the gate voltage, V_g, would allow for ionic transport

manipulation through either enhancement or depletion of ionic concentrations at the pore entrances and even inside the pores. Figure 5.5 plots the total ionic concentration at each pore mouth for either V_m = -0.5 V or V_m = +0.5V as well as V_g = -0.8V or V_g = +0.8V. We plot ionic concentrations on both sides of the membrane, which allows us to follow the effect of gate voltage on concentration polarization across different pores of the array.

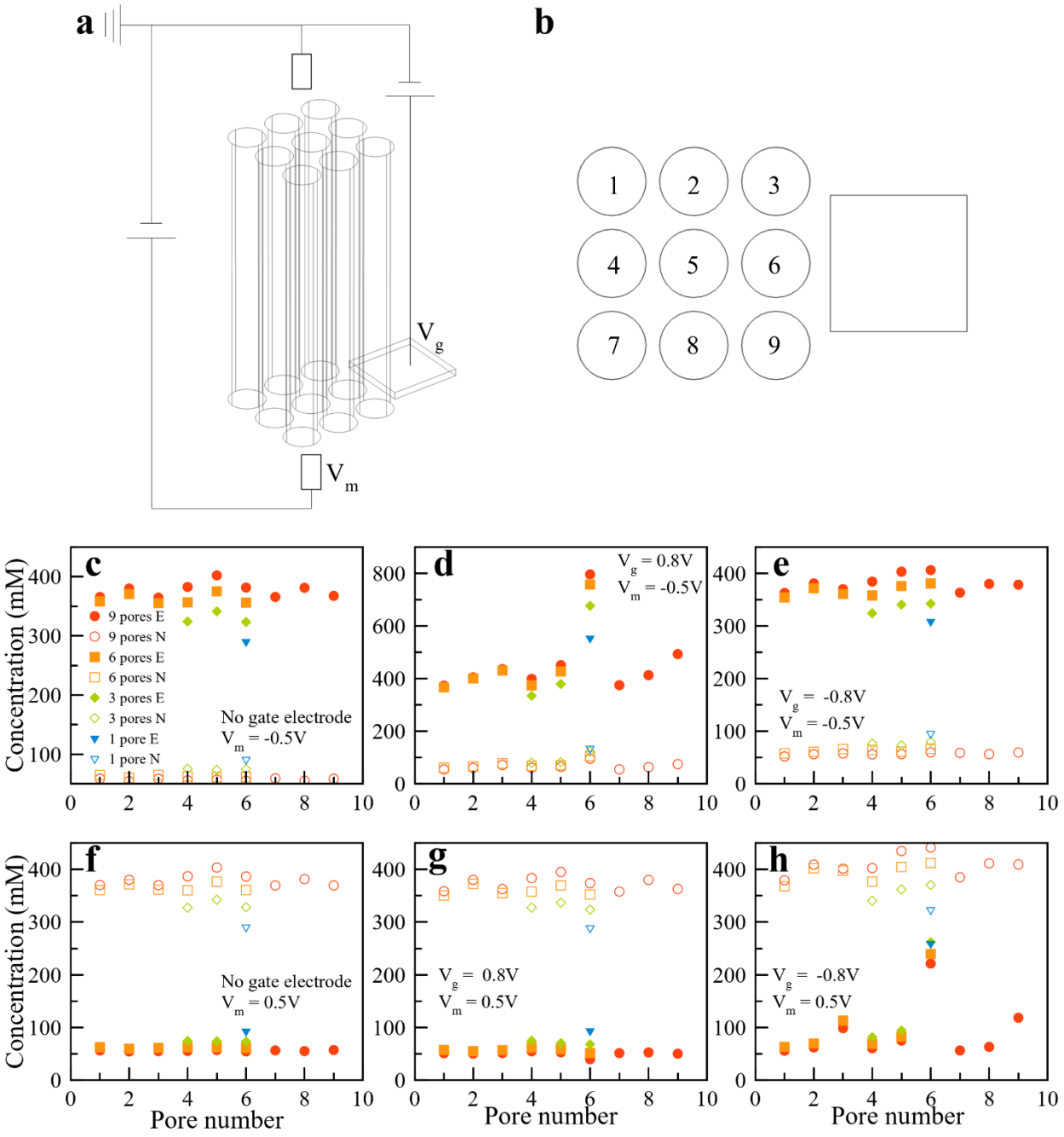

Figure 5.5: Modeling of ionic concentrations at nanopore entrances with transmembrane and gate potentials applied. (a) Scheme of the nanopore array with the electrodes that set the transmembrane potential, V_m, and the gate potential, V_g. (b) Bottom view of the array with the nanopores' numbers indicated. (c-h) Total ionic concentrations (sum of concentrations of cations and anions) at the center of each individual pore mouth in nanopore arrays with varying number of pores. Results for arrays with 3, 6 and 9 nanopores are shown; results for an individual, isolated nanopore are shown as well. The same pore numbering as in Figure 5.4 was used.

The legend indicates array size as well as whether the value was taken from the pore entrance on the side of the membrane with the electrode, E, or the side of the membrane without the electrode, N. The top row of plots was obtained at V_m = -0.5 V while the bottom row panels present results at V_m = 0.5 V. The following conditions were used in the modeling: (a) V_m = -0.5 V with no surface electrode, (b) V_m = -0.5 V, V_g = 0.8 V, (c) V_m =-0.5 V, V_g = -0.8 V, (d) V_m = 0.5 V with no surface electrode, (e) V_m = 0.5 V, V_g = 0.8 V, and (f) V_m = 0.5 V, V_g = -0.8 V. All simulations were performed in 100 mM KCl. The nanopores were 5 nm in diameter and 6 nm apart. The pore walls had charge density of -0.05 C/m^2 [4]. Reprinted with permission from R. A. Lucas and Z. S. Siwy, "Tunable Nanopore Arrays as the Basis for Ionic Circuits," *ACS Appl. Mater. Interfaces*, vol. 12, no. 50, pp. 56622–56631, Dec. 2020, doi: 10.1021/acsami.0c18574. Copyright 2020 American Chemical Society.

Figure 5.5 presents ionic concentrations at the entrances of nanopores in arrays that consist of 3, 6, or 9 nanopores. A cross-sectional view of the total concentration through the pores along the central line (pores 4, 5, and 6) is shown in Figure 5.6.

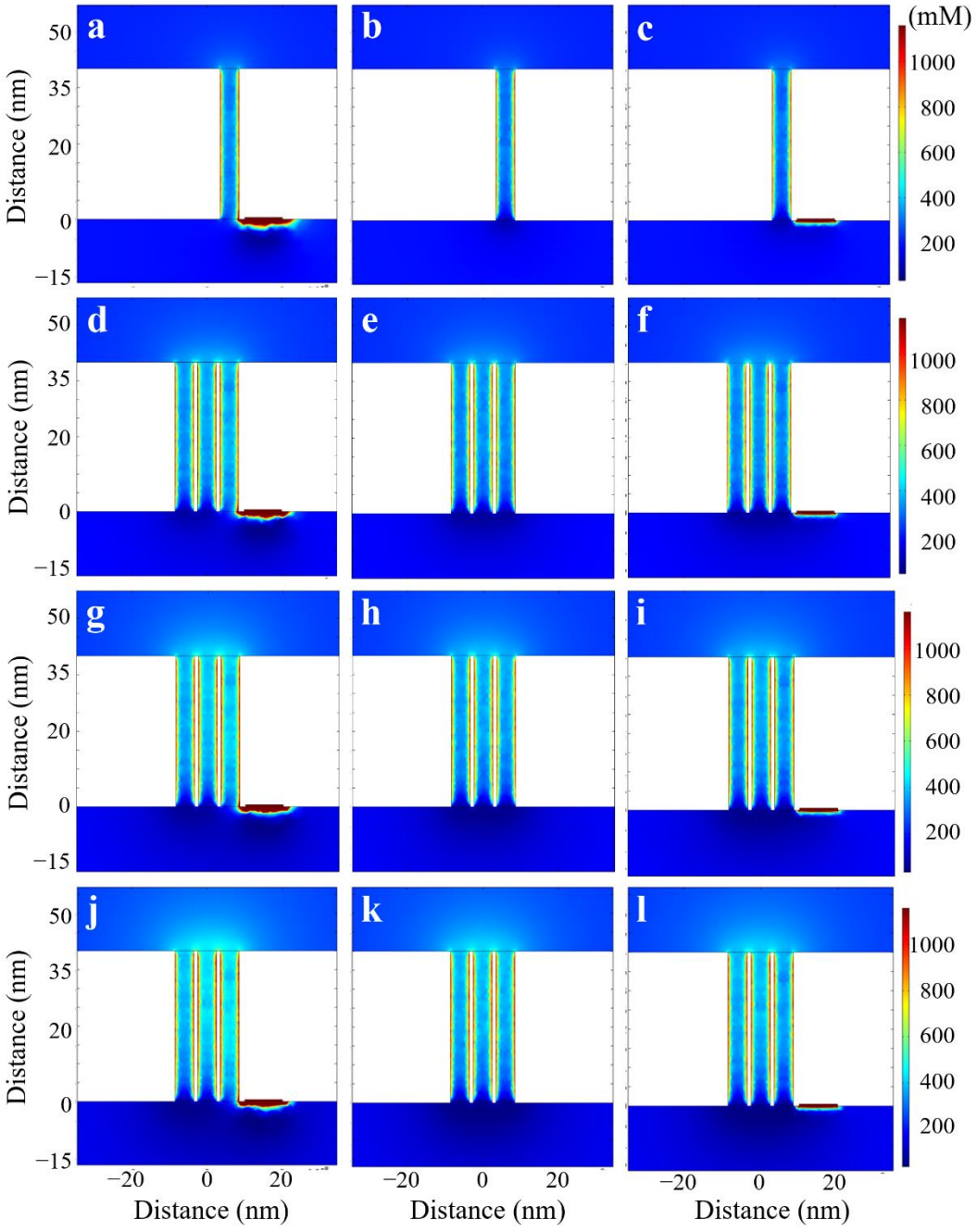

Figure 5.6: Surface representation of total ionic concentration for a single pore (a-c), and in pores 4-6 in the 3-pore array (d-f), 6-pore array (g-i), and 9-pore array (j-k) obtained at V_m = 0.5 V in 100 mM KCl solution. (a,d,g,j) V_g = -0.8 V, (b,e,h,k) no gate electrode, and (c,f,i,l) V_g = 0.8 V [4]. Reprinted with permission from R. A. Lucas and Z. S. Siwy, "Tunable Nanopore Arrays as the Basis for Ionic Circuits," *ACS Appl. Mater. Interfaces*, vol. 12, no. 50, pp. 56622–56631, Dec. 2020, doi: 10.1021/acsami.0c18574. Copyright 2020 American Chemical Society.

The ion concentration profiles shown in Figure 5.6 reveal that the gate voltage and transmembrane potential influence ionic concentrations over the entire pore entrance area. However, plotting the concentration only at the center of each pore entrance, as done in Figure 5.5, still allows us to perform accurate quantitative analysis of ionic concentrations at different pores, and with various voltage combinations applied. It is shown through these results that as the number of pores increases the changes in local ionic concentrations become greater. Similar modeling was also performed in 10 mM KCl (Figure 5.7). As the bulk concentration is lowered, the modulations of local ionic concentrations and ionic current are stronger compared to the results in 100 mM. Qualitatively, the effects of gate voltage and transmembrane potential in the two concentrations are however similar.

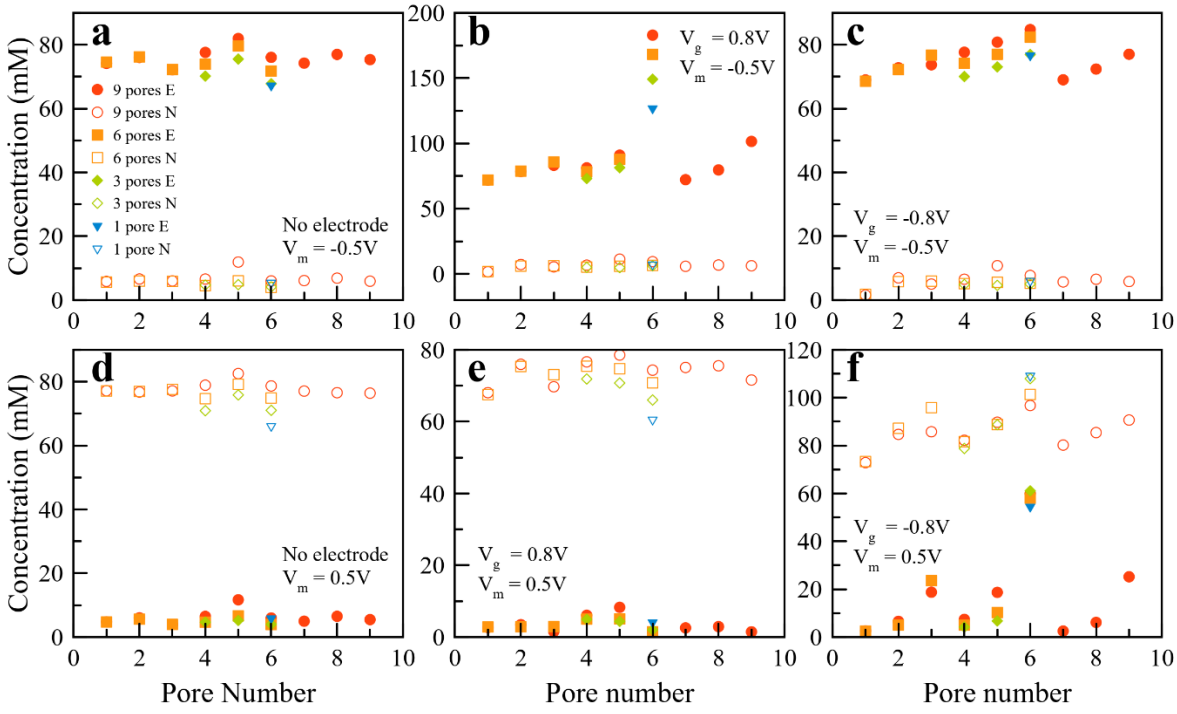

Figure 5.7: Total ionic concentrations (sum of concentrations of cations and anions) at the center of each individual pore mouth in nanopore arrays with varying number of pores. The legend indicates array size as well as whether the value was taken from the pore entrance on the side of the membrane with the electrode, E, or the side of the membrane without the electrode, N. The plots in the top row were obtained at V_m = -0.5 V while the bottom row panels present results at V_m =0.5 V. The following conditions were used in the modeling: (a) V_m = -0.5 V with no surface electrode, (b) V_m = -0.5 V, V_g = 0.8 V, (c) V_m = -0.5 V, V_g = -0.8 V, (d) V_m = 0.5 V

with no surface electrode, (e) V_m = 0.5 V, V_g = 0.8 V, and (f) V_m = 0.5 V, V_g = -0.8 V. All modeling was done in 10 mM KCl solution [4]. Reprinted with permission from R. A. Lucas and Z. S. Siwy, "Tunable Nanopore Arrays as the Basis for Ionic Circuits," *ACS Appl. Mater. Interfaces*, vol. 12, no. 50, pp. 56622–56631, Dec. 2020, doi: 10.1021/acsami.0c18574. Copyright 2020 American Chemical Society.

In the nanopore arrays considered here, the gate electrode is placed on the side of the membrane with the working electrode. It is known that, for negatively charged pores, the side of the membrane in contact with a positively biased electrode will contain a depletion zone. Therefore, if a negative voltage is applied to the gate electrode, we should observe an increase in ionic concentrations in the depletion zone. This is exactly what is seen in Figure 5.5h in comparison with a system without a gate electrode present (Figure 5.5f). It is also shown that pores closest to the gate electrode experience the largest modulations of local ionic concentrations, but some modulation is observed at nearly all pores. Thus, the gate can exert control over the entire array, while also inducing differences in individual pore behaviors. For the opposite case, when negative voltages are applied across the pore, negative gate voltage only has a small effect on the concentration at the pore mouths (Figure 5.5e).

The changes in ionic concentrations at the pore mouth induced by the gate potential, V_g, and transmembrane potential, V_m, directly influence ion current through the pores as shown in Figure 5.8. This figure shows current through individual pores in a 9-pore array for two polarities of V_m and V_g (Figure 5.5a). All results were obtained in 100 mM KCl and confirm that the ion current is mostly affected by ionic concentrations at the side of the pore where the depletion zone is formed.

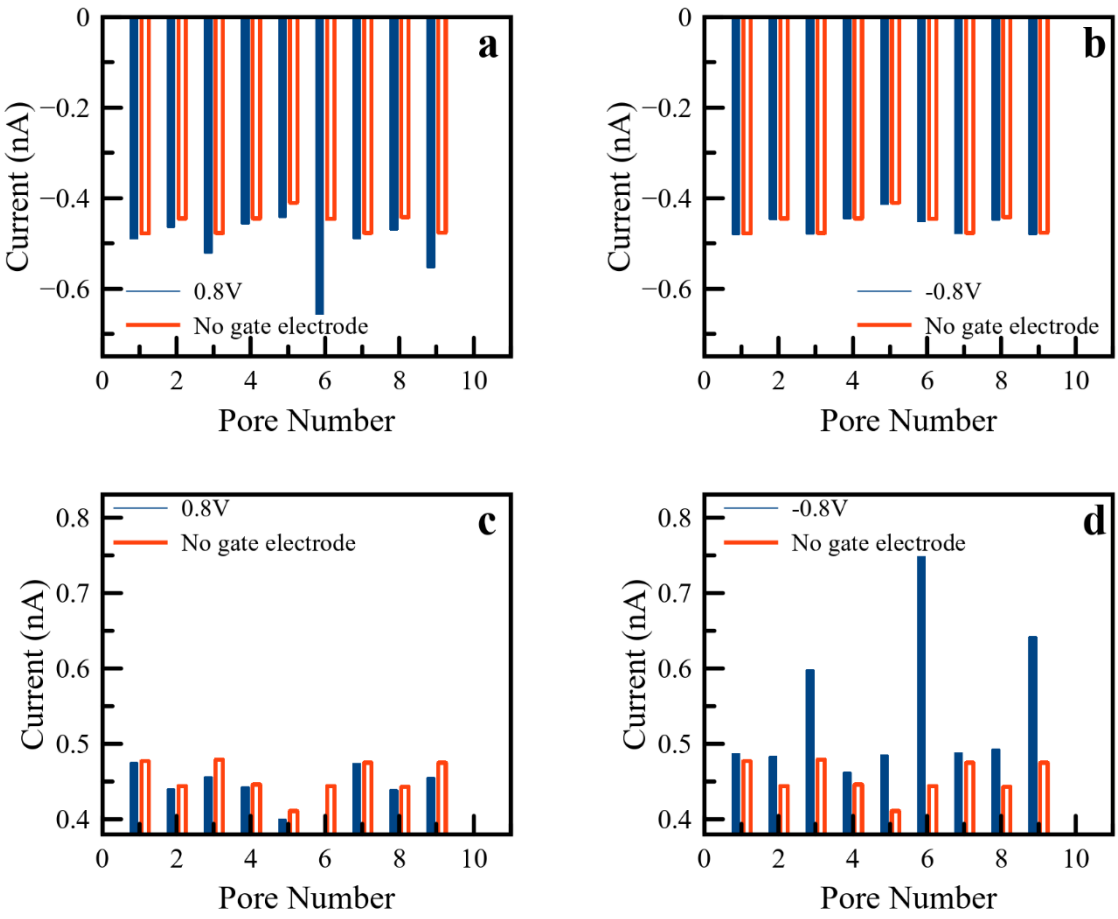

Figure 5.8: Ion current through individual nanopores of a 9-pore array with gate voltage applied. The following combinations of V_m and V_g were used in the modeling: (a) V_m = -0.5 V, V_g = 0.8 V, (b) V_m =-0.5 V, V_g =-0.8 V, (c) V_m = 0.5 V, V_g = 0.8 V, and (d) V_m = 0.5 V, V_g = -0.8 V. Currents for a 9-pore array without a gate electrode are shown in each panel in red. All simulations were performed in 100 mM KCl. The nanopores were 5 nm in diameter and 6 nm apart. The pore walls had charge density of -0.05 C/m^2 [4]. Reprinted with permission from R. A. Lucas and Z. S. Siwy, "Tunable Nanopore Arrays as the Basis for Ionic Circuits," *ACS Appl. Mater. Interfaces*, vol. 12, no. 50, pp. 56622–56631, Dec. 2020, doi: 10.1021/acsami.0c18574. Copyright 2020 American Chemical Society.

Figure 5.8 confirms the stronger effect of negative gate voltages versus positive gate voltages on local ionic concentrations and thus ion current. The results further suggest that pores with suppressed conductance may be switched to higher conductance states with the application of a gate voltage. Gate voltage has, however, a weaker effect in reducing ion current beyond the effect of concentration polarization and nanopore interdependence.

Due to the asymmetric influence of opposite gate voltage polarities on ion current, in the next step, we analyzed ion current rectification of individual pores in the array. Ion current rectification is defined as the absolute value of the ratio of current at V_m = -1V to the current at V_m = +1V. These values are plotted in Figure 5.9 for individual pores within a 9-pore array for two gate voltage values, V_g = ±0.8V, as well as for an array without the gate. Without a gate electrode present the rectification of all nanopores is ~1, as we would expect for individual cylindrically shaped nanopores. Looking first at the results shown for 100 mM KCl (Figure 5.9a), rectification ratio below 1 for negative V_g indicates that positive currents are enhanced over negative currents, as is expected due to the mitigation of concentration polarization. For positive V_g a rectification ratio above 1 is present, indicating enhanced negative currents versus positive currents. This aligns with the enhanced concentration polarization seen for these positive gate voltage values.

The most interesting results concerning rectification properties of individual pores were obtained when the bulk concentration was decreased to 10 mM (Figure 5.9b). In these conditions, applying gate voltage of the same polarity induces different rectification properties of the pores in the array, even though the pores have the same geometry and surface charge properties. More specifically, there is a subset of the pores that rectify the current such that positive currents are larger than negative currents, while another subset of nanopores rectifies in the opposite direction. Consequently, at 10 mM, when a negative gate voltage is applied, the nanopores closest to the gate have a rectification ratio less than 1 while the remaining pores exhibit opposite rectification, with values greater than 1. These results provide an evidence for the coupling of ion current modulation due to applied gate voltage and the interaction of ionic transport between individual nanopores.

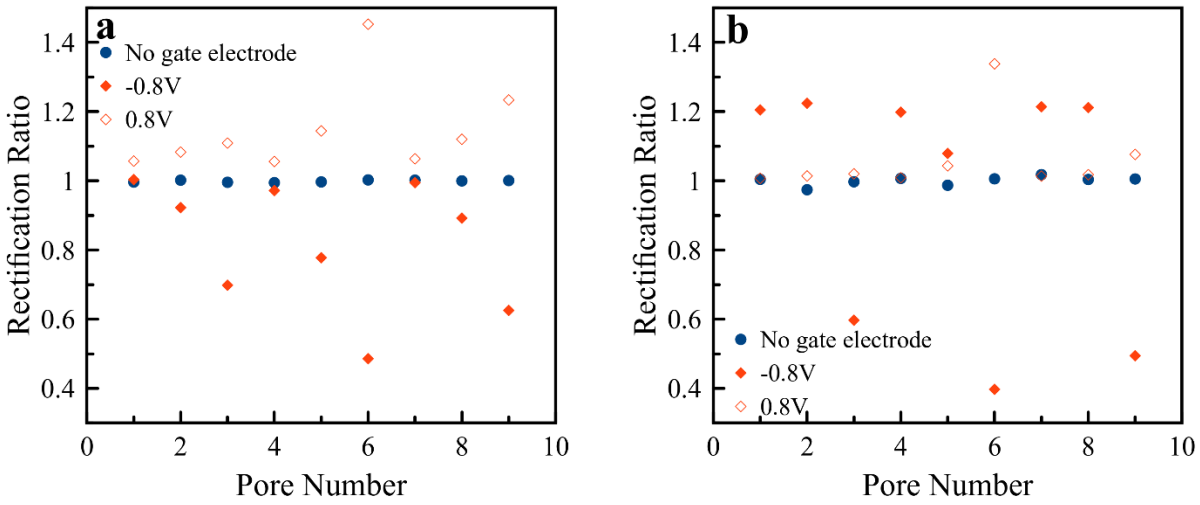

Figure 5.9: Rectification degree for nanopores in a 9-nanopore array as a function of gate potential. Rectification was calculated as the absolute value of a ratio of ion currents at V_m =-1 V and at V_m = 1 V for two values of V_g, shown in the legend, in (a) 100 mM and (b) 10 mM KCl bulk solution. All pores were 5 nm in diameter and 40 nm in length; the distance between nanopores was kept at 6 nm [4]. Reprinted with permission from R. A. Lucas and Z. S. Siwy, "Tunable Nanopore Arrays as the Basis for Ionic Circuits," *ACS Appl. Mater. Interfaces*, vol. 12, no. 50, pp. 56622–56631, Dec. 2020, doi: 10.1021/acsami.0c18574. Copyright 2020 American Chemical Society.

To provide understanding for the position dependent ion current rectification, the cross-sectional distribution of ionic concentrations was simulated and can be viewed in Figure 5.10. Shown are the cross sections of pores 1-3 for a 9-pore array in 100 mM KCl (top row) and 10 mM KCl (bottom row) for the various applied voltage combinations. In both concentrations, with a positive transmembrane potential and a negative gate voltage, the depletion zone at the entrance of pore 3, the pore closest to the electrode, contains enhanced ionic concentrations compared to that seen without an electrode present or with a positive gate voltage applied. This agrees with the expectation that negative gate voltage mitigates concentration polarization. However, in 10 mM KCl, the same negative gate potential decreases concentration at the entrances of pores 1 and 2. This suggests that pores closest to the gate electrode may act similar to a current sink and may limit the number of ions available to the pores further from the electrode. This effect is significant in 10 mM versus

100 mM solution due to the higher selectivity and strong concentration polarization in the lower concentration.

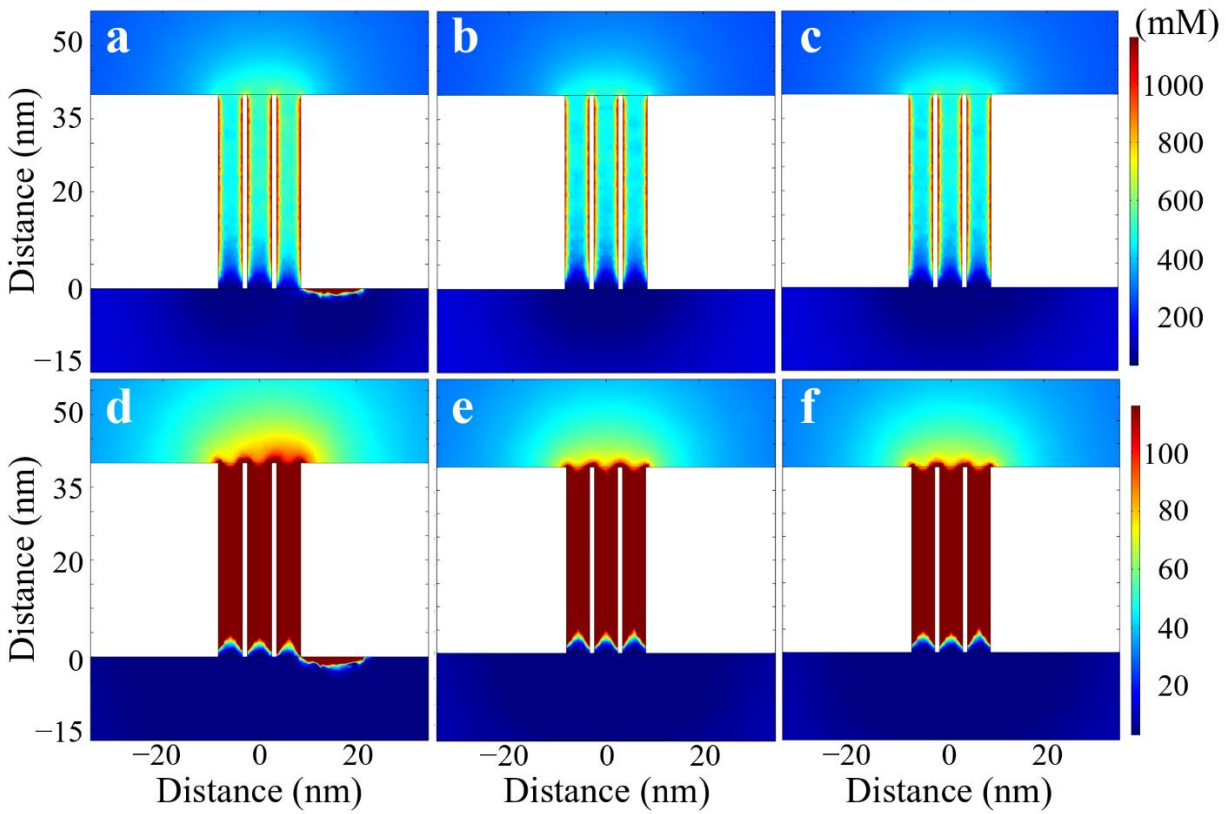

Figure 5.10: Surface representation of total ionic concentration in pores 1-3 in the 9-pore array. (a-c) Results in 100 mM, (d-f) Results in 10 mM at V_m = 1 V, and the following gate potentials: (a,d) V_g = -0.8 V, (b,e) no gate electrode, and (c,f) V_g = 0.8 V [4]. Reprinted with permission from R. A. Lucas and Z. S. Siwy, "Tunable Nanopore Arrays as the Basis for Ionic Circuits," *ACS Appl. Mater. Interfaces*, vol. 12, no. 50, pp. 56622–56631, Dec. 2020, doi: 10.1021/acsami.0c18574. Copyright 2020 American Chemical Society.

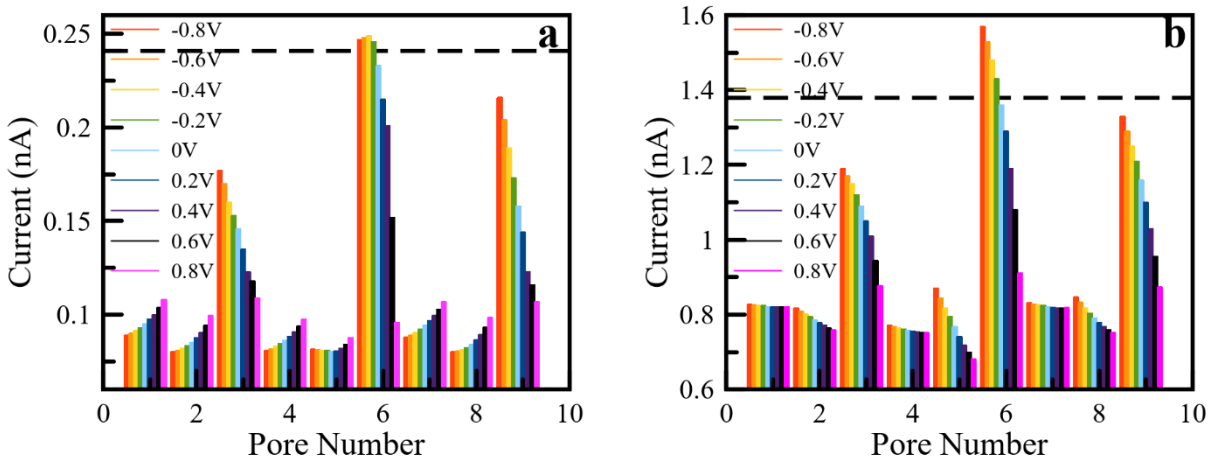

Figure 5.11: Ion current through individual nanopores of the 9-pore array as a function of gate potential, V_g. The modeling was performed at V_m = 1 V in (a) 10 mM KCl, and (b) 100 mM KCl. Voltage at the gate electrode, V_g, was varied as shown in the legend. All pores were 5 nm in diameter, and 40 nm in length; the distance between nanopores was kept at 6 nm [4]. Reprinted with permission from R. A. Lucas and Z. S. Siwy, "Tunable Nanopore Arrays as the Basis for Ionic Circuits," *ACS Appl. Mater. Interfaces*, vol. 12, no. 50, pp. 56622–56631, Dec. 2020, doi: 10.1021/acsami.0c18574. Copyright 2020 American Chemical Society.

Results shown in previous figures consider only one magnitude of gate voltage, 0.8 V. In order to understand the sensitivity of ionic transport to changes in gate voltage, ion current through individual pores in a 9-pore array was modeled, as shown in Figure 5.11. The new modeling results corroborate the conclusions which were drawn when looking at rectification ratios in 10 mM and 100 mM solution in Figure 5.9. Explicitly, Figure 5.11a shows results in 10 mM solution where only the pores closest to the gate electrode exhibit an increase in their conductance as the gate potential becomes more negative while all the pores further from the gate electrode exhibit a decrease in conductance over the same potential range. As the gate potential becomes more negative, the concentration profiles become more asymmetric and less ions become available to pores 1, 2, 4, 5, 7, and 8. Accordingly, for the same gate potential, different nanopores within the array exhibit different rectification and transport properties. It is these unique properties that could allow

for special applications like delivery of specific ions or molecules to specific locations, as may be necessary in some drug delivery devices.

5.3 Tuning Array Function through Addition of Pore with Nonlinear Current-Voltage Characteristics

So far, we have considered nanopore arrays whose transport properties can be tuned using an external voltage signal applied to a gate electrode. Another way to tune transport of nanopores in an array would be to include nanopores with nonlinear current-voltage characteristics. Considering arrays with nanopores that exhibit diode-like behavior would directly mimic a biological cell membrane that also contains nanopores and channels with diverse transport properties. To probe this concept, a 3-nanopore system was created where one of the three pores was a diode. The diode was created by imposing half positive surface charge and half negative surface charge on a cylindrical nanopore as shown in Figure 5.12a.

The system is first modeled in Figure 5.12c,d without a gate electrode to see the influence of the ionic diode on ionic transport on its own. With the diode configuration described and the transmembrane electrode placement similar to previous experiments, the diode functions in a higher conductance state for positive V_m and a lower conductance state for negative V_m. The diode position was tested in each of the three pore positions shown. The results indicate that without a gate electrode the diode enhances current through all pores at positive V_m. When placed in either of the two end positions (1 or 3) the diode causes enhanced current at positive transmembrane potential of the middle pore (2), leading to a rectification degree less than 1 (Figure 5.12d). Interestingly, the pore furthest from the diode rectifies in the opposite direction such that negative currents are higher than positive currents. If, however,

the diode is place in the middle position (2) current through both neighboring pores increases and all pores rectify in the same direction, with positive currents higher than negative currents.

The next step was to probe the system with a gate electrode present. We chose V_g = -0.8V as previous results have shown this potential to have the largest effect on ionic transport of nanopores in an array (Figure 5.12e,f). Again, three positions of the diode were tested. These results suggest that the currents through all three nanopores are affected most by the gate bias potential when the diode is placed closest to the surface electrode (at position 3). Both the presence of the diode and the application of a negative voltage increase the current through the neighboring pore. Thus, with the diode closest to the electrode, these two effects combine to give the highest overall current as shown in Figure 5.12e.

When the presence of an ionic diode is combined with the gate electrode, it is possible to control ion current through individual nanopores such that specific pores become the dominant contributors of ionic transport throughout the array. Figure 5.13a-c shows current-voltage curves through individual pores for varying V_g and V_m combinations. Here, the control of ionic transport through individual nanopores is explicitly evidenced. For example, without a gate voltage (Figure 5.13a) the ionic diode is the main current contributor only for V_m > 0.5V. With a negative gate voltage applied (Figure 5.13b) it is possible to exhibit different currents through all three nanopores at the same V_m, a property which could be useful in the formation of spatial chemical gradients.

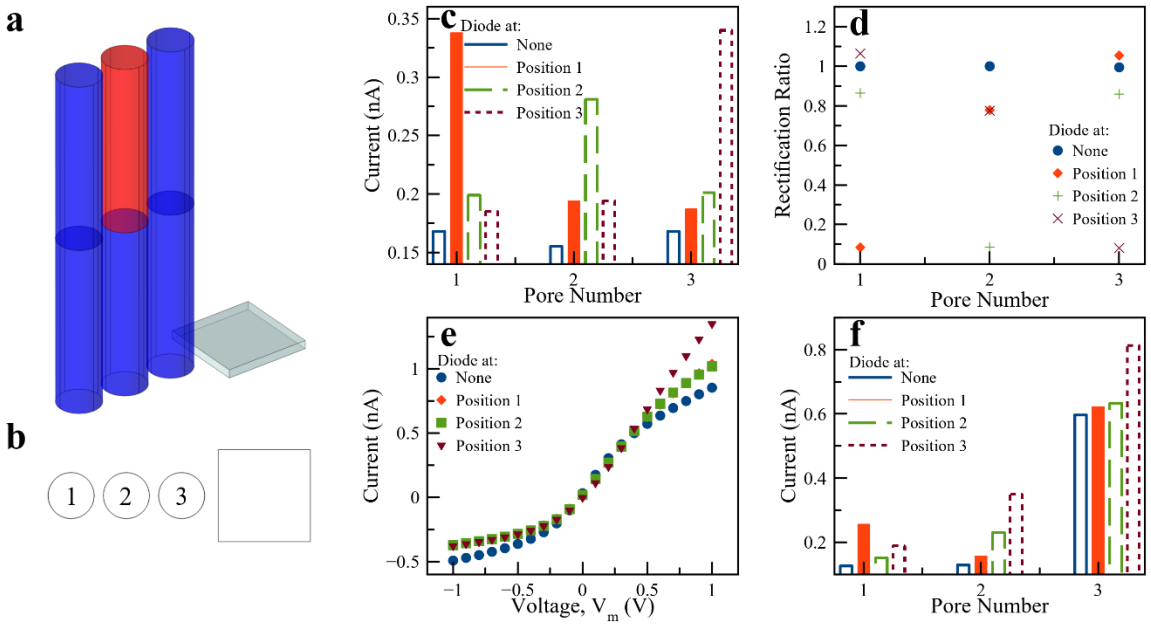

Figure 5.12: Modeling of a 3-pore array with a diode. (a) 3-dimensional representation of the COMSOL model showing a diode placed in pore position 2. Here, blue represents negative surface charge density of -0.05 C/m,[2] and red represents positive surface charge density of +0.05 C/m^2. 10 mM KCl was used in the simulations. (b) Top-down view of the setup showing assigned pore numbers. (c) Current at a transmembrane potential of V_m = 1 V through each pore of a 3-pore array containing an ionic diode placed in position 1, 2 or 3, as labeled in the legend. A gate electrode is not included in this system. (d) Rectification ratios for the system shown in (c) calculated at V_m = ±1 V. (e) Current-voltage curves for a 3-pore array with a diode placed in various positions of the array, and a gate electrode placed as shown in (b) at V_g = -0.8 V (f) Current through individual nanopores at a transmembrane potential of V_m = 1 V for the system shown in (e) [4]. Reprinted with permission from R. A. Lucas and Z. S. Siwy, "Tunable Nanopore Arrays as the Basis for Ionic Circuits," *ACS Appl. Mater. Interfaces*, vol. 12, no. 50, pp. 56622–56631, Dec. 2020, doi: 10.1021/acsami.0c18574. Copyright 2020 American Chemical Society.

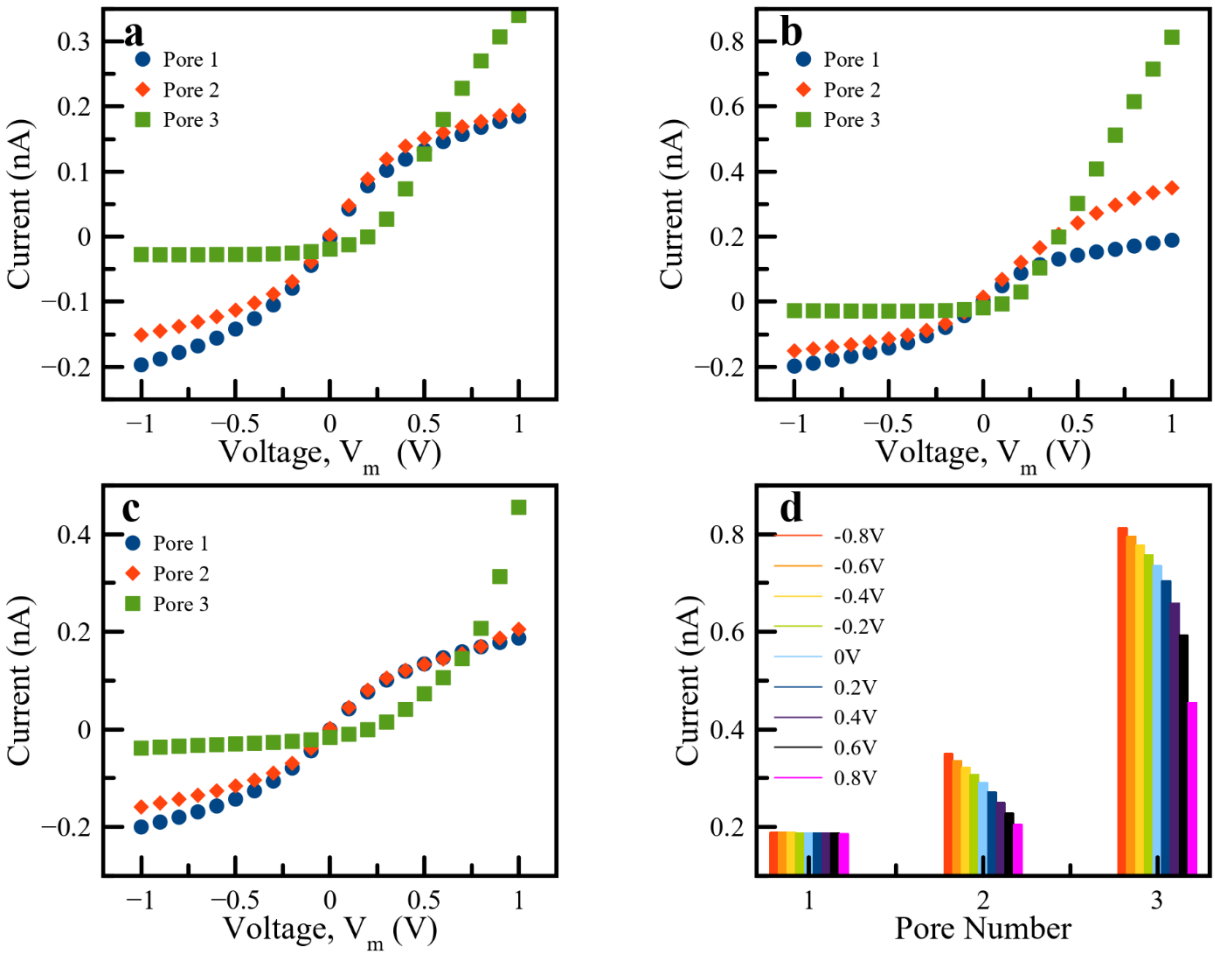

Figure 5.13: Tuning ion current through individual pores in a 3-pore array with a diode. (a) Current-voltage curves through each individual pore in the 3-pore array with the diode placed in position 3. Nanopores in positions 1 and 2 are negatively charged. The gate electrode was not included in the modeling. (b) Same system as (a) but with V_g = -0.8 V, located as shown in Figure 5.12a,b. (c) Same as (b) with V_g = 0.8 V. (d) Current through each pore at V_m = 1 V and V_g varied as shown in the legend. The modeling was done in 10 mM KCl [4]. Reprinted with permission from R. A. Lucas and Z. S. Siwy, "Tunable Nanopore Arrays as the Basis for Ionic Circuits," *ACS Appl. Mater. Interfaces*, vol. 12, no. 50, pp. 56622–56631, Dec. 2020, doi: 10.1021/acsami.0c18574. Copyright 2020 American Chemical Society.

To confirm the influence of ionic diodes on ionic transport could be implemented in larger arrays as well, the system was expanded and tested as a 9-pore array (Figure 5.14). For this system three diodes were placed in positions 3, 6, and 9 such that they would be in the positions closest to the gate electrode. Again, the system was considered both with and without a gate electrode present. Similar to the 3-pore system, the combination of the diodes and a negative gate potential led to current enhancement at positive V_m compared to the case

without diodes. It is also observed that the maximum magnitude of current is lower than that exhibited in the 3-pore array, as would be expected from initial results showing decreased current magnitude for increased number of pores within an array (Figure 5.4). Again, similar to the 3-pore array, with the presence of diodes, gate potential allows control over ionic transport through individual nanopores in a similar manner.

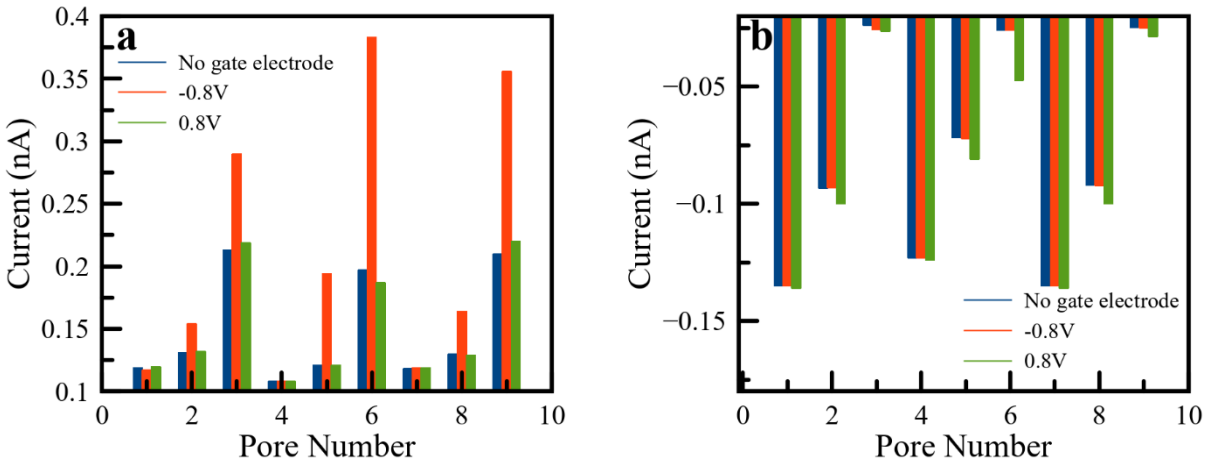

Figure 5.14: Ion current through individual nanopores of a 9-pore array with three diodes positioned at locations 3, 6 and 9. Three cases were considered: no gate voltage, V_g= -0.8 V and V_g = 0.8 V. The modeling was performed in 10 mM KCl at (a) V_m = 1 V and (b) V_m = -1 V. All nanopores were 5 nm in diameter and 6 nm apart [4]. Reprinted with permission from R. A. Lucas and Z. S. Siwy, "Tunable Nanopore Arrays as the Basis for Ionic Circuits," *ACS Appl. Mater. Interfaces*, vol. 12, no. 50, pp. 56622–56631, Dec. 2020, doi: 10.1021/acsami.0c18574. Copyright 2020 American Chemical Society.

Nanopore arrays presented in this chapter demonstrate manipulation of ionic current through voltage application at a gate which affects even pores further from direct contact with the gate. Modulation of current is also shown to be affected by placement of pores with nonlinear current-voltage characteristics. With a small enough array system ionic currents cease being independent of one another. Thus, new phenomena are exhibited based on this principle leading to new potential applications such as mimicking of transient ionic signals like those in axons or development of complex spatial chemical gradients which may be useful in drug delivery devices.

CONCLUSIONS

Throughout this document a variety of ion current control methods are investigated. The nanopore systems that we examined were used to understand electrochemical properties of a solid/liquid interface as well as to understand and tune transport properties at the nanoscale. The nanopores were also a template for several devices including ionic transistors and nanopore arrays as a basis for ionic circuits.

Polyethylene terephthalate (PET) nanopores are used in a wide range of ion current studies. In this work cylindrical pores were utilized to investigate the effect of solvent type, voltage, and ionic concentration on ionic current and thus surface charge in the system. Through measurements utilizing electroosmotic flow it was revealed that the carboxlyated surface of PET can flip charge polarity dependent on solvent type and concentration of $LiClO_4$. This work helped overall understanding of the effective surface charge in organic solvents and its impact on ionic transport. Our measurements revealed that adsorption of lithium ions to the pore surface plays an important role in the formation of the effective positive surface potential. Numerical modeling developed here can be used for systems with varying charge density along a surface due to experimental conditions.

Variations of surface charge along with application of potential at a gate electrode provide manipulation of ion current in a way that allowed for emulation of a npn bipolar junction transistor. This system was based off pores in silicon nitride membranes with a layer of Nafion sandwiched between them. It was successfully demonstrated through this system that an ionic transistor with fully ionic inputs and outputs can easily be rearranged into amplifying units providing amplifications up to 300 times. This type of ionic

amplification could be utilized in preparation of artificial biocircuits such as those present in the synaptic cleft.

Finally, we modeled a system of a nanopore array to investigate pore interactions and effects on ionic transport. Response to gate voltage, interpore distance, number of pores, and placement of pores with nonlinear current-voltage characteristics were demonstrated as parameters capable of tuning ionic transport through the nanopore array. New phenomena were observed due to interpore interactions leading to potential new applications such as mimicking of transient ionic signals like those in axons or development of complex spatial chemical gradients which may be useful in drug delivery devices.

Much work was done throughout this thesis but there is always more to explore. This document is hoped to provide a basis for future development and exploration along these project paths.

REFERENCES

[1] Y. Jiang, A. Lee, J. Chen, M. Cadene, B. T. Chait, and R. MacKinnon, "The open pore conformation of potassium channels," *Nature*, vol. 417, no. 6888, Art. no. 6888, May 2002, doi: 10.1038/417523a.

[2] S. Majd, E. C. Yusko, Y. N. Billeh, M. X. Macrae, J. Yang, and M. Mayer, "Applications of biological pores in nanomedicine, sensing, and nanoelectronics," *Current Opinion in Biotechnology*, vol. 21, no. 4, pp. 439–476, Aug. 2010, doi: 10.1016/j.copbio.2010.05.002.

[3] Y. Zhang and G. C. Schatz, "Conical Nanopores for Efficient Ion Pumping and Desalination," *J. Phys. Chem. Lett.*, vol. 8, no. 13, pp. 2842–2848, Jul. 2017, doi: 10.1021/acs.jpclett.7b01137.

[4] R. A. Lucas and Z. S. Siwy, "Tunable Nanopore Arrays as the Basis for Ionic Circuits," *ACS Appl. Mater. Interfaces*, vol. 12, no. 50, pp. 56622–56631, Dec. 2020, doi: 10.1021/acsami.0c18574.

[5] D. Losic and S. Simovic, "Self-ordered nanopore and nanotube platforms for drug delivery applications," *Expert Opinion on Drug Delivery*, vol. 6, no. 12, pp. 1363–1381, Dec. 2009, doi: 10.1517/17425240903300857.

[6] R. Duan, F. Xia, and L. Jiang, "Constructing Tunable Nanopores and Their Application in Drug Delivery," *ACS Nano*, vol. 7, no. 10, pp. 8344–8349, Oct. 2013, doi: 10.1021/nn405092w.

[7] F. Haque, J. Li, H.-C. Wu, X.-J. Liang, and P. Guo, "Solid-state and biological nanopore for real-time sensing of single chemical and sequencing of DNA," *Nano Today*, vol. 8, no. 1, pp. 56–74, Feb. 2013, doi: 10.1016/j.nantod.2012.12.008.

[8] S. W. Kowalczyk, T. R. Blosser, and C. Dekker, "Biomimetic nanopores: learning from and about nature," *Trends in Biotechnology*, vol. 29, no. 12, pp. 607–614, Dec. 2011, doi: 10.1016/j.tibtech.2011.07.006.

[9] J. J. Kasianowicz, E. Brandin, D. Branton, and D. W. Deamer, "Characterization of individual polynucleotide molecules using a membrane channel," *PNAS*, vol. 93, no. 24, pp. 13770–13773, Nov. 1996, doi: 10.1073/pnas.93.24.13770.

[10] I. Vlassiouk and Z. S. Siwy, "Nanofluidic Diode," *Nano Lett.*, vol. 7, no. 3, pp. 552–556, Mar. 2007, doi: 10.1021/nl062924b.

[11] S.-W. Nam, M. J. Rooks, K.-B. Kim, and S. M. Rossnagel, "Ionic Field Effect Transistors with Sub-10 nm Multiple Nanopores," *Nano Lett.*, vol. 9, no. 5, pp. 2044–2048, May 2009, doi: 10.1021/nl900309s.

[12] R. A. Lucas, C.-Y. Lin, L. A. Baker, and Z. S. Siwy, "Ionic amplifying circuits inspired by electronics and biology," *Nature Communications*, vol. 11, no. 1, Art. no. 1, Mar. 2020, doi: 10.1038/s41467-020-15398-3.

[13] E. B. Kalman, I. Vlassiouk, and Z. S. Siwy, "Nanofluidic Bipolar Transistors," *Advanced Materials*, vol. 20, no. 2, pp. 293–297, 2008, doi: https://doi.org/10.1002/adma.200701867.

[14] S. Smirnov, I. Vlassiouk, P. Takmakov, and F. Rios, "Water Confinement in Hydrophobic Nanopores. Pressure-Induced Wetting and Drying," *ACS Nano*, vol. 4, no. 9, pp. 5069–5075, Sep. 2010, doi: 10.1021/nn101080k.

[15] Z. S. Siwy and S. Howorka, "Engineered voltage-responsive nanopores," *Chemical Society Reviews*, vol. 39, no. 3, pp. 1115–1132, 2010, doi: 10.1039/B909105J.

[16] P. Y. Apel, I. V. Blonskaya, O. L. Orelovitch, P. Ramirez, and B. A. Sartowska, "Effect of nanopore geometry on ion current rectification," *Nanotechnology*, vol. 22, no. 17, p. 175302, Mar. 2011, doi: 10.1088/0957-4484/22/17/175302.

[17] Z. Zeng, Y. Ai, and S. Qian, "pH-regulated ionic current rectification in conical nanopores functionalized with polyelectrolyte brushes," *Physical Chemistry Chemical Physics*, vol. 16, no. 6, pp. 2465–2474, 2014, doi: 10.1039/C3CP54097A.

[18] Y. Qiu, R. A. Lucas, and Z. S. Siwy, “Viscosity and Conductivity Tunable Diode-like Behavior for Meso- and Micropores,” *J. Phys. Chem. Lett.*, vol. 8, no. 16, pp. 3846–3852, Aug. 2017, doi: 10.1021/acs.jpclett.7b01804.
[19] R. Spohr, *Methods and Device to Generate a Predetermined Number of Ion Tracks*, vol. German Patent DE 2951376 C2. 1983.
[20] W. DeSorbo, “Ultraviolet effects and aging effects on etching characteristics of fission tracks in polycarbonate film,” *Nuclear Tracks*, vol. 3, no. 1, pp. 13–32, Mar. 1979, doi: 10.1016/0191-278X(79)90026-X.
[21] Z. Zhu, Y. Maekawa, Q. Liu, and M. Yoshida, “Influence of UV light illumination on latent track structure in PET,” *Nuclear Instruments and Methods in Physics Research Section B: Beam Interactions with Materials and Atoms*, vol. 236, no. 1, pp. 61–67, Jul. 2005, doi: 10.1016/j.nimb.2005.03.251.
[22] J. Li, “Ion-beam sculpting at nanometre length scales | Nature,” 2001. https://www.nature.com/articles/35084037 (accessed Mar. 09, 2021).
[23] A. A. Lev, Y. E. Korchev, T. K. Rostovtseva, C. L. Bashford, D. T. Edmonds, and C. A. Pasternak, “Rapid switching of ion current in narrow pores: implications for biological ion channels,” *Proc Biol Sci*, vol. 252, no. 1335, pp. 187–192, Jun. 1993, doi: 10.1098/rspb.1993.0064.
[24] A. Rigort and J. M. Plitzko, “Cryo-focused-ion-beam applications in structural biology,” *Archives of Biochemistry and Biophysics*, vol. 581, pp. 122–130, Sep. 2015, doi: 10.1016/j.abb.2015.02.009.
[25] A. J. Storm, J. H. Chen, X. S. Ling, H. W. Zandbergen, and C. Dekker, “Fabrication of solid-state nanopores with single-nanometre precision,” *Nature Materials*, vol. 2, no. 8, Art. no. 8, Aug. 2003, doi: 10.1038/nmat941.
[26] “Transmission electron microscopy,” *Wikipedia*. Mar. 03, 2021, Accessed: Mar. 08, 2021. [Online]. Available: https://en.wikipedia.org/w/index.php?title=Transmission_electron_microscopy&oldid=1010114132.
[27] “How do electron microscopes work?,” *Explain that Stuff*, Jun. 24, 2007. http://www.explainthatstuff.com/electronmicroscopes.html (accessed Mar. 08, 2021).
[28] J. N. Israelachvili, “Intermolecular and Surface Forces,” p. 706.
[29] P. Y. Apel, Yu. E. Korchev, Z. Siwy, R. Spohr, and M. Yoshida, “Diode-like single-ion track membrane prepared by electro-stopping,” *Nuclear Instruments and Methods in Physics Research Section B: Beam Interactions with Materials and Atoms*, vol. 184, no. 3, pp. 337–346, Nov. 2001, doi: 10.1016/S0168-583X(01)00722-4.
[30] W. Choi *et al.*, “A low-noise silicon nitride nanopore device on a polymer substrate,” *PLOS ONE*, vol. 13, no. 7, p. e0200831, Jul. 2018, doi: 10.1371/journal.pone.0200831.
[31] P. Nelson, *Biological Physics: Energy, Informatin, Life*. New York, NY: W.H. Freeman and Company, 2004.
[32] “Nanofluidic Ionic Diodes. Comparison of Analytical and Numerical Solutions | ACS Nano.” https://pubs.acs.org/doi/10.1021/nn800306u (accessed Mar. 09, 2021).
[33] Z. Siwy, L. Trofin, P. Kohli, L. A. Baker, C. Trautmann, and C. R. Martin, “Protein biosensors based on biofunctionalized conical gold nanotubes,” *J Am Chem Soc*, vol. 127, no. 14, pp. 5000–5001, Apr. 2005, doi: 10.1021/ja043910f.
[34] I. Vlassiouk, T. R. Kozel, and Z. S. Siwy, “Biosensing with Nanofluidic Diodes,” *J Am Chem Soc*, vol. 131, no. 23, pp. 8211–8220, Jun. 2009, doi: 10.1021/ja901120f.
[35] Y. Tian, L. Wen, X. Hou, G. Hou, and L. Jiang, “Bioinspired Ion-Transport Properties of Solid-State Single Nanochannels and Their Applications in Sensing,” *ChemPhysChem*, vol. 13, no. 10, pp. 2455–2470, 2012, doi: https://doi.org/10.1002/cphc.201200057.

[36] M. Ali, S. Nasir, and W. Ensinger, “Bioconjugation-induced ionic current rectification in aptamer-modified single cylindrical nanopores,” *Chem. Commun.*, vol. 51, no. 16, pp. 3454–3457, Feb. 2015, doi: 10.1039/C5CC00257E.
[37] G. Xie, L. Wen, and L. Jiang, “Biomimetic smart nanochannels for power harvesting,” *Nano Res.*, vol. 9, no. 1, pp. 59–71, Jan. 2016, doi: 10.1007/s12274-016-0993-1.
[38] K. Xu, “Nonaqueous Liquid Electrolytes for Lithium-Based Rechargeable Batteries,” *Chem. Rev.*, vol. 104, no. 10, pp. 4303–4418, Oct. 2004, doi: 10.1021/cr030203g.
[39] P. Simon and Y. Gogotsi, “Materials for electrochemical capacitors,” in *Nanoscience and Technology*, 0 vols., Co-Published with Macmillan Publishers Ltd, UK, 2009, pp. 320–329.
[40] Q. Li, J. Chen, L. Fan, X. Kong, and Y. Lu, “Progress in electrolytes for rechargeable Li-based batteries and beyond,” *Green Energy & Environment*, vol. 1, no. 1, pp. 18–42, Apr. 2016, doi: 10.1016/j.gee.2016.04.006.
[41] M. P. S. Mousavi *et al.*, “Ionic Liquids as Electrolytes for Electrochemical Double-Layer Capacitors: Structures that Optimize Specific Energy,” *ACS Appl. Mater. Interfaces*, vol. 8, no. 5, pp. 3396–3406, Feb. 2016, doi: 10.1021/acsami.5b11353.
[42] A. Manthiram, X. Yu, and S. Wang, “Lithium battery chemistries enabled by solid-state electrolytes,” *Nature Reviews Materials*, vol. 2, no. 4, Art. no. 4, Feb. 2017, doi: 10.1038/natrevmats.2016.103.
[43] J. Vatamanu, Z. Hu, D. Bedrov, and C. Perez, “Increasing Energy Storage in Electrochemical Capacitors with Ionic Liquid Electrolytes and Nanostructured Carbon Electrodes | The Journal of Physical Chemistry Letters,” 2013. https://pubs.acs.org/doi/abs/10.1021/jz401472c?casa_token=OlqvDyaNvhUAAAAA:mnEPMNRwLw2BrN93mt0SvBut7g8K5hde-9g7u6DrrKnpAVki4CI9Um_u_yaebsUdHef3jYKHpz1d8iNV (accessed Mar. 10, 2021).
[44] R. A. Lucas, C.-Y. Lin, and Z. S. Siwy, “Electrokinetic Phenomena in Organic Solvents,” *J. Phys. Chem. B*, vol. 123, no. 28, pp. 6123–6131, Jul. 2019, doi: 10.1021/acs.jpcb.9b04969.
[45] G. B. Westermann-Clark and C. C. Christoforou, “Note on nonaqueous electrokinetic transport in charged porous media,” *Journal of Membrane Science*, vol. 20, no. 3, pp. 325–338, Sep. 1984, doi: 10.1016/S0376-7388(00)82009-8.
[46] T. Plett *et al.*, “Rectification of nanopores in aprotic solvents – transport properties of nanopores with surface dipoles,” *Nanoscale*, vol. 7, no. 45, pp. 19080–19091, 2015, doi: 10.1039/C5NR06340J.
[47] M. L. Belaya, M. V. Feigel’man, and V. G. Levadnyii, “Structural forces as a result of nonlocal water polarizability,” *Langmuir*, vol. 3, no. 5, pp. 648–654, Sep. 1987, doi: 10.1021/la00077a011.
[48] M. Belaya, V. Levadny, and D. A. Pink, “Electric Double Layer near Soft Permeable Interfaces. 1. Local Electrostatic,” *Langmuir*, vol. 10, no. 6, pp. 2010–2014, Jun. 1994, doi: 10.1021/la00018a061.
[49] C. A. Rivera, J. S. Bender, K. Manfred, and J. T. Fourkas, “Persistence of Acetonitrile Bilayers at the Interface of Acetonitrile/Water Mixtures with Silica,” *J. Phys. Chem. A*, vol. 117, no. 46, pp. 12060–12066, Nov. 2013, doi: 10.1021/jp4045572.
[50] T. Gamble *et al.*, “Rectification of Ion Current in Nanopores Depends on the Type of Monovalent Cations: Experiments and Modeling,” *J. Phys. Chem. C*, vol. 118, no. 18, pp. 9809–9819, May 2014, doi: 10.1021/jp501492g.
[51] B. Berne, J. Fourkas, R. Walker, and J. Weeks, “Nitriles at Silica Interfaces Resemble Supported Lipid Bilayers | Accounts of Chemical Research,” 2016. https://pubs.acs.org/doi/abs/10.1021/acs.accounts.6b00169 (accessed Mar. 10, 2021).
[52] M. Ali, S. Mafe, P. Ramirez, R. Neumann, and W. Ensinger, “Logic Gates Using Nanofluidic Diodes Based on Conical Nanopores Functionalized with Polyprotic Acid Chains,” *Langmuir*, vol. 25, no. 20, pp. 11993–11997, Oct. 2009, doi: 10.1021/la902792f.

[53] J.-H. Han, K. B. Kim, H. C. Kim, and T. D. Chung, “Ionic Circuits Based on Polyelectrolyte Diodes on a Microchip,” *Angewandte Chemie*, vol. 121, no. 21, pp. 3888–3891, 2009, doi: https://doi.org/10.1002/ange.200900045.
[54] S. H. Han, S.-R. Kwon, S. Baek, and T.-D. Chung, “Ionic Circuits Powered by Reverse Electrodialysis for an Ultimate Iontronic System,” *Scientific Reports*, vol. 7, no. 1, Art. no. 1, Oct. 2017, doi: 10.1038/s41598-017-14390-0.
[55] G. Maglia *et al.*, “Droplet networks with incorporated protein diodes show collective properties,” *Nature Nanotechnology*, vol. 4, no. 7, Art. no. 7, Jul. 2009, doi: 10.1038/nnano.2009.121.
[56] K. Tybrandt, R. Forchheimer, and M. Berggren, “Logic gates based on ion transistors,” *Nature Communications*, vol. 3, no. 1, Art. no. 1, May 2012, doi: 10.1038/ncomms1869.
[57] J. Rivnay, S. Inal, A. Salleo, R. M. Owens, M. Berggren, and G. G. Malliaras, “Organic electrochemical transistors,” *Nature Reviews Materials*, vol. 3, no. 2, Art. no. 2, Jan. 2018, doi: 10.1038/natrevmats.2017.86.
[58] G. D. Spyropoulos, J. N. Gelinas, and D. Khodagholy, “Internal ion-gated organic electrochemical transistor: A building block for integrated bioelectronics,” *Science Advances*, vol. 5, no. 2, p. eaau7378, Feb. 2019, doi: 10.1126/sciadv.aau7378.
[59] D. Purves, Ed., *Neuroscience*, 3rd ed. Sunderland, Mass: Sinauer Associates, Publishers, 2004.
[60] C. Grewer, A. Gameiro, T. Mager, and K. Frendler, “Electrophysiological Characterization of Membrane Transport Proteins,” *Annual Review of Biophysics*, vol. 42, pp. 95–120, Feb. 2013, doi: https://doi.org/10.1146/annurev-biophys-083012-130312.
[61] G. A. Sauer, G. Nagel, H. Koepsell, E. Bamberg, and K. Hartung, “Voltage and substrate dependence of the inverse transport mode of the rabbit Na+/glucose cotransporter (SGLT1),” *FEBS Letters*, vol. 469, no. 1, pp. 98–100, 2000, doi: https://doi.org/10.1016/S0014-5793(00)01255-2.
[62] B. Van Zeghbroeck, *Principles of Electronic Devices*. 2011.
[63] A. C. Barbati and B. J. Kirby, “Electrokinetic Measurements of Thin Nafion Films,” *Langmuir*, vol. 30, no. 8, pp. 1985–1993, Mar. 2014, doi: 10.1021/la403735g.
[64] C.-Y. Lin, C. Combs, Y.-S. Su, L.-H. Yeh, and Z. S. Siwy, “Rectification of Concentration Polarization in Mesopores Leads To High Conductance Ionic Diodes and High Performance Osmotic Power,” *J. Am. Chem. Soc.*, vol. 141, no. 8, pp. 3691–3698, Feb. 2019, doi: 10.1021/jacs.8b13497.
[65] D. Stein, M. Kruithof, and C. Dekker, “Surface-Charge-Governed Ion Transport in Nanofluidic Channels,” *Phys. Rev. Lett.*, vol. 93, no. 3, p. 035901, Jul. 2004, doi: 10.1103/PhysRevLett.93.035901.
[66] I. Vlassiouk, S. Smirnov, and Z. Siwy, “Nanofluidic Ionic Diodes. Comparison of Analytical and Numerical Solutions,” *ACS Nano*, vol. 2, no. 8, pp. 1589–1602, Aug. 2008, doi: 10.1021/nn800306u.
[67] G. Sun, Z. Pan, S. Senapati, and H.-C. Chang, “Concentration-Gradient Stabilization with Segregated Counter- and Co-Ion Paths: A Quasistationary Depletion Front for Robust Molecular Isolation or Concentration,” *Phys. Rev. Applied*, vol. 7, no. 6, p. 064024, Jun. 2017, doi: 10.1103/PhysRevApplied.7.064024.
[68] I. Rubinstein, *Electro-Diffusion of Ions*. Society for Industrial and Applied Mathematics, 1990.
[69] Z. Sun, M. Barboiu, Y.-M. Legrand, E. Petit, and A. Rotaru, “Highly Selective Artificial Cholesteryl Crown Ether K+-Channels,” *Angewandte Chemie*, vol. 127, no. 48, pp. 14681–14685, 2015, doi: https://doi.org/10.1002/ange.201506430.
[70] M. Ali, P. Ramirez, S. Nasir, J. Cervera, S. Mafe, and W. Ensinger, “Ionic circuitry with nanofluidic diodes,” *Soft Matter*, vol. 15, no. 47, pp. 9682–9689, Dec. 2019, doi: 10.1039/C9SM01654F.
[71] P. Ramirez *et al.*, “Designing voltage multipliers with nanofluidic diodes immersed in aqueous salt solutions,” *Phys. Chem. Chem. Phys.*, vol. 18, no. 5, pp. 3995–3999, 2016, doi: 10.1039/C5CP07203D.

[72] P. Ramirez *et al.*, “Modulation of current-time traces by two-pore arrangements of polyimide nanofluidic diodes,” *Applied Physics Letters*, vol. 115, no. 18, p. 183701, Oct. 2019, doi: 10.1063/1.5125042.
[73] P. Nelson, *Biological Physics (Updated Edition)*. Macmillan, 2003.
[74] J. W. Long, B. Dunn, D. R. Rolison, and H. S. White, “Three-Dimensional Battery Architectures,” *Chem. Rev.*, vol. 104, no. 10, pp. 4463–4492, Oct. 2004, doi: 10.1021/cr020740l.
[75] D. W. M. Arrigan, “Nanoelectrodes, nanoelectrode arrays and their applications,” *Analyst*, vol. 129, no. 12, pp. 1157–1165, 2004, doi: 10.1039/B415395M.
[76] N. Godino, X. Borrisé, F. X. Muñoz, F. J. del Campo, and R. G. Compton, “Mass Transport to Nanoelectrode Arrays and Limitations of the Diffusion Domain Approach: Theory and Experiment,” *J. Phys. Chem. C*, vol. 113, no. 25, pp. 11119–11125, Jun. 2009, doi: 10.1021/jp9031354.
[77] Y. Liu, M. Sairi, G. Neusser, C. Kranz, and D. W. M. Arrigan, “Achievement of Diffusional Independence at Nanoscale Liquid–Liquid Interfaces within Arrays,” *Anal. Chem.*, vol. 87, no. 11, pp. 5486–5490, Jun. 2015, doi: 10.1021/acs.analchem.5b01162.
[78] W. Han and X. Chen, “A review: applications of ion transport in micro-nanofluidic systems based on ion concentration polarization,” *Journal of Chemical Technology & Biotechnology*, vol. 95, no. 6, pp. 1622–1631, 2020, doi: https://doi.org/10.1002/jctb.6288.